

APPLIED COMPUTATIONAL ELECTROMAGNETICS SOCIETY JOURNAL

December 2023
Vol. 38 No. 12
ISSN 1054-4887

The ACES Journal is abstracted in INSPEC, in Engineering Index, DTIC, Science Citation Index Expanded, the Research Alert, and to Current Contents/Engineering, Computing & Technology.

The illustrations on the front cover have been obtained from the ARC research group at the Department of Electrical Engineering, Colorado School of Mines

Published, sold and distributed by: River Publishers, Alsbjergvej 10, 9260 Gistrup, Denmark

THE APPLIED COMPUTATIONAL ELECTROMAGNETICS SOCIETY

<http://aces-society.org>

EDITORS-IN-CHIEF

Atef Elsherbeni

Colorado School of Mines, EE Dept.
Golden, CO 80401, USA

Sami Barmada

University of Pisa, ESE Dept.
56122 Pisa, Italy

ASSOCIATE EDITORS

Maokun Li

Tsinghua University
Beijing 100084, China

Wei-Chung Weng

National Chi Nan University, EE Dept.
Puli, Nantou 54561, Taiwan

Paolo Mezzanotte

University of Perugia
I-06125 Perugia, Italy

Mauro Parise

University Campus Bio-Medico of Rome
00128 Rome, Italy

Alessandro Formisano

Seconda Università di Napoli
81031 CE, Italy

Luca Di Rienzo

Politecnico di Milano
20133 Milano, Italy

Yingsong Li

Harbin Engineering University
Harbin 150001, China

Piotr Gas

AGH University of Science and Technology
30-059 Krakow, Poland

Lei Zhao

Jiangsu Normal University
Jiangsu 221116, China

Riyadh Mansoor

Al-Muthanna University
Samawa, Al-Muthanna, Iraq

Long Li

Xidian University
Shaanxi, 710071, China

Sima Noghianian

Commscope
Sunnyvale, CA 94089, USA

Lijun Jiang

University of Hong Kong, EEE Dept.
Hong Kong

Steve J. Weiss

US Army Research Laboratory
Adelphi Laboratory Center (RDRL-SER-M)
Adelphi, MD 20783, USA

Nunzia Fontana

University of Pisa
56122 Pisa, Italy

Shinishihiro Ohnuki

Nihon University
Tokyo, Japan

Jiming Song

Iowa State University, ECE Dept.
Ames, IA 50011, USA

Stefano Selleri

DINFO - University of Florence
50139 Florence, Italy

Kubilay Sertel

The Ohio State University
Columbus, OH 43210, USA

Toni Bjorninen

Tampere University
Tampere, 33100, Finland

Yu Mao Wu

Fudan University
Shanghai 200433, China

Giulio Antonini

University of L'Aquila
67040 L'Aquila, Italy

Santanu Kumar Behera

National Institute of Technology
Rourkela-769008, India

Fatih Kaburcuk

Sivas Cumhuriyet University
Sivas 58140, Turkey

Antonio Musolino

University of Pisa
56126 Pisa, Italy

Daniele Romano

University of L'Aquila
67100 L'Aquila, Italy

Huseyin Savci

Istanbul Medipol University
34810 Beykoz, Istanbul

Abdul A. Arkadan

Colorado School of Mines, EE Dept.
Golden, CO 80401, USA

Alireza Baghai-Wadji

University of Cape Town
Cape Town, 7701, South Africa

Zhixiang Huang

Anhui University
China

Salvatore Campione

Sandia National Laboratories
Albuquerque, NM 87185, USA

Marco Arjona López

La Laguna Institute of Technology
Torreón, Coahuila 27266, Mexico

Amin Kargar Behbahani

Florida International University
Miami, FL 33174, USA

Ibrahim Mahariq

American University of the Middle East
Kuwait and University of
Turkish Aeronautical Association
Turkey

Kaikai Xu

University of Electronic Science
and Technology of China
China

Laila Marzall

University of Colorado, Boulder
Boulder, CO 80309, USA

Sheng Sun

University of Electronic Science and
Tech. of China
Sichuan 611731, China

EDITORIAL ASSISTANTS

Matthew J. Inman
University of Mississippi, EE Dept.
University, MS 38677, USA

Shanell Lopez
Colorado School of Mines, EE Dept.
Golden, CO 80401, USA

EMERITUS EDITORS-IN-CHIEF

Duncan C. Baker
EE Dept. U. of Pretoria
0002 Pretoria, South Africa

Allen Glisson
University of Mississippi, EE Dept.
University, MS 38677, USA

Ahmed Kishk
Concordia University, ECS Dept.
Montreal, QC H3G 1M8, Canada

Robert M. Bevensee
Box 812
Alamo, CA 94507-0516

Ozlem Kilic
Catholic University of America
Washington, DC 20064, USA

David E. Stein
USAF Scientific Advisory Board
Washington, DC 20330, USA

EMERITUS ASSOCIATE EDITORS

Yasushi Kanai
Niigata Inst. of Technology
Kashiwazaki, Japan

Mohamed Abouzahra
MIT Lincoln Laboratory
Lexington, MA, USA

Alexander Yakovlev
University of Mississippi, EE Dept.
University, MS 38677, USA

Levent Gurel
Bilkent University
Ankara, Turkey

Sami Barmada
University of Pisa, ESE Dept.
56122 Pisa, Italy

Ozlem Kilic
Catholic University of America
Washington, DC 20064, USA

Erdem Topsakal
Mississippi State University, EE Dept.
Mississippi State, MS 39762, USA

Alistair Duffy
De Montfort University
Leicester, UK

Fan Yang
Tsinghua University, EE Dept.
Beijing 100084, China

Rocco Rizzo
University of Pisa
56123 Pisa, Italy

Atif Shamim
King Abdullah University of Science and
Technology (KAUST)
Thuwal 23955, Saudi Arabia

William O'Keefe Coburn
US Army Research Laboratory
Adelphi, MD 20783, USA

Mohammed Hadi
Kuwait University, EE Dept.
Safat, Kuwait

Amedeo Capozzoli
Univerita di Naoli Federico II, DIETI
I-80125 Napoli, Italy

Wenxing Li
Harbin Engineering University
Harbin 150001, China

Qiang Ren
Beihang University
Beijing 100191, China

EMERITUS EDITORIAL ASSISTANTS

Khaleb ElMaghoub
Trimble Navigation/MIT
Boston, MA 02125, USA

Kyle Patel
Colorado School of Mines, EE Dept.
Golden, CO 80401, USA

Christina Bonnington
University of Mississippi, EE Dept.
University, MS 38677, USA

Anne Graham
University of Mississippi, EE Dept.
University, MS 38677, USA

Madison Lee
Colorado School of Mines, EE Dept.
Golen, CO 80401, USA

Allison Tanner
Colorado School of Mines, EE Dept.
Golden, CO 80401, USA

Mohamed Al Sharkawy
Arab Academy for Science and Technology, ECE Dept.
Alexandria, Egypt

DECEMBER 2023 REVIEWERS

Intan Sorfina Zainal Abidin
Ghulam Ahmad
Ebrahim Amiri
Alireza Baghai-Wadji
Thomas Bauernfeind
Billel Bentouhami
Malcolm M. Bibby
Gaowei Cai
Biswajit Dwivedy
Giacomo Giannetti
Alfredo Gomes Neto
Taha Imeci
Pankaj Jha

Ashutosh Kedar
Fabrizio Loreto
Rajesh Natarajan
Mahdi Oliaei
Shi Pu
Alain Reineix
Manthan Shah
M. Mohammadi Shirkolaei
Cui Zhen Sun
Kechen Wang
Erdem Yazgan
Shihyuan Yeh
Wei-Hua Zong

TABLE OF CONTENTS

A Passive Adaptive Metamaterial Radome based on PIN Diodes
Ting-Ting Ge, Ming-Shun Li, Wei Song, Kai-Jiang Xu, Ke-Xin Xing,
and Xin-Qing Sheng922

Uncertainty Quantification and Optimal Design of EV-WPT System Efficiency based on
Adaptive Gaussian Process Regression
Xinlei Shang, Linlin Xu, Quanyi Yu, Bo Li, Gang Lv, Yaodan Chi, and Tianhao Wang 929

Mitigation of Feed Horn Overlapping Condition for Multi-beam Parabolic Reflector
Antenna
Nur Faiqah Fauzi, Nurul Huda Abd Rahman, Yoshihide Yamada,
Robi'atun Adayiah Awang, and Idnin Pasya.....941

Inductive Reactance Isolated Dynamic Seawater Monopole Antenna of High Efficiency
Lihua Li, Shimin Feng, and Menglei Xiu 952

Design of Wilkinson Power Dividers with SITL Compensated Microstrip Bandpass
Filters
Ravee Phomloungsri, Somkuan Srisawat, Somchat Sonasang,
and Mitchai Chongcheawchamnan 958

A Symmetrical Fractal-based Balanced Branch-Line Coupler for Simultaneous Low- and
Mid-band 5G Frequencies Applications
Abdulkadir B. Shallah, Farid Zubir, Mohamad Kamal A. Rahim, and Zubaida Yusoff 965

Single-mode Condition and Bending Loss Analysis of Ultrafast Laser-inscribed
Mid-infrared Waveguides in GeAsSe Chalcogenide Glass
Takashi Yasui975

An Investigation of the Relationship between Effective Relative Permittivity and
Infill Density in a 3D Printed Slab
Bibek Kattel, Winn Elliott Hutchcraft, and Richard K. Gordon 981

Resonant Frequency Modelling of Microstrip Antennas by Consensus Network and Student's-T Process Xuefeng Ren, Yubo Tian, Qing Li, and Hao Fu	987
Multi-polarized Reconfigurable Antenna with Ground Plane Slot and Capacitance Feeding for UAV-to-everything Communications Seong-Hyeop Ahn, Yu-Seong Choi, Mohamed Elhefnawy, and Wang-Sang Lee	998

A Passive Adaptive Metamaterial Radome based on PIN Diodes

Ting-Ting Ge¹, Ming-Shun Li¹, Wei Song^{1*}, Kai-Jiang Xu², Ke-Xin Xing¹,
and Xin-Qing Sheng¹

¹Beijing Institute of Technology
Beijing, China

²Aerospace Information Research Institute
Chinese Academy of Sciences
wsong@bit.edu.cn

Abstract – Automatic protection of EM detecting systems from unexpected high-power incidence is important to the robustness and life of a passive detecting system. In this paper, an adaptive metamaterial radome which automatically shields the receiving antenna from strong incident wave is designed. Based on standard wire medium, PIN diodes are added between adjacent wires. When the incident EM wave is weak, the diodes are in “off” state and affect little to the transmission of the wire medium. When the incident EM wave is strong enough to turn the diodes to “on” state, electric currents will be automatically formed in the diodes and the power transmitted to the antenna will be largely reduced. The adaptive transmission of the proposed radome is validated by the simulation and measurement results.

Index Terms – Metamaterial, radome, tunable devices, wire media.

I. INTRODUCTION

Conventional radomes are used to provide physical protection for the antenna from its environment (wind, rain, sand, ice, etc.) [1], but new radomes also face the increasing technical requirements such as regulating electromagnetic (EM) beams. For example, EM metamaterials are introduced in radomes to provide functions such as improving the gain, changing the polarization of the antenna, and filtering the electromagnetic waves [2–5]. Metamaterials or metamaterials-inspired structures [6, 7] generally present frequency-selective properties. So metamaterials-incorporated devices can avoid out-of-band electromagnetic interference [8].

Wire medium is a classic type of metamaterial [9–14]. As shown in [15], a standard wire medium aligned in the z -axis with square lattice has anisotropic permittivity as

$$\bar{\epsilon} = \begin{bmatrix} \epsilon_0 & 0 & 0 \\ 0 & \epsilon_0 & 0 \\ 0 & 0 & \epsilon \end{bmatrix}, \quad (1)$$

where

$$\epsilon = \epsilon_0 \left(1 - \frac{k_0^2}{k^2 - q_z^2} \right), \quad (2)$$

and k_0 , q_z are defined in [15].

In this medium, transmission line mode can be supported. When the length of the wire is properly designed, the wire medium reaches Fabry-Perot resonance and can provide high transmission for all angle incidence with subwavelength details in this canalization status [9, 10].

In metamaterial designs, active devices are utilized to provide flexibility for various applications [16–20]. Active metamaterials are also used in radomes to regulate the beams to enhance the angular stability [21] or to actively control the transmission [22–24]. However, for a detecting system, unexpected high-power incidence of EM waves is fatal and will affect the robustness of the detecting system. In this case, active metamaterials are not so effective in harnessing the EM waves because the state of the incidence is not known in advance.

In this paper, we propose an adaptive passive radome based on PIN diodes incorporated wire medium. This radome provides high transmission for low-power EM incidence. However, if the EM incidence is strong enough, the transmission will be dramatically reduced automatically. The mechanism of the radome is as follows. When working in a low-power incidence scenario, the PIN diodes are in “off” state and have little effect on the canalization working status of the wire medium. So high transmission is supported in the wire medium. When the incidence is so strong as to turn the PIN diodes to “on” state, forward currents will be formed between the PIN diodes, forming a shielding net in the wire medium, destroying the canalization status of the wire medium, and causing low transmission in the radome. Thus, adaptive transmission and automatic protection for the passive detecting system is realized from the hardware point of view, and it will significantly enhance the robustness and lifetime of a detecting system.

The operating mechanism is detailed below. The proposed radome was simulated by software CST Microwave Studio, with the diodes modeled by its equivalent circuits. Further, it was fabricated and measured, with its function verified by measurement results.

II. DESIGN OF THE RADOME

The proposed metamaterial radome consists of a standard wire medium. On a plane normal to the wires, a layer of PIN diodes is added connecting the neighboring wires. A thin dielectric layer is added to support the diodes, on which a metallic circuit is printed to connect the diodes to the wires, as shown in Fig. 1.

The proposed radome is based on the transmission properties of the standard wire medium and the turn-on characteristics of the PIN diodes. The standard wire medium can be designed to work in the canalization status. That is, when the length of the metal wire is integer multiples of half-wavelength, the wire medium reaches Fabry-Perot resonance. Under such resonance, the wire medium experiences total wave transmission for all angles of the incident wave [7–8]. Since the lattice constant of the wire medium relates to the resolution of transmission, it should be designed sufficiently small to capture the detailed information of the transmitted EM wave.

Moreover, transmission line (TEM) mode is supported in the canalization status [7]. So, as shown in Fig. 2 (a), the transverse electric field between the metallic rods can provide a bias for the PIN diodes, providing us the chance to add semiconductors to dynamically adjust the transmission characteristics of the wire media.

Hence, a layer of PIN diodes is integrated, as illustrated in Fig. 2 (b). While the wire medium works in canalization status, when the incident power is not so strong as to turn the diodes on, the PIN diodes stay in “off” state and the diode array is equivalent to a layer of dielectric plane. In this case the canalization status of the wire medium will be largely preserved, leading to high transmission characteristics of the radome. When

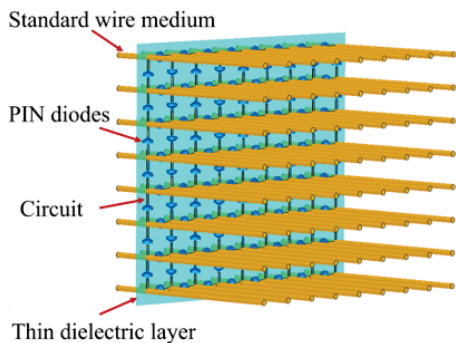


Fig. 1. Structure of the proposed radome.

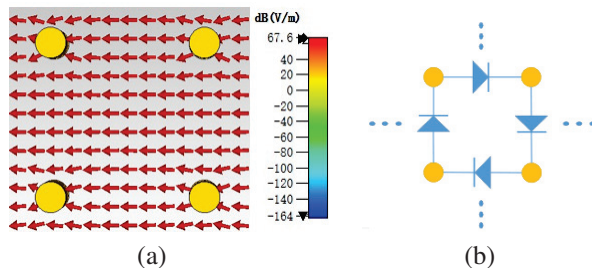


Fig. 2. Scheme of PIN diodes integration in the wire medium: (a) CST result of electric field in a standard wire medium in the canalization status, (b) diode integration scheme.

the incident power is so strong that the transverse electric fields between adjacent wires exceed the turn-on voltage of the diodes, the diodes will be turned on, and a forward current will be formed through the sheet.

Thus, an equivalent metallic net is generated on the diode layer, reflecting the incident electromagnetic waves automatically. With the canalization state of the wire medium destroyed by the forward currents, the radome shows low transmission.

III. SIMULATION ANALYSIS

A. The simulation models

The wire medium modeled consists of copper rods with diameter 2 mm and length 150 mm (2.5 wavelengths under 5 GHz). These rods form a 40×33 array in a square lattice with lattice constant of 10 mm. Near one end (20 mm away from the end) of the wire medium, a thin F4B sheet with thickness 0.508 mm, and $\epsilon_r = 2.2$ is used as the support medium for the diode array. On this sheet periodical holes are arranged for the metallic rods to go through. Between the holes, short metallic wires with width 0.3 mm are printed as a circuit to connect a PIN diode to its neighboring rods. The diode considered is the RF PIN diode BAR64-5 of Infineon Corporation. According to [25], the photo, the hardware basing circuit, and the equivalent circuit (EC) for the PIN diode (D1) used in the design is shown in Fig. 3. The operating frequency of the diode is 5 GHz, which is beyond the highest specified frequency by the manufacturer [25]. As the EC parameters for the design are not provided by the manufacturer, in this paper, the diode parameters were extracted from the measured S-parameters of the diode [26]. The extracted parameters are $R_s = 3 \Omega$, $L = 1.8 \text{ nH}$, $C_T = 0.22 \text{ pF}$, and $R_p = 2850 \Omega$.

Two horn antennas operating at 5 GHz are modeled as the transmitter and receiver, as shown in Fig. 4 (a). An observation plane is defined as a plane transverse to the wave transmission between the wire medium and the receiver. On this plane, the electric field is sampled to calculate the transmission of the radome.

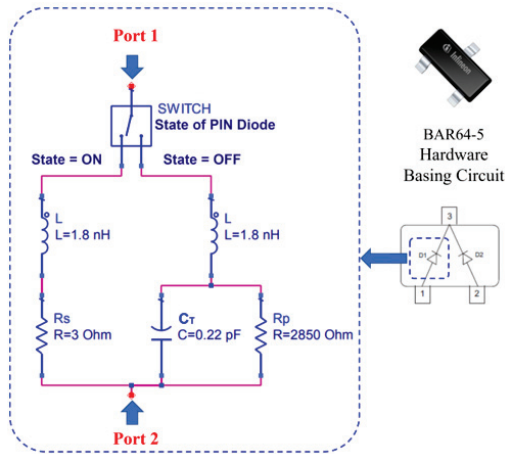


Fig. 3. The photo, the hardware basing circuit, and the equivalent circuit of the PIN diode (D1) used in the design under “on” or “off” states.

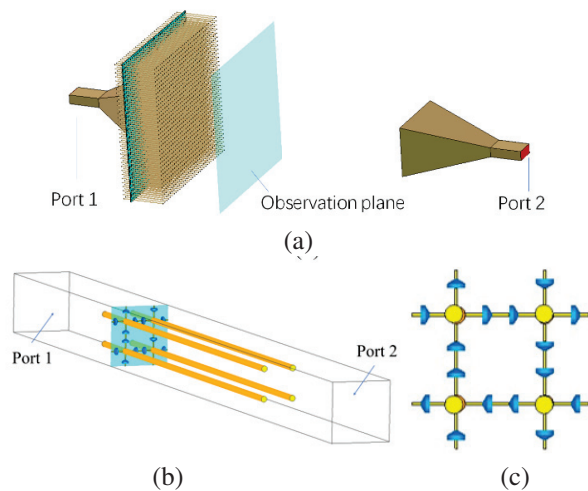


Fig. 4. Illustration of the proposed radome: (a) The finite sized model, (b) the unit cell model, and (c) the cut plane where diodes are integrated.

Apart from the above model, unit cell models for diode “on” and “off” states are also used to study the proposed radome with sufficient periodicity. In the unit cell model, for the convenience of modelling, each PIN diode is separated into a pair of serially connected identical PIN diodes, as shown in Fig. 4 (c).

In both the finite structure model and unit cell model, a radome formed by the same standard wire medium without diodes and the F4B sheet is used as a reference.

B. Simulation results

With the finite model shown in Fig. 4 (a), the S parameters were calculated. Figure 5 shows that the

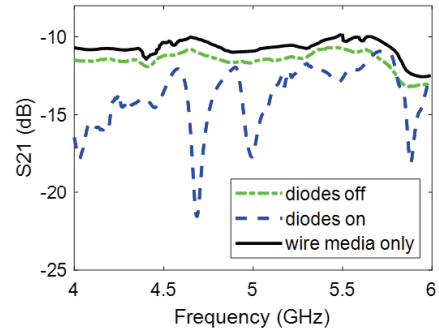


Fig. 5. The transmission coefficients of the radomes.

difference in S21 between the proposed radome with Diodes “off” and the reference radome is generally less than 1 dB. It indicates the proposed radome only slightly degrades the transmission when the diodes stay off. When the diodes are turned on by strong incidence, the transmission gets obviously reduced. Compared with that of the reference, this difference reaches 6.6 dB at 5 GHz.

The amplitudes of electric field on the observation plane in the near field are compared in Fig. 6. It can be seen that the field distribution of the radome with diodes “off” is similar to that from a horn antenna with a reference radome. That is because in “off” state, known from the EC model, the impedance of the diode is very high, leading to small leakage currents between the metallic wires. So, compared to that in the case of standard

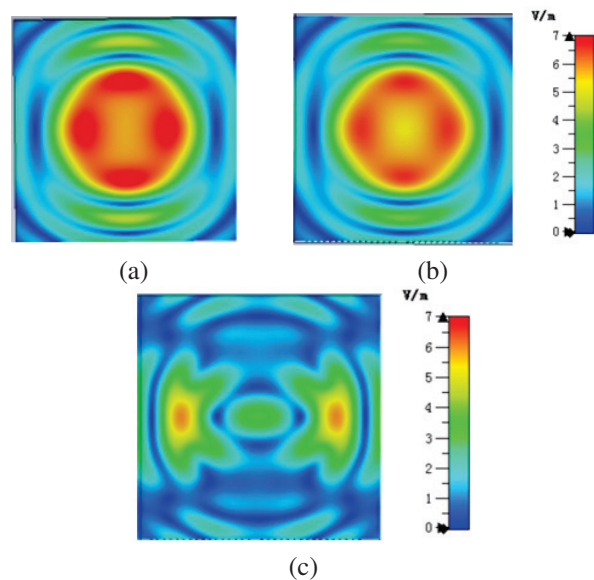


Fig. 6. Simulated electric field distribution on the observation plan: (a) The reference radome, (b) radome with diodes “off,” and (c) radome with diodes “on.”

wire medium, the leakage currents have little effect on the transverse field between the metallic wires. Consequently, the canalization status of wire medium is largely preserved. However, with diodes “on,” the impedance of the diode is small and the leakage currents between the metallic wires are large. The large leakage currents form a current net in the diode plane, dramatically reducing the transverse electric field on that plane. Without the supporting of the transverse electric field, the canalization status of the wire medium disappears, and the EM wave transmitted through the radome will be largely reduced. That is why we can find significantly weaker electric field on the observation plane, as shown in Fig. 6 (c), which demonstrates an obvious shielding effect of the radome.

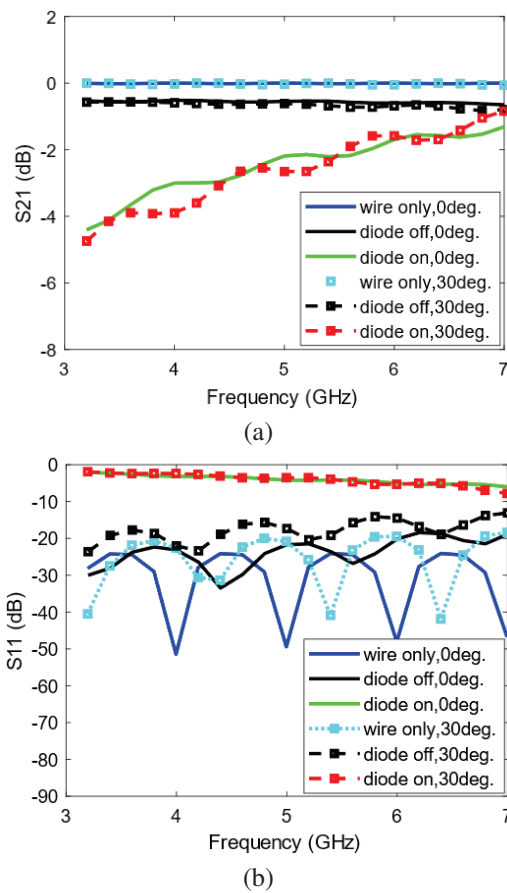


Fig. 7. The transmission and reflection of the three radomes under unit-cell models with different incident angles: (a) S21 and (b) S11.

The reflection and transmission coefficients of the proposed radome are simulated with unit cell models. The incident angles of 0 and 30 degrees were investigated. As shown in Fig. 7, for the reference radome, the simulated transmission is 0 dB, both for the normal inci-

dence case and the oblique incidence one. As for the radome with the diodes in “off” state, the S21 is around -0.6 dB for the normal or the oblique incidence cases, indicating that high transmission is supported, which is affected little by the incident angle. However, when the diodes are on, the proposed radome has highest reflection and lowest transmission for both cases. Specifically, the S11 results are about -3.5 dB at 5 GHz and the S21 results are low. While when the diodes are off, the reflection is around -20 dB, and the transmission is over -1 dB for either incidence.

IV. EXPERIMENTAL RESULTS

The proposed radome as investigated in Section III was fabricated by using copper rods, F4B and RF PIN diodes BAR64 of Infineon Corporation. In order to generate a strong incident electromagnetic wave to turn the diodes on, a power amplifier with output power of 39 dBm was used for feeding the antenna when the “on” state of the diode is required. Circulator and attenuators are utilized in the measurement system for protection measurement for high-power case. The near fields from the radome are scanned as shown in Fig. 8. The scan plane is 5 wavelengths (300 mm) away from the radome.

As shown in Fig. 9, the measured field distributions show similar trends to the simulation results. When the input signal is weak, which cannot turn on the diodes, the electric field on the observation plane has a similar distribution pattern to that without the radome. When the high-power amplifier is used, the incident electric field is so strong that the diodes are turned on, and the electric field, as shown in Fig. 9 (c), gets reduced by more than 3 dB on the observation plane compared with Fig. 9 (b). To some degree, the proposed radome reaches the goal to shield the receiver from strong electromagnetic wave.

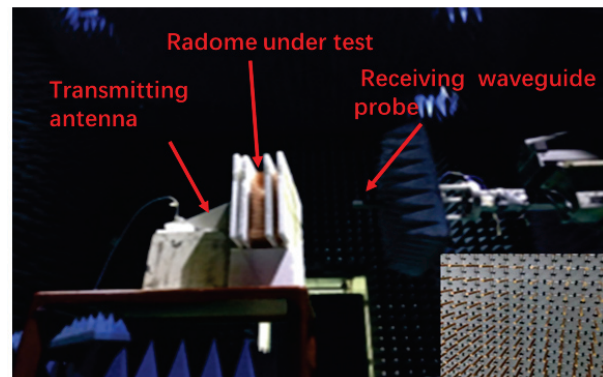


Fig. 8. Measurement environment and the details of the fabricated radome (lower right-hand corner)

Figure 9 also shows that the field amplitude in the case with the radome under low-power incidence is evi-

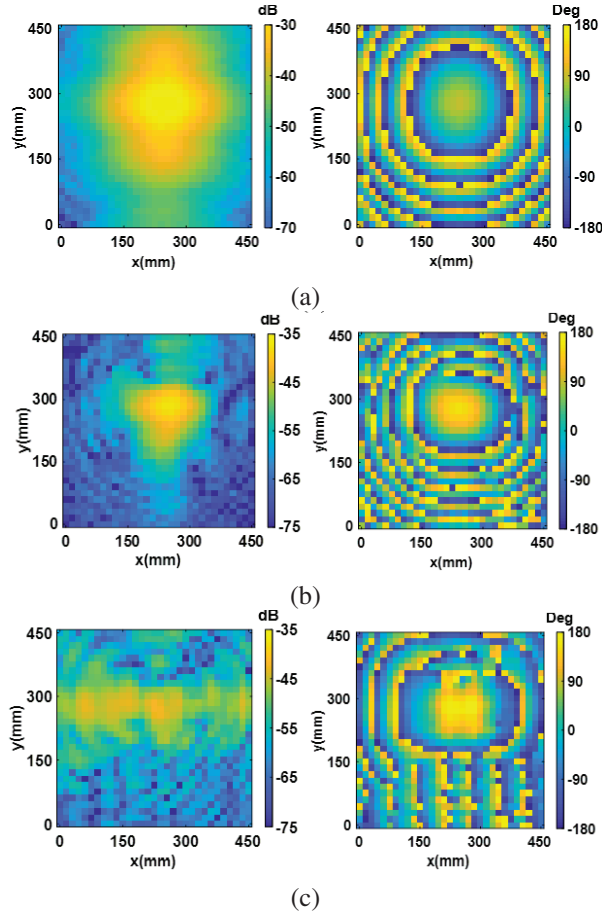


Fig. 9. Near-field scanning results of field intensity and phase distribution: (a) Antenna without radome, (b) antenna with radome under low-power incidence, and (c) antenna with radome under high-power incidence.

dently smaller than that without the radome. The diode-integrated wire medium radome introduces larger losses in physical measurement than in simulation. The reasons are as follows:

1. The F4B board, the printed circuit, and the welding of the PIN diodes bring greater loss to the transmission channel in measurement than in simulation, which affected the transmission of the radome.
2. The manufacturing of the wire medium in the radome was not precise enough; e.g., some metallic rods were not sufficiently parallel.
3. The diode's equivalent circuit model is based on circuit tests with voltage bias instead of EM wave scattering experiments. So, the equivalent circuit model is not sufficiently accurate when predicting its EM scattering effect.

Table 1: Comparison of self-tuning radomes (radome function: low power transmission, and high power absorption)

Ref.	Structure	Freq. (GHz)	Verification	
			Sim.	Meas.
[20]	Metasurface+PIN diodes	2.5	✓	○
[21]	Metasurface+PIN diodes	6.5	✓	○
This work	Metamaterial+PIN diodes	5	✓	✓

The comparison between the proposed radome and other self-tuning radomes in the literature is made in Table 1.

V. CONCLUSIONS

In this paper, a passive metamaterial radome based on PIN diodes is proposed, to automatically shield the receiver from high-power EM incidence and protect the receiver system. The mechanism of the radome is explained. Simulation results show that the proposed radome shows obviously different transmission property under diodes “off” and “on” states. The reflection is around -20 dB with diodes “off,” while it is -3.5 dB with diodes “on.” Experimental results show that the transmission also gets reduced by more than 3 dB, when the receiver is illuminated by strong incidence with power of 39dBm, compared with the weak incident power case.

REFERENCES

- [1] M. Latrach, H. Rmili, C. Sabatier, E. Seguenot, and S. Toutain, “Design of a new type of metamaterial radome for low frequencies,” *Microwave and Optical Technology Letters*, vol. 52, no. 5, pp. 1119-1123, 2010.
- [2] G. V. Trentini, “Partially reflecting sheet arrays,” *Ire Transactions on Antennas & Propagation*, vol. 4, no. 4, pp. 666-671, 1956.
- [3] A. P. Feresidis and J. C. Vardaxoglou, “High gain planar antenna using optimised partially reflective surfaces,” *Microwaves Antennas & Propagation Iee Proceedings*, vol. 148, no. 6, pp. 345-350, 2001.
- [4] A. P. Feresidis, G. Goussetis, S. Wang, and J. C. Vardaxoglou, “Artificial magnetic conductor surfaces and their application to low-profile high-gain planar antennas,” *IEEE Transactions on Antennas and Propagation*, vol. 53, no. 1, pp. 209-215, 2005.
- [5] Z.-J. Han, W. Song, and X.-Q. Sheng, “Broadband circularly polarized antenna by using polarization conversion metasurface,” *Applied Computational Electromagnetics Society (ACES) Journal*, vol. 35, no. 6, pp. 656-661, June 2020.

- [6] P. Jha, A. Kumar, A. De, and R. K. Jain, "CPW-fed metamaterial inspired compact multiband antenna for LTE/5G/WLAN communication," *Frequenz*, vol. 76, no. 7-8, pp. 401-407, 2022.
- [7] P. Jha, A. Kumar, and N. Sharma, "A metamaterial inspired split ring resonator accomplished multi-band antenna for 5G and other wireless applications," *Revue Roumaine des Sciences Techniques, Série Électrotechnique et Énergétique*, vol. 68, no. 2, pp. 127-131, 2023.
- [8] H. Zhou, S. Qu, B.-Q. Lin, J. Wang, H. Ma, Z. Xu, W. Peng, and P. Bai, "Filter-antenna consisting of conical FSS radome and monopole antenna," *IEEE Transactions on Antennas & Propagation*, vol. 60, no. ISOCC, pp. 3040-3045, 2012.
- [9] P. A. Belov and C. R. Simovski, "Canalization of subwavelength images by electromagnetic crystals," *PIERS Online*, vol. 1, no. 1, pp. 37-41, 2005.
- [10] P. A. Belov, Y. Hao, and S. Sudhakaran, "Subwavelength imaging by a slab of wire medium," *IEEE Antennas and Propagation Society International Symposium*, pp. 4515-4518, 2006.
- [11] P. A. Belov and M. G. Silveirinha, "Resolution of subwavelength transmission devices formed by a wire media," *Physical Review E*, vol. 73, no. 2, pp. 645-666, 2006.
- [12] X. Radu, A. Lapeyronnie, and C. Craeye, "Numerical and experimental analysis of a wire medium collimator for magnetic resonance imaging," *Electromagnetics*, vol. 28, no. 7, pp. 531-543, 2008.
- [13] S. Kosulnikov, D. Filonov, S. Glybovski, P. Belov, S. Tretyakov, and C. Simovski, "Wire-medium hyperlens for enhancing radiation from subwavelength dipole sources," *IEEE Transactions on Antennas & Propagation*, vol. 63, no. 11, pp. 4848-4856, 2015.
- [14] S. Kosulnikov, M. Mirmoosa, D. Vovchuk, S. Tretyakov, S. Glybovski, and C. Simovski, "Enhancement of radiation with irregular wire media," *IEEE Transactions on Antennas & Propagation*, 2016.
- [15] P. Belov, R. Marqués, S. Maslovski, I. Nefedov, M. Silveirinha, C. Simovski, and S. Tretyakov, "Strong spatial dispersion in wire media in the very large wavelength limit," *Physical Review B*, vol. 67, no. 11, pp. 113103, 2003.
- [16] J. P. Turpin, D. H. Werner, and D. E. Wolfe, "Design considerations for spatially reconfigurable metamaterials," *IEEE Transactions on Antennas and Propagation*, vol. 63, no. 8, pp. 3513-3521, 2015.
- [17] Y. Luo, K. Qin, H. Ke, B. Xu, S. Xu, and G. Yang, "An active metamaterial antenna with beam scanning manipulation based on a digitally-modulated array factor method," *IEEE Transactions on Antennas and Propagation*, no. 99, pp. 1-1, 2021.
- [18] M. M. Shirkolaei and J. Ghalibafan, "Magnetically scannable slotted waveguide antenna based on the ferrite with gain enhancement," *Waves in Random and Complex Media*, pp. 1-11, 2021.
- [19] M. Shirkolaei and M. Aslinezhad, "Substrate integrated waveguide filter based on the magnetized ferrite with tunable capability," *Microwave and Optical Technology Letters*, vol. 63, no. 4, pp. 1120-1125, 2021.
- [20] M. M. Shirkolaei and J. Ghalibafan, "Unbalanced CRLH behavior of ferrite-loaded waveguide operated below cutoff frequency," *Waves in Random and Complex Media*, vol. 32, no. 2, pp. 755-770, 2022.
- [21] H. Bai, M.-B. Yan, W. Li, J. Wang, L. Zheng, H. Wang, and S. Qu, "Tunable frequency selective surface with angular stability," *IEEE Antennas and Wireless Propagation Letters*, vol. 20, no. 6, pp. 1108-1112, 2021.
- [22] Y. Zhao, J. Fu, Z. Liang, Z. Wang, Z. Zhang, B. Lv, and W. Chen, "Reconfigurable active frequency selective surface for ultra-wideband applications," *International Journal of RF and Microwave Computer-Aided Engineering*, no. 5, pp. e22222, 2020.
- [23] K. Wang, P. Liu, and H. Liu, "A miniaturized, low-profile, self-actuated radome for EM protection," *International Applied Computational Electromagnetics Society Symposium (ACES)*, Suzhou, China, pp. 1-2, 2017.
- [24] Y. J. Zhou, H. X. Xu, Q. Y. Li, X. B. Wu, and S. Y. Xiao, "Active self-tuning metasurface radome for high-power microwave," *CIE International Conference on Radar (Radar)*, Haikou, Hainan, China, pp. 2719-2722, 2021.
- [25] Data sheet of the RF PIN diode of Infineon Corporation with model of BAR64-5. https://www.infineon.com/dgdl/Infineon-BAR64-05-DS-v01_01-EN.pdf?fileId=5546d462689a790c01690f026ce63904.
- [26] PIN SPAR data sheet of the RF PIN diode of Infineon Corporation. <https://www.infineon.com/cms/cn/product/rf/rf-diode/rf-pin-diode/antenna-switch/bar64-05/#!/?fileId=5546d46269e1c0190169ecdea94b46e8>.



Ting-Ting Ge received her B.E. degree from North China University of Technology, Beijing, China, in 2019, and her M.S. degree from the Beijing Institute of Technology, Beijing, China, in 2022. Her current research interests include EM property analysis, and metamaterial-based antenna design.



Ming-Shun Li received his B.E. degree in electronic information engineering from Dalian Maritime University in 2020 and the Master's degree in electronic science and technology from Beijing Institute of Technology in 2023. His current research interests include wideband circularly polarized antenna design, low RCS antenna design, and electromagnetic metasurface design.



Wei Song received her Bachelor's degree from North Eastern University, Shen-yang, China, in 2002, and her M.Sc. and Ph.D. degrees from Queen Mary, University of London, London, UK, in 2003 and 2008 respectively. She is currently an associate professor with the School of Integration Circuit and Electronics, Beijing Institute of Technology, Beijing, China. She has authored or co-authored over 40 papers in refereed journals and international conferences, and has co-authored a monograph in computational electromagnetics. Her current research interests include high-performance methods in computational electromagnetics, metamaterial EM property analysis, and metamaterial-based antenna design.



Kai-Jiang Xu received the B.E. degree from the School of Electronic Information Engineering, Anhui University, Hefei, China, in 2011, and the Ph.D. degree in the Center for Electromagnetic Simulation, School of Information and Electronics, Beijing Institute of Technology, Beijing, China, in 2018. He is currently a research assistant fellow with the Aerospace Information Research Institute, Chinese Academy of Sciences, Beijing. His current research interests include antenna design and applied computational electromagnetics.



Ke-Xin Xing received her B.E. degree from Hefei University of Technology, Hefei, China, in 2021, and she is currently pursuing the M.S. degree at the Institute of Radio Frequency Technology and Software from Beijing Institute of Technology. Her current research interests include EM property analysis and metamaterial-based antenna design.



Xin-Qing Sheng received his B.S., M.S. and Ph.D. degrees from the University of Science and Technology of China (USTC), Hefei, China, in 1991, 1994, and 1996, respectively. Sheng is a Chang-Jiang Professor of the School of Integration Circuit and Electronics at the Beijing Institute of Technology. Sheng has authored and co-authored over 150 papers in refereed journals, and three books: *Essentials of Computational Electromagnetics* (Singapore: IEEE Press-Wiley, 2012), *A Brief Treatise on Computational Electromagnetics* (Beijing: Science Press, 2004), and *A Treatise on Electromagnetic Waves* (Beijing: Science Press, 2007). Sheng authored SINOCOM, a simulation software for scattering by complex targets. His research interests include computational electromagnetics, scattering and antenna analysis, electromagnetic compatibility, and microwave imaging.

Uncertainty Quantification and Optimal Design of EV-WPT System Efficiency based on Adaptive Gaussian Process Regression

Xinlei Shang¹, Linlin Xu¹, Quanyi Yu¹, Bo Li¹, Gang Lv², Yaodan Chi³, and Tianhao Wang^{1*}

¹College of Instrument and Electrical Engineering
Jilin University, Changchun, 130026, China

shangxinlei@jlu.edu.cn, xull21@mails.jlu.edu.cn, qyyu20@mails.jlu.edu.cn,
libo21@mails.jlu.edu.cn, *wangtianhao@jlu.edu.cn

²EMC Department National Automotive Quality Supervision and Inspection Center
Changchun, 130011, China
lvgang@catc.com.cn

³Jilin Provincial Key Laboratory of Architectural Electricity and Comprehensive Energy Saving
Jilin Jianzhu University Changchun, 130118, China
chiyaodan@jlju.edu.cn

Abstract – Wireless power transfer (WPT) is a safe, convenient, and intelligent charging solution for electric vehicles. To address the problem of the susceptibility of transmission efficiency to large uncertainties owing to differences in coil and circuit element processing and actual driving levels, this study proposes the use of adaptive Gaussian process regression (aGPR) for the uncertainty quantification of efficiency. A WPT system efficiency aGPR surrogate model is constructed with a set of selected small-sample data, and the confidence interval and probability density function of the transmission efficiency are predicted. Finally, the reptile search algorithm is used to optimize the structure of the WPT system to improve efficiency.

Index Terms – Adaptive Gaussian process regression (aGPR), electric vehicle (EV), optimal design, uncertainty quantification (UQ), wireless power transfer (WPT).

I. INTRODUCTION

With the rapid development of electric vehicle (EV) technology, its charging methods have also improved [1]. In response to the drawbacks of cable charging methods, wireless power transfer (WPT) technology was designed to remove the mechanical interface, improve safety, and enable dynamic charging. The technology is advanced, maturing gradually [2, 3], and a promising mainstream EV charging technology in the future [4]. Many scholars examined the issues related to EV-WPT systems and developed international standards [5]. However, owing to the complex design and control of the transfer system

and differences in actual driving levels, each factor in the coil structure, transfer distance, misalignment, and compensation topology design can directly or indirectly impact the efficiency of the system [6–8]. As the uncertainty of the aforementioned relevant factors as input parameters will have a significant impact on WPT system efficiency, conducting uncertainty quantification (UQ) evaluation and optimization studies on the efficiency of EV-WPT systems is important.

Parametric UQ methods include statistical and non-statistical methods, among which the statistical methods are dominated by the Monte Carlo (MC) method and its improvements, which are typically used to verify the accuracy of other UQ methods [9]. Owing to the complexity and high computational cost of an experimental system, nonstatistical methods based on the generalized polynomial chaos expansion (gPCE) method, machine learning, deep learning, and the Kriging surrogate model are widely used in UQ studies. Rossi et al. [10] combined gPCE theory with an effective model of interactions among devices in the radiative near field to build a UQ framework for the efficiency of WPT systems and demonstrated that the method is more flexible and efficient than the stochastic configuration method, based on a single gPCE and direct MC analysis; however, the mapping solving process of the PCE surrogate model suffers from the problem of the “curse of dimensionality” [11]. With the development of artificial intelligence, machine learning has gradually been employed in the field of WPT electromagnetic compatibility. Trincherio et al. [12] examined leastsquares support vector machine (LS-SVM) regression and its optimized form for WPT

efficiency UQ and demonstrated that LS-SVM regression, based on kernel technology, can effectively solve the high-dimensional spatial nonlinear UQ problem, but the hyperparameter selection lacks a priori knowledge and cannot be realized based on a rigorous mathematical basis. Larbi et al. [13] employed LS-SVM regression, combined with Gaussian process regression (GPR), for WPT system UQ. Based on the quantification results, the authors used partial least squares regression for the sensitivity analysis of the parameters and system efficiency optimization but obtained poor prediction results for the regions with a low probability of occurrence. Other scholars applied the Kriging surrogate model [14] and deep learning [15] to the UQ and optimization of simplified WPT systems, but UQ capability for the complex structure of WPT simulation models remains to be verified. The GPR method, based on Gaussian stochastic processes, kernel techniques, and Bayesian inference theory, can overcome the “curse of dimensionality” and follows a strict mathematical derivation of the hyperparameters while giving a more comprehensive uncertainty analysis than LS-SVM regression and adaptive sparse PCE [16]; however, the number of training samples can be further reduced to lessen the computational cost.

In terms of WPT efficiency optimization, Chen et al. [17] proposed a series-parallel hybrid resonant structure and optimized capacitor parameters to improve WPT efficiency while achieving a long transfer distance. Yang et al. [18] optimized the voltage gain and transmission efficiency by designing compensation parameters for series/series-parallel inductive power transfer systems. Meanwhile, Zhou et al. [19] employed a constrained adaptive particle swarm algorithm with a multi-objective function, using DC – DC input voltage as the decision variable to perform the multi-objective optimization of the output power and efficiency of a WPT system. The above studies showed that the optimization of the efficiency of WPT systems is influenced by a variety of parameters. Therefore, the optimization of EV-WPT transmission efficiency based on UQ can, on the one hand, fully consider the practical application of WPT systems and, on the other hand, provide a reference for improving the robustness of such systems.

To address the shortcomings of the above studies, an information entropy adaptive sampling strategy is used in this study to build an adaptive GPR (aGPR) surrogate model to quantify the transmission efficiency uncertainty and compare it with the MC method and GPR UQ results. Based on the UQ, the efficient reptile search algorithm (RSA) is combined to optimize the component parameters in the compensation network to improve transmission efficiency and system robustness.

The main contents of this paper are as follows: Section II introduces the EV-WPT system numerical

simulation model, and Section III builds an aGPR-based transmission efficiency UQ framework for an EV-WPT system. Section IV presents the application of the RSA in the transmission efficiency prediction and overall system optimization, and Section V describes the specific experimental procedure for verifying the UQ capability of the aGPR model and effectiveness of the optimization scheme. Finally, Section VI summarizes the whole work.

II. NUMERICAL SIMULATION MODEL OF EV-WPT SYSTEM

Based on the principle of magnetic coupling resonance, this study uses space alternating magnetic fields to transfer power and establishes a simulation model of a magnetically coupled resonant EV-WPT system by COMSOL software. The working frequency of the system is 85kHz and the output power is 3 kW.

Figure 1 (a) presents an overall model of EVs, referring to most family car models on the market, with a design body size of 4500 mm \times 2000 mm \times 1500 mm and material of mainly aluminum, ignoring other non-electromagnetic materials. Figure 1 (b) shows a square magnetic coupling mechanism, the inner side of which is the power transfer coil group consisting of transmitting and receiving coils, with an outer contour size of 600 mm \times 600 mm and an inner contour size of 300 mm \times 300 mm. The vertical distance d of the transceiver coil is within the range of 100-150 mm, the number of turns of the coil on each side is 11, the conductor material is copper, and the radius of the cross-section r_0 is 0.8 mm. The outer side of the coil group is covered with ferrite of the same size as the outer contour of the transfer coil, with a thickness of 10 mm, which can improve the coupling coefficient and reduce magnetic field leakage, thereby improving transmission efficiency. The scale factor l is

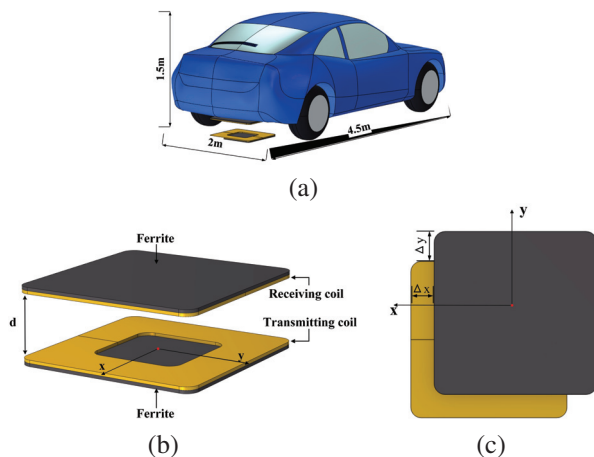


Fig. 1. EV with WPT and magnetically coupled mechanism.

defined as the scaling of the dimensions of the square transceiver coils to their square centers (e.g., the dot in Fig. 1 (b)), and Δx and Δy are the misalignment of the coupling mechanism in the horizontal x - and y -axis directions, respectively, as shown in Fig. 1 (c).

As WPT coils typically have a small coupling coefficient, S-S and parallel-series topologies are highly suitable for efficient WPT systems [20]. To further enhance the transmission power, an S-S compensation circuit is used in this study, as shown in Fig. 2, where I_S is the AC current source, R_T is the equivalent resistance of the transmitting loop, R_R is the equivalent resistance of the receiving loop, R_L is the load resistance, C_T and C_R are compensation capacitors at the transmitting and receiving end, respectively, L_T and L_R are the equivalent inductance of the transmitting and receiving coils, respectively, and M is the mutual inductance between the two coils. When resonance is generated between the two coils, the efficiency of the power transfer in the system will be [21]:

$$\eta = \frac{R_L}{R_R + R_L} \frac{\omega^2 M^2}{\omega^2 M^2 + R_T(R_R + R_L)}, \quad (1)$$

where $R_Z = R_R + R_L$, ω is the resonant angular frequency.

In practice, differences exist in the manufacturing of coils and circuit components and in the operations of the driver, which may lead to uncertainty in the coil dimensions and circuit element parameters and misalignment of the transmitting and receiving coil packs, thereby affecting the mutual inductance and mutual coupling coefficient. Such differences may also inevitably cause uncertainty in the transmission efficiency of EV-WPT systems. Therefore, typical deterministic studies are not representative, and UQ studies on EV-WPT efficiency must be conducted statistically to analyze the extent to which efficiency is affected by multiple factors. This study focuses on the UQ of EV-WPT system efficiency under misalignment, physical dimensions, and component parameters and further optimizes it. In the next section, a UQ framework for the transmission efficiency of an EV-WPT system is developed based on aGPR machine learning.

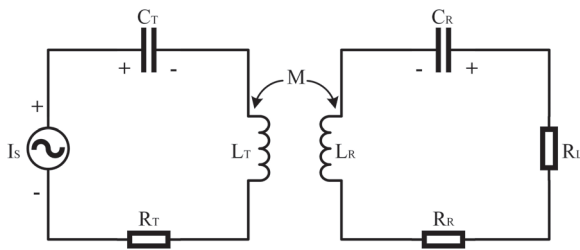


Fig. 2. Series-series (S-S) compensation circuit.

III. UQ OF EV-WPT TRANSMISSION EFFICIENCY BASED ON AGPR

A. GPR for transmission efficiency prediction GPR is a parameter-free stochastic process regression based on a Gaussian distribution, which can give probabilistic approximate predictions on the quantity of interest and calculate the predicted variance at each sample point in the input parameter space [22]. The Gaussian process is entirely determined by the mean function (trend) and covariance function (kernel function). The hyperparameters of the covariance function can be optimized when training the GP model. This study uses GPR to establish the correspondence between the d -D column vector of input parameters $\mathbf{x}_{p \times d}$ and transmission efficiency of the WPT system $\boldsymbol{\eta}_{n \times 1}$, then builds a surrogate model and quantifies the uncertainty.

Based on the function space perspective, the Gaussian process can be expressed as:

$$f(\mathbf{x}) \sim GP(m(\mathbf{x}), k_{\theta}(\mathbf{x}, \mathbf{x}')), \quad (2)$$

where θ is the hyperparameter of the covariance function, and $m(\mathbf{x})$ and $k_{\theta}(\mathbf{x}, \mathbf{x}')$ are the mean and covariance functions of the stochastic process $f(\mathbf{x})$, respectively [23]. The GPR learning problem for transmission efficiency is:

$$\boldsymbol{\eta} = f + \boldsymbol{\varepsilon}. \quad (3)$$

The GPR training process is shown in Fig. 3, where f is considered as a potential function, $\boldsymbol{\varepsilon}$ is the estimated noise of the GP, $\boldsymbol{\varepsilon} \sim \mathbf{N}(0, \sigma_n^2 \mathbf{I})$, and f_1, f_2, \dots, f_n satisfy the joint Gaussian distribution.

To simplify the calculation, let the prior trend of $\boldsymbol{\eta}$ constructed from the n training samples $(\mathbf{x}_{n \times d}, \boldsymbol{\eta}_{n \times 1})$ be $\boldsymbol{\eta} \sim \mathbf{N}(0, K_{ff} + \sigma_n^2 \mathbf{I})$ and the potential function constructed from the m testing samples be f^* . The joint prior distribution of $\boldsymbol{\eta}$ and f^* is:

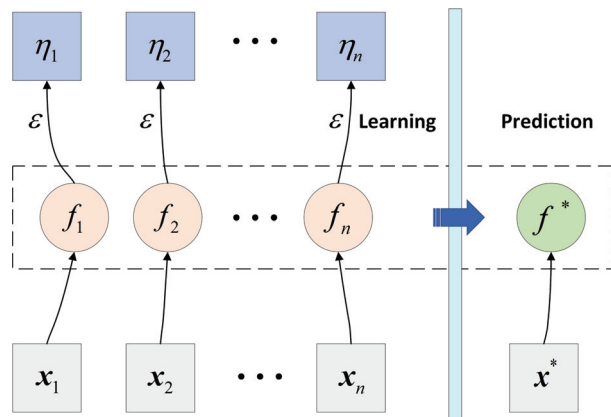


Fig. 3. GPR prediction process for transmission efficiency.

$$\begin{bmatrix} \boldsymbol{\eta} \\ \mathbf{f}^* \end{bmatrix} \sim N\left(\mathbf{0}, \begin{bmatrix} \mathbf{K}_{ff} + \sigma_n^2 \mathbf{I} & \mathbf{K}_{ff}^T \\ \mathbf{K}_{ff} & \mathbf{K}_{\psi^*} \end{bmatrix}\right) \quad (4)$$

where $\mathbf{K}_{ff}, \mathbf{K}_{**}, \mathbf{K}_{ff^*}$ are the covariance matrices between the training samples, testing samples, and the training and testing samples, respectively. The mean \bar{f}^* and variance σ_*^2 of the predicted distribution can be derived from Bayesian theory as:

$$\bar{f}^* = \mathbf{K}_{ff^*} (\mathbf{K}_{ff} + \sigma_n^2 \mathbf{I})^{-1} \boldsymbol{\eta}, \quad (5)$$

$$\sigma_*^2 = \mathbf{K}_{**} - \mathbf{K}_{ff^*} (\mathbf{K}_{ff} + \sigma_n^2 \mathbf{I})^{-1} \mathbf{K}_{ff^*}^T, \quad (6)$$

where \bar{f}^* gives the probabilistic approximate predicted value of the transmission efficiency, and σ_*^2 gives the uncertainty of the prediction.

1) Kernel function

Commonly used kernel functions are square kernels, that is, SE covariance, Matérn 3/2 kernel, and so on. As square kernels have a low solution complexity and low computational cost, this study applies the square kernel function to the regression analysis, as shown in (7):

$$k_{SE}(\mathbf{x}, \mathbf{x}') = \sigma_f^2 \exp\left(-\frac{1}{2\nu^2} \|\mathbf{x} - \mathbf{x}'\|^2\right). \quad (7)$$

2) Hyperparameters

In GPR, the various parameters and noise σ_n^2 in the kernel function are variable and collectively referred to as hyperparameters. The hyperparameters of the covariance function, mean function, and nugget factor are learned by finding the maximum value of the log marginal likelihood function (8) of the training samples $(\mathbf{x}_{n \times 0}, \boldsymbol{\eta}_{n \times 1})$, leading to the optimal hyperparameters:

$$\begin{aligned} & \log p(\boldsymbol{\eta} | \mathbf{x}) \\ &= -\frac{1}{2} \boldsymbol{\eta}^T (\mathbf{K}_{ff} + \sigma_n^2 \mathbf{I})^{-1} \boldsymbol{\eta} \\ & - \frac{1}{2} \log |\mathbf{K}_{ff} + \sigma_n^2 \mathbf{I}| - \frac{n}{2} \log 2\pi. \end{aligned} \quad (8)$$

Unconstrained nonlinear optimization algorithms can solve the GPR maximum likelihood estimation problem. Common methods are the conjugate gradient method and quasi-Newton method, but the solution complexity enhances as dimensionality increases. The Fmincon algorithm uses the interior point method, which is highly accurate and converges well but requires a suitable assigned initial value when optimizing. Classical stochastic optimization methods, such as genetic algorithms and particle swarm algorithms, have the advantage of not relying on initial values and using global search for optimality, which are less likely to fall into local optimality but prone to premature convergence and low accuracy [24]. However, the RSA has superior convergence and can improve accuracy [25]. Therefore, in

this study, the RSA is used for the GPR hyperparameter solution and compared with other stochastic optimization algorithms to verify the optimization-seeking capability.

A. Sampling strategy for aGPR training

The aGPR method allows the standard deviation σ_* at the transmission efficiency prediction point x to be the entropy $IE(x)$, according to the information entropy adaptive sampling strategy [26], as shown in (9). First, this strategy collects the specified samples from the candidate pool X_{cand} to the training pool and adds a new input parameter point x^{k+1} at the maximum value of the transmission efficiency prediction entropy, that is, the maximum standard deviation, as shown in (10), where k is the number of training samples. Second, the termination condition for the adaptive sampling is determined based on the transmission efficiency prediction accuracy, as shown in (11), which terminates the sampling when the maximum entropy decreases to δ . Each iteration fits and constructs a new GP such that the mean of the transmission efficiency prediction points can effectively approximate the true value of the transmission efficiency, maximize the accuracy of the surrogate model, and reduce the required number of training samples. The pseudo-code of aGPR is:

$$IE(x) = \sigma_*, \quad (9)$$

$$x^{k+1} = \underset{x \in X_{cand}}{\operatorname{argmax}} [IE(x)], \quad (10)$$

$$\max [IE(x)] \leq \delta. \quad (11)$$

Algorithm 1 aGPR training pseudo-code

Input: Training samples $\{x_1, \eta_1\}, \{x_2, \eta_2\}, \dots, \{x_n, \eta_n\}$, testing samples $\{x_*, \eta_*\}$, and the maximum entropy δ

Output: The mean and variance of prediction \mathbf{f}^* and σ_*^2

- 1 Initialize the kernel function and the hyperparameters based on (7),(8)
 - 2 **while** sampling isn't finished
 - 3 Calculate the covariance matrices $\mathbf{K}_{ff}, \mathbf{K}_{**}, \mathbf{K}_{ff^*}$, the best hyperparameters, the entropy $IE(x)$ based on (9) and a new input point x^{k+1} based on (10)
 - 4 **if** $IE(x) \leq \delta$ **then**
 - 5 Determine the minimum number of adaptive sampling
 - 6 **end**
 - 7 Calculate \mathbf{f}^*, σ_*^2 based on (5),(6)
 - 8 **End**
-

In the UQ, most of the initial samples are in the region with a high probability of input parameter distribution, and the entropy of this part of the region is small. In the region with a low probability of input parameter distribution, owing to the lack of sample points, the prediction accuracy is low. Thus, aGPR places most of the adaptive points in the area with a low input parameter probability and continuously reduces the adaptive maximum entropy.

B. UQ framework based on aGPR

Based on the above theory, this study performs EVWPT system transmission efficiency UQ based on the aGPR surrogate model, which is divided into three main stages.

Stage 1: Preparation of training data

Latin hypercube sampling is used to prepare the training data ($\mathbf{x}_{n \times \alpha_0} \boldsymbol{\eta}_{n \times 1}$). In combination with the actual situation, it is assumed that the spatial misalignment uncertainty input parameters obey a uniform distribution, and the coil structure and component uncertainty input parameters obey a normal distribution, given the mean, variance, and fluctuation range of each parameter.

Stage 2: Construction of aGPR surrogate model

A covariance function is selected for aGPR training, and RSA is used to search for the optimal set of hyperparameters. Let the negative log-likelihood function be the unconstrained minimization objective function and the hyperparameters be the optimization variables to prevent the local optimum. The maximum entropy of the transmission efficiency prediction model is continuously updated, and input parameters from the candidate pool are added to the training pool, iterating until a satisfactory maximum entropy is reached. Model evaluation is performed in comparison with the MC method.

Stage 3: WPT transmission efficiency UQ

Two characteristic statistics of the transmission efficiency model, that is, the mean and variance, and the transmission efficiency are calculated. Based on the results, the impact of the input uncertainty on the output can be understood, and the EV-WPT transmission efficiency uncertainty can be quantified.

IV. OPTIMIZATION OF EV-WPT TRANSMISSION EFFICIENCY BASED ON RSA

The RSA is a new intelligent optimization algorithm proposed by Laith Abualigah in 2021. The algorithm mainly simulates the hunting behavior of crocodiles to achieve an optimal solution, which has the characteristics of fast convergence and strong search capability [25].

In this study, the RSA is employed to solve two key problems: first, the optimization problem of the GPR machine learning hyperparameters, and second, the EVWPT system structure optimization problem, in

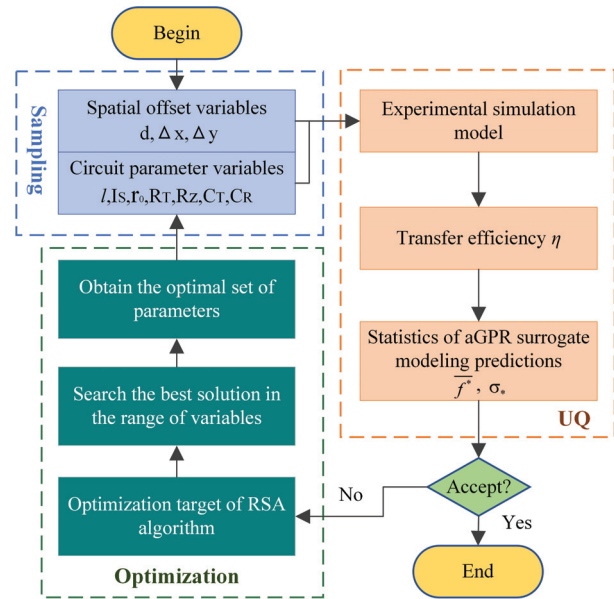


Fig. 4. The overall optimization process for transmission efficiency.

which the WPT system transmission efficiency is taken as the RSA optimization target, and the system structure-related inputs are taken as the optimization parameters to achieve the global optimization of the WPT system transmission efficiency. The overall optimization process is shown in Fig. 4. Firstly, adaptive sampling method is used to extract samples of spatial offset variables and circuit parameters. The aGPR surrogates are then modeled for UQ. The aGPR hyperparameters or model compensation circuit parameters are optimized in the case of unacceptable UQ accuracy and transmission efficiency η . Re-perform the sampling and UQ until the results are acceptable and then end the optimization.

The RSA search process consists mainly of three phases, namely, the initialization phase, encircling phase (exploration), and hunting phase (exploitation).

Initialization phase: The optimization process starts with a set of randomly generated candidate solutions X , as shown in (12):

$$X = rand \times (UB - LB) + LB, \quad (12)$$

where $rand$ denotes to a random number between 0 and 1, and UB and LB denote the upper and lower bounds of the given problem, respectively.

Encircling phase (global search): The RSA exploration mechanism is based on two main search strategies, that is, the high walking movement strategy and belly walking movement strategy. The high walking strategy depends on $t \leq T/4$, the belly walking strategy depends on $t \leq T/2$, and $t > T/4$. The position update equation for the encircling phase is shown in (13):

$$\begin{aligned}
& x_{(i,j)}(t+1) \\
& = \begin{cases} \text{Best}_j(t) - \gamma_{(i,j)}(t) \times \beta - R_{(i,j)}(t) \times \text{rand}, & t \leq T/4 \\ \text{Best}_j(t) \times x_{(i,j)} \times ES(t) \times \text{rand}, & t \leq T/2 \text{ and } t > T/4 \end{cases}, \quad (13)
\end{aligned}$$

where $\text{Best}_j(t)$ is the i_{th} position in the best obtained solution, t is the number of the current iteration, and T is the maximum number of iterations. In addition, $\gamma_{(i,j)}$ denotes the hunting operator for the i_{th} position in the i_{th} solution, which is calculated using (14); β is fixed to equal 0.1; the reduce function $R_{(i,j)}$ is the value used to reduce the search area, which is calculated using (15); r_1 is a random number between $[1 N]$; $x_{(r_1,j)}$ denotes a random position of the i_{th} solution; N is the number of candidate solutions; and $ES(t)$ is the evolutionary sense, which is calculated using (16):

$$\gamma_{(i,j)} = \text{Best}_j(t) \times P_{(i,j)}, \quad (14)$$

$$R_{(i,j)} = \frac{\text{Best}_j(t) - x_{(r_1,j)}}{\text{Best}_j(t) + \varepsilon}, \quad (15)$$

$$ES(t) = 2 \times r_3 \times \left(1 - \frac{1}{T}\right), \quad (16)$$

where ε is a small value, r_2 is a random number between $[1 N]$, r_3 denotes a random integer between $[-1 1]$, and $P_{(i,j)}$ is the percentage difference between the j_{th} position of the best obtained solution and i_{th} position of the current solution.

Hunting phase (local search): The RSA exploitation mechanism makes use of the search space and is based on two main search strategies (hunting coordination and cooperation) to avoid getting trapped in the local optima, as shown in (17). The hunting coordination operation depends on $t \leq 3T/4$ and $t > T/2$, and the hunting cooperation operation depends on $t \leq T$ and $t > 3T/4$:

$$\begin{aligned}
& x_{(i,j)}(t+1) \\
& = \begin{cases} \text{Best}_j(t) \times P_{(i,j)}(t) \times \text{rand}, & t \leq \frac{3T}{4} \text{ and } t > \frac{T}{2}, \\ \text{Best}_j(t) - \gamma_{(i,j)}(t) \times \varepsilon - R_{(i,j)}(t) \times \text{rand}, & \\ t \leq T \text{ and } t > \frac{3T}{4}. \end{cases} \quad (17)
\end{aligned}$$

The algorithm produces a random value in each iteration, and this part of searching is beneficial in the case of local optimum stagnation, especially in the final iteration.

V. EXPERIMENTAL SIMULATION ANALYSIS

A. UQ of transmission efficiency

Based on the transmission efficiency model in Section II, it was determined that the EV-WPT transmission efficiency was highly uncertain owing to the influence of the coupling mechanism misalignment, uncertainty of the coil structure, and circuit component parameters. Based on the actual situation, it was assumed that the spatial location parameters obeyed a uniform

Table 1: Parameter distribution of random variables

Variables	Random Distribution	Unit
l	$N(1, 0.05)$	/
I_S	$N(50, 2.5)$	A
Δx	$U(-0.1, 0.1)$	m
Δy	$U(-0.1, 0.1)$	m
d	$U(0.1, 0.15)$	m
r_0	$N(8e-4, 4e-5)$	m
R_T	$N(0.1, 0.005)$	Ω
R_Z	$N(5, 0.25)$	Ω
C_T	$N(120, 6)$	nF
C_R	$N(130, 7.5)$	nF

distribution, and the component parameters obeyed a normal distribution. After determining reasonable component parameters, the intervals of the most probable distribution of parameters and possible boundaries of the optimized parameters are determined in conjunction with the real situation. The normal distribution sets the variance to $0.05 \times \text{mean}$. The distribution intervals of 10 variables with an impact on transmission efficiency were shown in Table 1.

According to the random distribution parameters in Table 1, 200 training samples were collected with the Latin hypercube sampling method as the initial training pool to establish the aGPR model, and 300 adaptive iterations were performed until the adaptive maximum entropy has leveled off. Another 800 training samples were collected to establish the GPR surrogate model according to the prediction accuracy. At the same time, based on experience and the UQ stability, 10,000MC simulation experiments were performed to verify the accuracy of the aGPR method. The simulation model took about 1 minute to sample each sample, and the calculation time was given for computers with 6core/12-thread processors (Intel Core i5-10400, 2.90 GHz) and 16 GB of RAM, running Windows.

A square kernel was used as the kernel function to optimize the hyperparameters $\theta = [v_0 \sigma_f \sigma_k]$ for the establishment of the aGPR model. To verify the tracking performance of the RSA, it was compared with the simulated annealing algorithm, arithmetic optimization algorithm, and other common algorithms [25]. With (8) as the tracking objective, the population size of each algorithm was set to 20, and the maximum number of iterations was set to 100. The convergence behavior and computation time of each algorithm are shown in Fig. 5. The same global optimal solution was obtained for all the methods, except for the GA, which was trapped in a local optimum, and the RSA had a faster search speed than the other methods, took less time to compute, and demonstrated the strongest overall search capability.

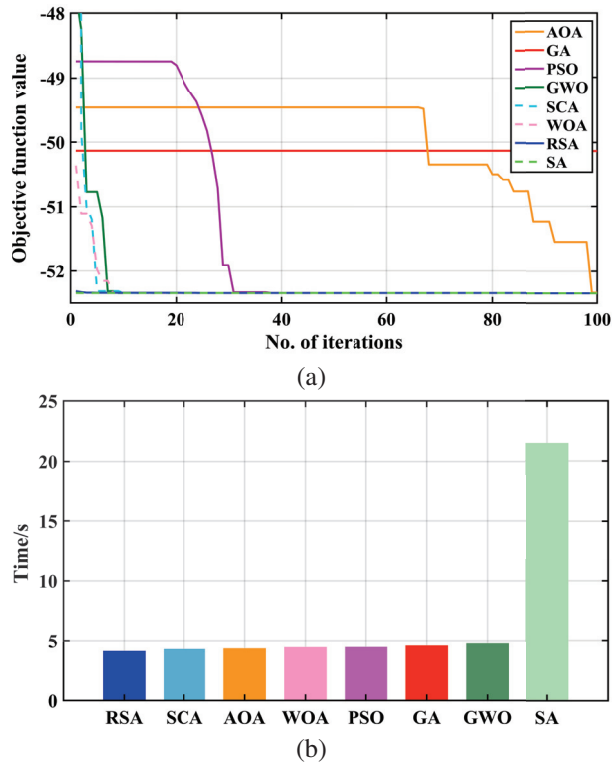


Fig. 5. (a) Convergence results of maximum likelihood estimation and (b) computation time of each algorithm.

To verify whether the aGPR model can overcome the “curse of dimensionality”, UQ was performed on the transmission efficiency of the first five and all 10 dimensions in Table 1, and the training process and prediction results of the five-dimensional variables are shown in Fig. 6. As shown in Fig. 6 (a), the adaptive maximum entropy value decreased continuously during the aGPR training process, and a highly desirable maximum entropy was observed after about 250 calculations. The aGPR prediction results were compared with the true values, as shown in Fig. 6 (b).

The probability of the actual values falling within the prediction interval was 98.75%. Similarly, the GPR prediction results, compared with the true values, are shown in Fig. 6 (c), with a probability of 96.78%, demonstrating that the actual values fell within the prediction interval. To examine the performance of the obtained surrogate model, the aGPR and GPR prediction results were compared, as shown in Fig. 6 (d) and Table 2, demonstrating that the aGPR model had a higher prediction accuracy in the areas with a low probability of occurrence of the samples and stronger predictive capability than the GPR model.

According to the above experiments and EV-WPT model proposed in Section II, this study quantified the uncertainty of the EV-WPT system transmission effi-

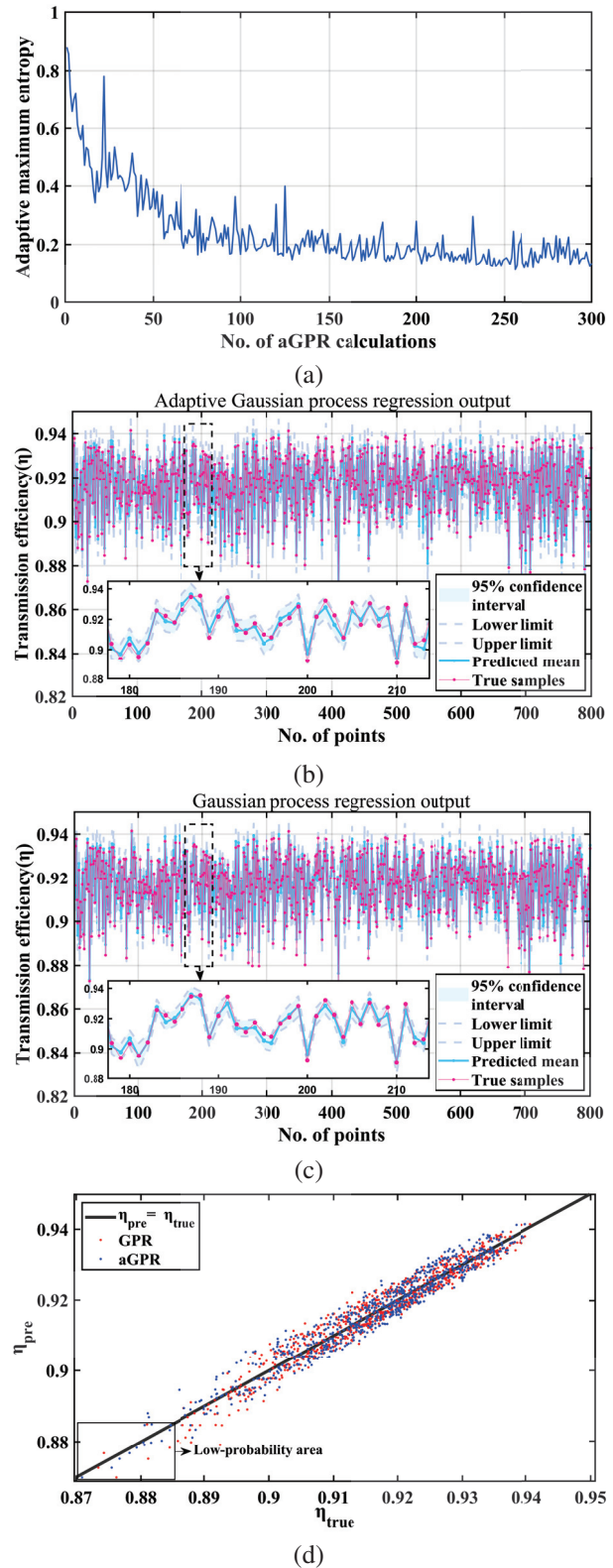


Fig. 6. GPR and aGPR training process and results: (a) Adaptive maximum entropy value iteration, (b) AGPR training and prediction, (c) GPR training and prediction, and (d) Comparison of predicted mean and true values.

Table 2: Statistical parameters related to prediction

	Probability of Actual Values Within the Predicted Intervals	MAPE	RMSE	Coefficient of Determination
GPR	96.78%	0.27%	0.0030	0.97355
aGPR	98.75%	0.27%	0.0029	0.97406

ciency based on the aGPR, GPR, and MC models and obtained the comparison results of the three methods through simulation, as shown in Fig. 7 and Table 3. Based on the above simulation results, it was determined that the UQ accuracy of the proposed aGPR model was basically the same as that of the MC method. Compared with the GPR model, the overall speed of the aGPR model increased by about 9.2% and 14.3%, which substantially reduced the computational cost. The computational cost remained the same when the dimensionality of the input variables increased, indicating that the

aGPR model was not trapped in the “curse of dimensionality”, but the mean value of the transmission efficiency decreased, and the variance increased, showing the existence of many uncertainties in the actual engineering, which can reduce the transmission efficiency and robustness of the WPT system. Therefore, there is an urgent need to optimize EV-WPT systems.

B. Optimization

In combination with the contents of Section IV, component parameters R_T, R_Z, C_T , and C_R in the primary and secondary circuits were optimized, with WPT system efficiency as the optimization objective. With the mean values of the parameters in Table 1 as the basis, optimization was performed within the range of $[R_T/2, 2 \times R_T], [R_Z/2, 2 \times R_Z], [C_T/2, 2 \times C_T]$, and $[C_R/2, 2 \times C_R]$, considering the global search and calculation cost.

To verify the superiority of the RSA, it was compared with the Sparrow Search Algorithm (SSA), improved Grey Wolf Optimizer (IGWO), and Enhanced Whale Optimization Algorithm (EWOA) at the same time.

According to the experimental effect, the population size of all four algorithms was 20, and the maximum

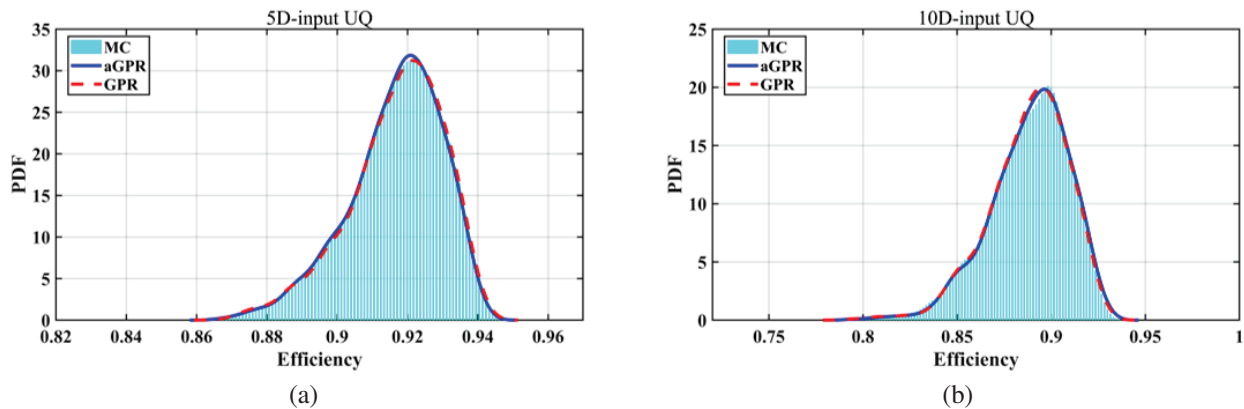


Fig. 7. Contrast of probability density function (PDF) (a) under the first five dimensions and (b) under the whole dimensions of input variables in Table 1.

Table 3: Comparison of MC, GPR, and AGPR models with uncertainty inputs

Dimensions of Variables	Method	Mean	Variance	Correlated Error		Total Time	
				Mean	Variance	Sampling	Calculation
5	MC	0.9044	0.02712	Mean	Variance	6 d22 h	
	GPR	0.9053	0.02662	0.0995%	-1.844%	13 h27 min	53 s
		aGPR	0.9045	0.02678	0.011%	-1.254%	12 h19 min
10	MC	0.8628	0.04578	Mean	Variance	7 d8 h	
	GPR	0.862	0.04822	-0.093%	5.33%	13 h49 min	57 s
		aGPR	0.8629	0.04829	0.012%	5.46%	12 h05 min

number of iterations was 10. The efficiency optimization iterative process and optimization results of each method are shown in Table 4 and Fig. 8. The SSA and EWOA easily fell into local optimization, resulting in low search accuracy. Although the IGWO demonstrated high search accuracy, its calculation speed was slow such that the optimal transmission efficiency of 94.23% was approached in the 8th iteration. Compared with the other algorithms, the RSA had a faster calculation speed and higher search accuracy, which quickly approached the optimal transmission efficiency in the third iteration, and effectively solved the problem of WPT efficiency optimization.

Taking the optimal solution obtained by the RSA as the mean of the input parameters, the probability density function of the transmission efficiency, corresponding to the 10-dimensional uncertainty inputs in Table 1, was calculated by the aGPR model. The mean value of the optimized aGPR prediction was 0.9343, and the variance was 0.02218. The mean value of the transmission efficiency improved by 8.27%, and the variance decreased by 54.07%, which significantly improved the transmission efficiency and robustness of the EV-WPT system, thereby providing a theoretical basis for the practical engineering design and optimization of EVWPT systems. The probability density functions of the efficiency, quantified by the aGPR and

Table 4: Parameter comparison before and after optimization

	$R_T(\Omega)$	$R_Z(\Omega)$	$C_T(\text{nE})$	$C_R(\text{nF})$	$\eta \times 10^0$ (%)
Original	0.1	5	120	130	90.52
RSA	0.1582	9.9962	224.4007	191.5533	94.23
IGWO	0.1525	9.9986	235.4230	194.9361	94.23
EWOA	0.1542	8.2954	119.1866	140.7130	93.15
SSA	0.2	10	240	65	84.50

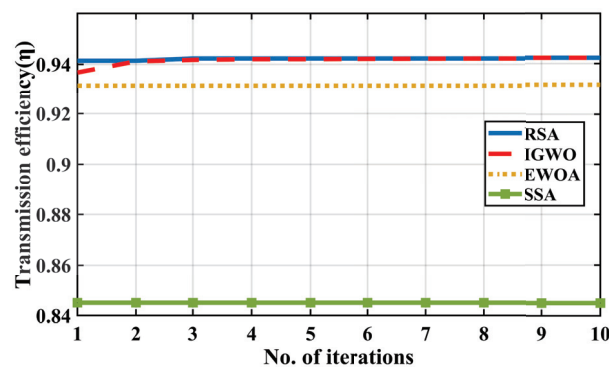


Fig. 8. Comparison of different algorithms for efficiency optimization results of WPT system.

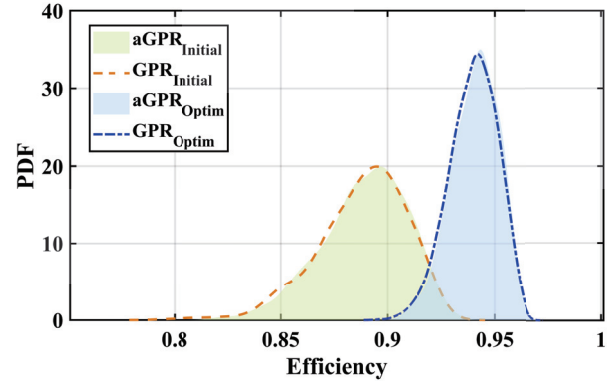


Fig. 9. Comparison of PDFs for efficiency of WPT system before and after optimization.

GPR models before and after optimization, are compared in Fig. 9.

The above simulations and comparative experiments showed that when uncertainties were present in the transmission process, the optimized WPT system proposed in this study demonstrated high transmission efficiency and strong robustness, which can effectively meet practical engineering needs.

VI. CONCLUSION

Based on the influence of transceiver coil mutual inductance on the transmission efficiency, this study focuses on the uncertainty effect of input variables on the efficiency of an EV-WPT system under actual conditions. In this study, aGPR is proposed as the UQ framework for EV-WPT transmission efficiency. Through a comparison of the quantitative results of the MC, GPR, and aGPR models, it is determined that the aGPR model has approximately the same solution accuracy as the MC method, and its computational speed is about 9.2% better than that of the GPR model, which can significantly reduce the computational cost and verify the absence of the “curse of dimensionality”. The RSA is used to optimize the transmission efficiency, and the results show that the mean value of the optimized transmission efficiency increases by 8.27%, whereas the variance decreases by 54.07%. In summary, the results reveal that the scheme proposed in this study can provide a low-cost and reliable solution for the transmission efficiency UQ and optimization of EV-WPT systems.

ACKNOWLEDGMENT

This work was supported in part by the Jilin Scientific and Technological Development Program under Grant 20230201122GX, Grant 20220101196JC, and Key Laboratory for Comprehensive Energy Saving of Cold Regions Architecture of Ministry of Education, Jilin Jianzhu University under Grant JLJZHDKF202203.

REFERENCES

- [1] A. Triviño, J. M. González-González, and J. A. Aguado, "Wireless power transfer technologies applied to electric vehicles: A review," *Energies*, vol. 14, no. 6, p. 1547, Mar. 2021.
- [2] A. Ahmad, M. S. Alam, and R. Chabaan, "A comprehensive review of wireless charging technologies for electric vehicles," *IEEE Trans. Transp. Electrification*, vol. 4, no. 1, pp. 38-63, Mar. 2018.
- [3] S. Y. Choi, B. W. Gu, S. Y. Jeong, and C. T. Rim, "Advances in wireless power transfer systems for roadway-powered electric vehicles," *IEEE J. Emerg. Sel. Topics Power Electron.*, vol. 3, no. 1, pp. 18-36, Mar. 2015.
- [4] D. Patil, M. K. McDonough, J. M. Miller, B. Fahimi, and P. T. Balsara, "Wireless power transfer for vehicular applications: Overview and challenges," *IEEE Trans. Transp. Electrification*, vol. 4, no. 1, pp. 3-37, Mar. 2018.
- [5] K. Detka and K. Górecki, "Wireless Power Transfer-A Review," *Energies*, vol. 15, no. 19, p. 7236, Jan. 2022.
- [6] M. G. Eftekhari, Z. Ouyang, M. A. E. Andersen, P. B. Andersen, L. A. de S. Ribeiro, and E. Scholtz, "Efficiency study of vertical distance variations in wireless power transfer for e-mobility," *IEEE Trans. Magn.*, vol. 52, no. 7, pp. 1-4, July 2016.
- [7] H. Kim, C. Song, H. Kim, D. H. Jung, I.-M. Kim, Y.-I. Kim, J. Kim, S. Ahn, and J. Kim, "Coil design and measurements of automotive magnetic resonant wireless charging system for high efficiency and low magnetic field leakage," *IEEE Trans. Microw. Theory Techn.*, vol. 64, no. 2, pp. 383-400, Feb. 2016.
- [8] R. Narayanamoorthi, "Modeling of capacitive resonant wireless power and data transfer to deep biomedical implants," *IEEE Trans. Compon. Packag. Manuf. Technol.*, vol. 9, no. 7, pp. 12531762Tule20710.
- [9] G. Fishman, *Monte Carlo: Concepts Algorithms and Applications*, Berlin: Springer, 2013.
- [10] M. Rossi, G.-J. Stockman, H. Rogier, and D. Yande Ginste, "Stochastic analysis of the efficiency of a wireless power transfer system subject to antenna variability and position uncertainties," *Sensors*, vol. 16, no. 7, pp. 1100, July 2016.
- [11] Q. Yu, W. Liu, K. Yang, X. Ma, and T. Wang, "Uncertainty quantification of the crosstalk in multiconductor transmission lines via degree adaptive stochastic response surface method," *Applied Computational Electromagnetics Society (ACES) Journal*, vol. 36, no. 2, pp. 174-183, Mar. 2021.
- [12] R. Trincherro, M. Larbi, H. M. Torun, F. G. Canavero, and M. Swaminathan, "Machine learning and uncertainty quantification for surrogate models of integrated devices with a large number of parameters," *IEEE Access*, vol. 7, pp. 4056-4066, 2019.
- [13] M. Larbi, R. Trincherro, F. G. Canavero, P. Besnier, and M. Swaminathan, "Analysis of parameter variability in an integrated wireless power transfer system via partial least-squares regression," *IEEE Trans. Compon. Packag. Manuf. Technol.*, vol. 10, no. 11, pp. 1795-1802, Nov. 2020.
- [14] Y. Pei, L. Pichon, M. Bensetti, and Y. Le-Bihan, "Uncertainty quantification in the design of wireless power transfer systems," *Open Phys.*, vol. 18, no. 1, pp. 391-396, July 2020.
- [15] T. Wang, Y. Wu, B. Li, Q. Yu, L. Xu, and S. Guan, "Design of electric vehicle's wireless power transfer system based on deep learning combined with multi-objective optimization," *IEEE Trans. Compon. Packag. Manuf. Technol.*, vol. 12, no. 12, pp. 1983-1994, Nov. 2022.
- [16] P. Manfredi and R. Trincherro, "A probabilistic machine learning approach for the uncertainty quantification of electronic circuits based on Gaussian process regression," *IEEE Trans. Comput.-Aided Design Integr. Circuits Syst.*, vol. 41, no. 8, pp. 2638-2651, Aug. 2022.
- [17] L. Chen, S. Liu, Y. C. Zhou, and T. J. Cui, "An optimizable circuit structure for high-efficiency wireless power transfer," *IEEE Trans. Ind. Electron.*, vol. 60, no. 1, pp. 339-349, July 2013.
- [18] L. Yang, M. Zong, and C. Li, "Voltage-gain design and efficiency optimization of series/series-parallel inductive power transfer system considering misalignment issue," *Energies*, vol. 14, no. 11, p. 2999, Jan. 2021.
- [19] Z. Zhou, Z. Liu, and H. Su, "Multi-objective optimization of the wireless power transfer system for electric vehicles," in *Proc. IEEE Wireless Power Transf. Conf. (WPTC)*, pp. 215-218, Nov. 2000.
- [20] S. Jeong, J. Jung, K. A. Kim, and J. Kim, "Analytical investigation of optimal wireless power transfer topology for electric vehicles," in *Proc. IEEE PELS Workshop Emerg. Technol. Wireless Power (WoW)*, pp. 1-5, June 2015.
- [21] Y. Guo, L. Wang, and C. Liao, "A general equivalent model for multi-coil wireless power transfer system analysis and its application on compensation network design," *Applied Computational Electromagnetics Society (ACES) Journal*, vol. 33, no. 06, pp. 648-656, July 2021.

- [22] C. E. Rasmussen and C. K. I. Williams, *Gaussian Processes for Machine Learning*, Cambridge, MA: MIT Press, 2006.
- [23] T. Zhang, Y. Tian, X. Chen, and J. Gao, "Antenna resonant frequency modeling based on AdaBoost gaussian process ensemble," *Applied Computational Electromagnetics Society (ACES) Journal*, vol. 35, no. 12, pp. 1485-1492, Dec. 2020.
- [24] C. Rong, X. He, Y. Wu, Y. Qi, R. Wang, Y. Sun, and M. Liu, "Optimization design of resonance coils with high misalignment tolerance for drone wireless charging based on genetic algorithm," *IEEE Trans. Ind. Appl.*, vol. 58, no. 1, pp. 12421253, Jan. 2022.
- [25] L. Abualigaha, M. A. Elaziz, P. Sumari, Z. WooGeem, and A. H. Gandomi, "Reptile Search Algorithm (RSA): A nature-inspired metaheuristic optimizer," *Expert Syst. Appl.*, vol. 1, Apr. 2022.
- [26] J. Zhou and J. Li, "IE-AK: A novel adaptive sampling strategy based on information entropy for Kriging in metamodel-based reliability analysis," *Reliab. Eng. Syst. Saf.*, vol. 229, p. 108824, Jan. 2023.



Xinlei Shang received the B.S. degree, the M.S. degree and the Ph.D. degree in Test and Measurement Technology and Instrumentation from Jilin University, Changchun, Jilin, China, in 2004, 2007 and 2010, respectively.

He is currently a professor with the College of Instrumentation and Electrical Engineering, Jilin University. His research interest includes nuclear magnetic resonance and transient electromagnetism.



Linlin Xu received the B.S. degree in electrical engineering and automation from the College of Instrumentation and Electrical Engineering, Jilin University, Changchun, Jilin, China, in 2020, where she is currently pursuing the M.S. degree in electrical engineering.

ing.

Her research interests include electromagnetic safety and electromagnetic compatibility of wireless charging systems in electric vehicles.



Quanyi Yu received the B.S. degree from the College of Communication Engineering, Jilin University, Changchun, Jilin, China, in 2016, the M.S. degree from College of Instrumentation and Electrical Engineering, Jilin University, Jilin, China, in 2020, where he is currently pursuing the Ph.D. degree in measurement technology and instruments.

His research interests include the uncertainty quantification and electromagnetic compatibility of wireless power transfer of EVs.



Bo Li received a B.S. degree in electrical engineering and automation from College of Instrumentation and Electrical Engineering, Jilin University, Changchun, Jilin, China, in 2020. He is currently studying for a M.S. degree in electrical Engineering from the College of Instrumentation and Electrical Engineering, Jilin University.

His research interests include uncertainty analysis, wireless power transfer, magnetic resonance, and human protection.



Gang Lv received the master degree of electronic circuit and system in college of electronic science & engineering, Jilin University, Changchun, Jilin, China, in 2008. He came on board into National Automotive Quality supervision & Inspection Center (Changchun) after graduated. He is currently the head of the EMC department. He is mainly in charge of the EMC performance in vehicle type approval under the direction of Ministry of Industry and Information Technology (MIIT) and Certification and Accreditation Administration of the P.R.C.

He always focuses on test methods improving and National Standards edit and amendment in EMC domain. He has joined teams to be responsible for EMC part of "Test and Evaluation of autonomous electric vehicle" subject which is released by Ministry of Science and Technology (MOST) and "Research on real-time concurrent Simulation test technology of Multi-source Sensor information of Intelligent Networked Vehicle" which is released by Science and Technology Department of Jilin Province.



Yaodan Chi received the B.S. degree in electronic information engineering from the Jilin University of Technology, Changchun, Jilin, China, in 1998, and the master's degree in testing and measuring technology and instruments and the Ph.D. degree in science and technology of instrument from Jilin University, Changchun, Jilin, China, in 2004 and 2018, respectively. She is currently the Vice Director of the Jilin Provincial Key Laboratory of Architectural Electricity and Comprehensive Energy Saving.

Her research interests include the uncertainty analysis approaches in electromagnetic compatibility simulation and building equipment intelligent integration technology.



Tianhao Wang received the B.S. degree in electrical engineering and the Ph.D. degree in vehicle engineering from Jilin University, Changchun, Jilin, China, in 2010 and 2016, respectively.

From 2016 to 2019, he was a Postdoctoral Researcher with the Department of Science and Technology of Instrument, Changchun, Jilin University. He is currently an associate professor with the College of Instrumentation and Electrical Engineering, Jilin University. His research interest includes the uncertainty quantification of wireless power transfer of EVs and human electromagnetic exposure safety.

Mitigation of Feed Horn Overlapping Condition for Multi-beam Parabolic Reflector Antenna

Nur Faiqah Fauzi¹, Nurul Huda Abd Rahman¹, Yoshihide Yamada²,
Robi'atun Adayiah Awang¹, and Idnin Pasya³

¹Antenna Research Centre College of Engineering
Universiti Teknologi MARA 40450 Shah Alam, Selangor, Malaysia
nurulhuda0340@uitm.edu.my, nfaiqahfauzi@gmail.com, robiatun@uitm.edu.my

²Malaysia-Japan International Institute of Technology (MJIIT) Universiti Teknolgi Malaysia
Jalan Yahya Petra 54100 Kuala Lumpur, Malaysia
yoshihide@utm.my

³Department of Computer Science and Engineering
Division of Computer Engineering, University of Aizu Aizuwakamatsu 965-8580, Japan
idnin@u-aizu.ac.jp

Abstract – In designing a contoured beam for communication satellite services, a reflector antenna remains the most preferred option. Previously, a multi-beam technique employing many feed horns at optimal feed positions was proposed to obtain a precise contour beam for Malaysia. However, it has led to feed horn overlapping when the beams were arranged closely. Therefore, this issue of beam allocation and feed horn size shall be addressed. In this article, an analysis of the relationship between feed position and beam direction is analysed through the Beam Deviation Factor (BDF). As a result, a useful design chart was derived for no feed horn overlapping conditions, which determines beam separation and feed horn size at different values of F/D. A practical application showing the Peninsular Malaysia beam coverage was demonstrated to validate the derived correlation. As a result, five multi-beams have been successfully designed with no overlapping feed horns. Through simulation, an excellent contour beam for Peninsular Malaysia was justified, featuring low side lobes, narrow beam width and high gain.

Index Terms – Beam shaping, Feed horn overlapping, Multi-beam, Parabolic reflector antenna, Satellite antenna.

I. INTRODUCTION

In Malaysia, the MEASAT Satellite System is currently the provider of satellite communication services through the MEASAT-3 satellite. These services include C-band and Ku-band services for the direct-to-home (DTH), video distribution and other Fixed Satel-

lite Service (FSS). The Ku-band beams offer high-quality DTH coverage across South Asia, Indonesia and Malaysia. Geographically, the Malaysia region consists of two main parts, Peninsular Malaysia and the Borneo region. Figure 1 demonstrates the Malaysia region from MEASAT-3's satellite point-of-view located at the orbital slot of 91.5° East longitude [1]. By observing the satellite's footprint for Malaysia, the beam shape can be further improved by concentrating on high-density areas and thus, will result in a more accurate contoured beam for Malaysia.

Contoured beam antennas have been widely used for various applications such as broadcasting, military operations and high-speed internet access. These applications require a highly concentrated and consistent signal to ensure uninterrupted data transmission to the coverage areas. While a single narrow beam can be used for the operation, it has limited coverage on the earth surface. Therefore, two techniques can be employed to produce

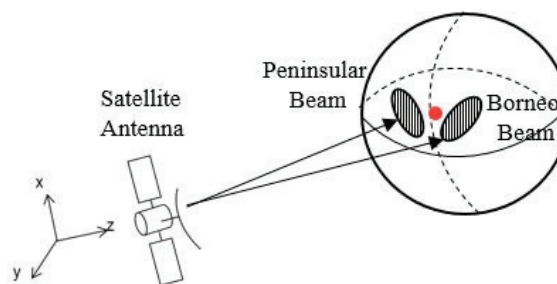


Fig. 1. Illustration of Malaysia from satellite point-of-view.

contoured beams, such as reflector shaping or a combination of multiple beams. Reflector shaping may be accomplished by creating the proper reflector curvature [2–4]. Among the available techniques, the multi-beam antenna (MBA) has been used to combine multiple narrow beams into the desired beam shape using a reflector antenna and multiple feed system [5–8]. In MBA, an array of feeds can be arranged simultaneously based on a precise positioning technique to generate a contoured beam of the desired area. By adopting this multi-beam concept, a precise contoured beam of Malaysia coverage can be accurately designed.

In the previous works on achieving Malaysia coverage by multi beams, feed horn overlapping problem has occurred. One technique used to address this issue was to replace the horn with a patch antenna [9–12]. However, in that work, the proposed mitigation technique was through the implementation of planar arrays, but a detailed analysis of how to solve the original overlapping horn issues was not provided. Another investigation of radiation properties has already been conducted [13], however, the theoretical and simulation results only focused on gain and side-lobe levels without providing information on how to overcome the feed overlapping.

When designing multi beams with multiple feeds, feed positioning becomes very important. In [14] the best feed position was obtained using ray tracing method. The feed positions were determined based on the concentrated point of all rays, based on caustic dependency on focal-length-to-diameter-ratio (F/D). However, to clarify the adequateness of the feed position in relation of F/D and beam direction, the method of focal region ray tracing is considered to be more reliable.

In this article, the feed overlapping issues are demonstrated and solved through the optimization of antenna parameters via theoretical analysis and the derivation of a design graph. The analysis is conducted in three steps. First, the correlation between feed displacement and beam separation is derived using technical parameters of the antenna such as reflector diameter, D , horn size, H , and wavelength, λ . Through the derived expression, the beam separation is presented in terms of the antenna beam width, meanwhile, the feed displacement is denoted in terms of feed horn size. As a result, a design graph showing the size of the feed horn that can be implemented to mitigate overlapping horn issues is determined. Next, to ensure the adequateness of the design graph, a practical example of the Malaysia coverage employing five multi-beam antennas is demonstrated.

II. ANALYSIS OF HORN OVERLAPPING

A. Fundamental equation of parabola

Figure 2 shows the configuration of the parabolic reflector antenna system used in this analysis. The reflec-

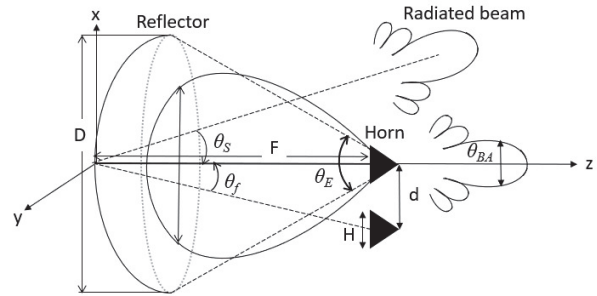


Fig. 2. Antenna parameters.

tor edge angle, θ_E , is determined as shown in the figure, while the half power beam width of a horn radiation pattern is indicated as θ_{BH} and the half power beam width of a reflector radiation pattern is indicated as θ_{BA} . The radiated beam direction, θ_S , is determined by the feed horn shift angle, θ_f . The detailed parameters used in this study are shown in Table 1.

Table 1: Parabolic reflector parameters

	Parameters	Symbols
	Frequency	f
	Wavelength	λ
Parabola	Reflector diameter	D
	Focal length	F
	Reflector edge angle	θ_E
	Half-power beam width of a reflector	θ_{BA}
	Beam separation angle	θ_S
Feed	Feed horn size	H
	Half-power beam width of a horn	θ_{BH}
	Feed horn displacement	d
	Feed horn displacement angle	θ_f

The relationship between the fundamental structural parameters of a parabolic reflector, namely the reflector edge angle, θ_E , focal length, F , and diameter, D , is expressed by equation (1):

$$\tan \frac{\theta_E}{4} = \frac{1}{4 \left(\frac{F}{D} \right)}. \quad (1)$$

By applying the approximation of $\tan(\theta_E/4) \approx \theta_E/4$ (*rad*), equation (1) is simplified as equation (2):

$$\theta_E = \frac{D}{F}. \quad (\text{rad}). \quad (2)$$

The beam width of the radiated beam, θ_{BA} , is given by equation (3):

$$\theta_{BA} = 1.14 \frac{\lambda}{D}. \quad (\text{rad}). \quad (3)$$

Here, the coefficient of 1.14 is determined based on the tapered aperture distribution of -10dB edge level [14].

B. Feed horn equations

The feed horn's size and its relation to the reflector edge level is important. Equation (4) describes the half power beam width of the conical feed horn, θ_{BH} , which is inversely proportional to its aperture size, H :

$$\theta_{BH} = 1.2 \frac{\lambda}{H}. \quad (\text{rad}). \quad (4)$$

The accuracy of the coefficient 1.2 used in equation (4) will be discussed in detail in section III part B.

Figure 3 illustrates the relationship between θ_{BH} and θ_E . Generally, the beam width, θ_{BH} , is almost same as the angle to the first null point, θ_N , as shown in the figure. In order to show the relation of θ_{BH} and θ_E , an α value is introduced, as shown by equation (5):

$$\frac{\theta_E}{2\theta_{BH}} = \alpha. \quad (5)$$

When $\alpha=1$, $\theta_E=2\theta_{BH}$ indicates that the null point corresponds to the reflector edge. At $\alpha=0.5$, $\theta_E=\theta_{BH}$ meaning that the reflector edge is illuminated by the feed horn at a level of -3dB (edge level). In the practical reflector design, the reflector edge level of around -10dB is selected. Then, an α value of around 0.7 is suitable.

By applying equations (2) and (4) to equation (5), the approximate relation between the size of the horn, H/λ and F/D is derived as shown in equation (6):

$$\frac{H}{\lambda} = 2.4\alpha \frac{F}{D}. \quad (6)$$

The importance of equation (6) is that the horn size, H , is related to F/D with a parameter α .

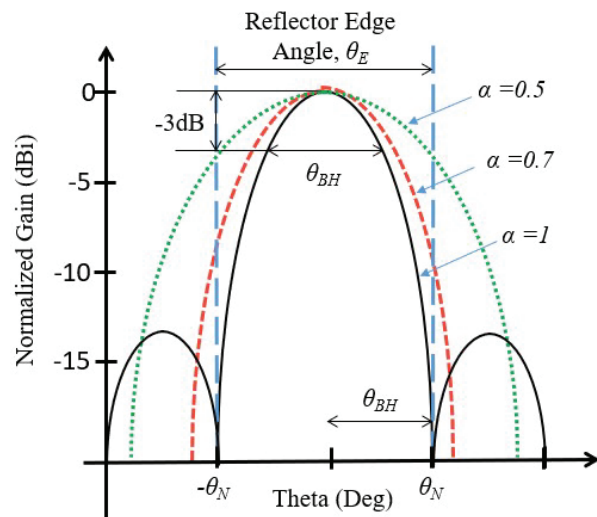


Fig. 3. Comparison of the reflector edge level with different values of α .

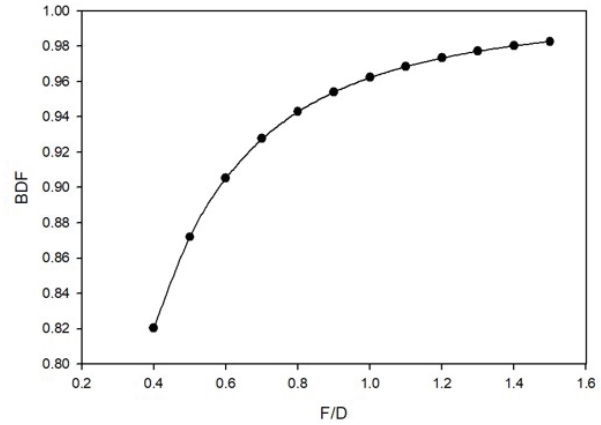


Fig. 4. BDF value versus F/D .

C. Beam direction and feed position

Figure 2 illustrates how the feed position, beam direction and feed displacement are related. The feed shift angle, θ_f , can be approximated in terms of the feed displacement, d , by the equation:

$$\tan\theta_f \approx \theta_f = \frac{d}{F}. \quad (7)$$

As for the relation of the feed displacement, d , to the radiation beam shift, θ_s , a beam deviation factor (BDF) equation can be used [15]:

$$\frac{\theta_s}{\theta_f} = BDF = \frac{1 + 0.36\left(\frac{D}{4F}\right)^2}{1 + \left(\frac{D}{4F}\right)^2}. \quad (8)$$

The numerical data of BDF is shown in Fig. 4, which shows that the BDF value increases with an increase in F/D . However, the change in BDF value is relatively small between 0.8 to 1.0.

By applying equation (7) to equation (8), θ_s is expressed by feed displacement, d , as in equation (9):

$$\theta_s = \theta_f BDF = \frac{d}{F} BDF. \quad (9)$$

D. Beam separation

In designing beam allocations, the beam separation angle, θ_s , is determined by the beam width of the parabolic reflector, θ_{BA} , by using the equation:

$$\theta_s = \beta\theta_{BA}. \quad (10)$$

Here, β is a parameter that determines the beam separation.

Figure 5 provides an example that illustrates the influence of β values. When $\beta=1$, the beam separation is similar to the beam width, θ_{BA} , resulting in beam overlapping as shown in Fig. 5 (a). For $\beta>1$, the beam separation becomes larger than the beam width, resulting in no beam overlapping, as shown in Fig. 5 (b).

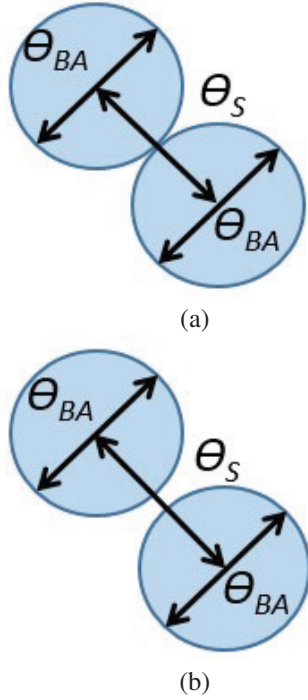


Fig. 5. (a) The relation between θ_{BA} and θ_S when $\beta=1$ and (b) The relation between θ_{BA} and θ_S when $\beta>1$.

E. No feed overlapping condition

Firstly, by applying equation (3) to equation (10), θ_s is expressed by the equation of $1.14\lambda/D$. Then, by using the θ_s equation of equation (9), the following equation is obtained:

$$1.14\beta \frac{\lambda}{D} = \frac{d}{F} BDF. \quad (11)$$

Using equations (6) and (11), F/D can be expressed as equation (12):

$$\frac{F}{D} = \frac{1}{2.4\alpha} x \frac{H}{\lambda} = \frac{BDF}{1.14\beta} x \frac{d}{\lambda}. \quad (12)$$

The following equation is derived to explain the relation between α , d , β and H .

$$\frac{\alpha}{\beta} x \frac{d}{H} = \frac{1}{BDF} x \frac{1.14}{2.4} = \frac{0.475}{BDF}. \quad (13)$$

The value of d/H is a key factor in judging feed overlapping. A value of $d/H>1$ indicates that there is no overlapping, while a value of and when $d/H<1$ indicates overlapping. The critical condition is when $d/H=1$.

To determine the relation between α and β , it is useful to consider the condition of $d/H=1$. The result is shown in Fig. 6 for various antenna F/D . On the line $\alpha=0.62$, the corresponding β value yields $d/H=1$. If β is slightly larger, it results in $d/H>1$ and, thus, no overlapping occurs. If β is slightly smaller, d/H is less than 1 ($d/H<1$) and overlapping occurs. In the practical antenna design presented in section III, $F/D=1$ is used. For this value, $\alpha=0.62$ and $\beta=1.3$ are selected.

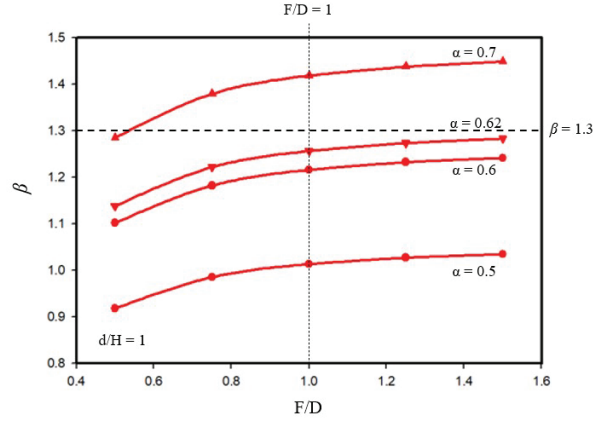


Fig. 6. Relation of F/D and β at $d/H=1$.

III. APPLICATION TO PRACTICAL REFLECTOR ANTENNA DESIGN

To ensure the accuracy of the feed position designing method discussed in section II, a practical antenna structure was designed for achieving a fine contour beam for Peninsular Malaysia coverage. To accomplish this, a multi-beam technique was employed, as shown in Fig. 7. In this figure, the boresight of the satellite antenna is aligned nearby to Riau Island (0,0) based on the geostationary satellite location at (3,1). Five beams denoted as B1, B2, B3, B4 and B5 are arranged to form a precise beam coverage for the Peninsular Malaysia region.

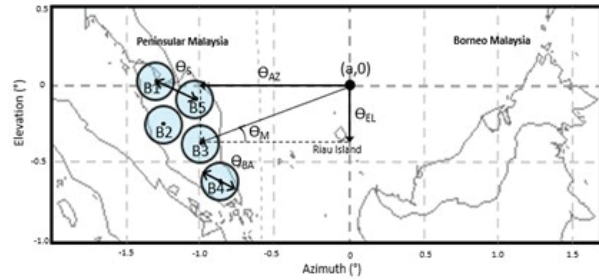


Fig. 7. Beam coverage of Peninsular Malaysia area.

A. Reflector antenna parameters

Table 2 shows the antenna parameters used to design the contoured beam for Peninsular Malaysia, which is divided into five small beams. The chosen operating frequency 7.5 GHz falls within the FSS planned band allocated for Malaysia. The antenna diameter, D , is set to 8.5 m to achieve narrow beam width, θ_{BA} , of 0.3° based on equation (2). The focal length is set to 8.5 m, which results in an F/D ratio of 1. Using equation (1), the calculated value for reflector edge angle, θ_E , is 56° . With $\beta=1.3$, the beam separation angle, θ_S , is determined to

Table 2: Detailed parameters of antenna design

Item	Value
Frequency, f	7.5 GHz
Reflector diameter, D	8.5 m
Focal length, F	8.5 m
Reflector edge angle, θ_E	56°
Beam width of a reflector, θ_{BA}	0.3°
B	1.3
Beam separation angle, θ_S	0.39°
Feed horn displacement, d	0.064 m

be 0.39° through calculation using equation (9). The feed displacement, d , is calculated to be 0.064 m from equation (8).

B. Feed horn

As for the feed horn, a conical horn antenna is selected due to the ability to mitigate the overlapping horn issues compared to the rectangular horn. The feed horn parameters are shown in Table 3. By applying $\alpha=0.62$ to equation (5), θ_{BH} of 45.2° is obtained from $\theta_E=56^\circ$. Then, the horn diameter, H , is calculated using equation (4). Other parameters such as horn length and waveguide dimensions are shown in Fig. 8, which are determined based on [16].

Electromagnetic simulations are performed by using FEKO electromagnetics solver to validate the feed horn performance. The three-dimensional (3D) and one-dimensional (1D) radiation patterns are shown in Figs. 9 (a) and (b), respectively. The reflector edge level beam becomes -7.3 dB and -8.5 dB for E-plane and H-plane, respectively. In Fig. 3, -10dB edge level is achieved at $\alpha=0.7$. Then, at $\alpha=0.62$, the edge level is slightly increased. From Fig. 9 (b), the half power beam-width, θ_{BH} , of the E-plane becomes $\theta_{BH}=46^\circ$ (0.8 rad). From Table 3, λ/H becomes 0.67 m. Then, θ_{BH} and λ/H relation is given by the following equation:

$$\theta_{BH} = 1.198 \frac{\lambda}{H}. \tag{14}$$

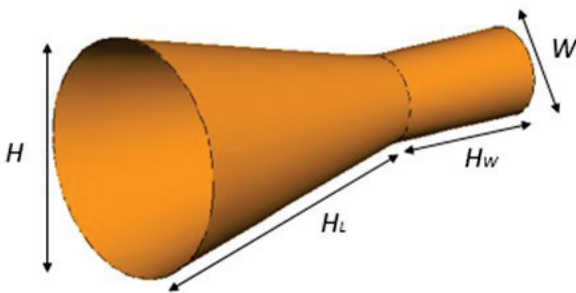
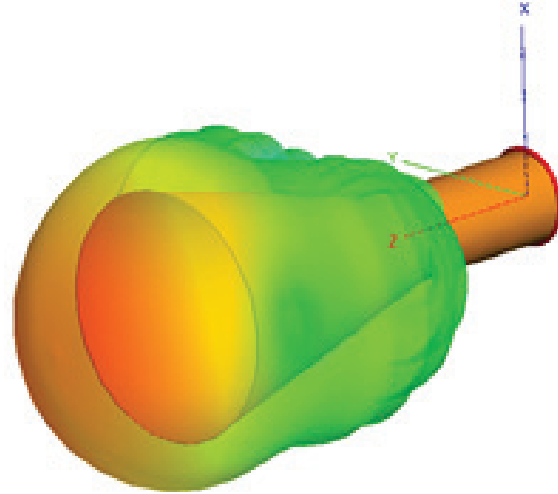
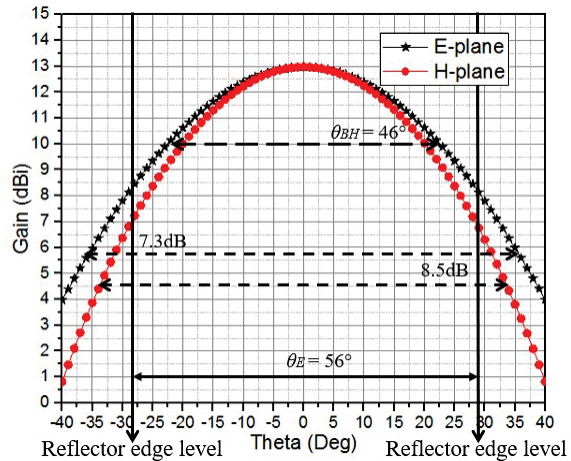


Fig. 8. Conical feed horn structure.



(a)



(b)

Fig. 9. (a) 3D radiation pattern of a single 7.5 GHz horn antenna and (b) E-plane and H-plane radiation pattern of a single horn.

By comparing equation (14) and equation (4), adequacy of 1.2 is ensured.

C. Horn mutual coupling

Two horns are closely arranged to calculate the mutual coupling of the feed horn arrangement, as shown in Fig. 10. In general, the mutual coupling of two horn excitations is the superposition of one horn excitation. The mutual coupling can be evaluated by the situation in which one horn of the two is excited. In Figs. 11 (a) and (b), electric field distribution and field intensity are shown, respectively. Field strength is decreased by more than 20 dB at the parasitic horn compared to the excited horn. Based on this observation, the effect of mutual coupling can be judged to be very small. The radiation pattern of a single horn compared to the dual

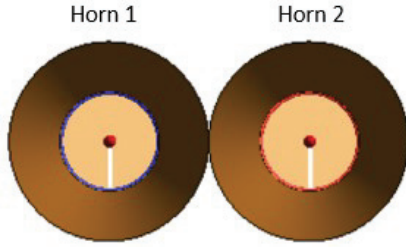


Fig. 10. Dual horn configuration.

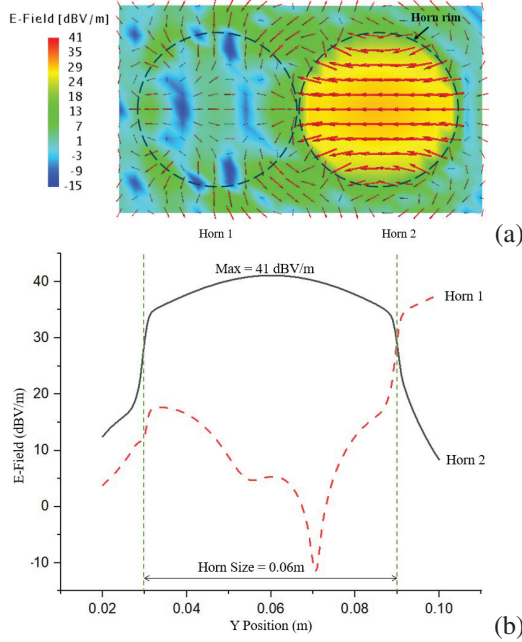


Fig. 11. (a) Electric field distribution and (b) Field intensity.

horn configuration shown in Fig. 10 is plotted. Based on Fig. 12, no efficiency degradation between these two horn types is observed.

D. Horn allocation for multi-beam

The coordinate system for positioning the feed horn is shown in Fig. 13, where θ_M represents the angle from the centre to the desired beam position shown in Fig. 7. θ_M has two position components, known as θ_{AZ} and θ_{EL} , that correspond to the feed horn displacement (Δd). Δd has three positional components: Δx , Δy and Δz .

Using equations (7) and (8), the feed displacement, Δd , can be expressed as:

$$\Delta d(\Delta x, \Delta y) = -\frac{F}{BDF} \sin \theta_M. \quad (15)$$

Here, the Δd components in terms of Δx and Δy are determined from the θ_M components. However, the feed displacement of Δx and Δy can only show a one-dimensional (1D) beam direction. In order to obtain

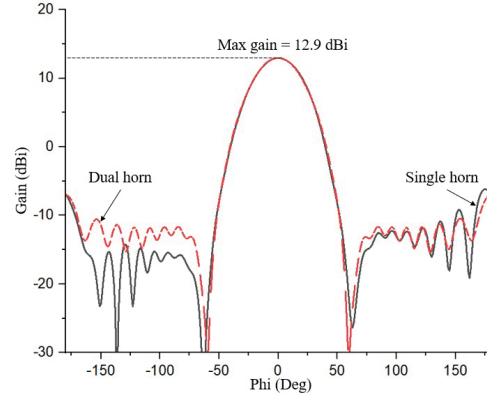


Fig. 12. Radiation patterns of single and dual horn cases.

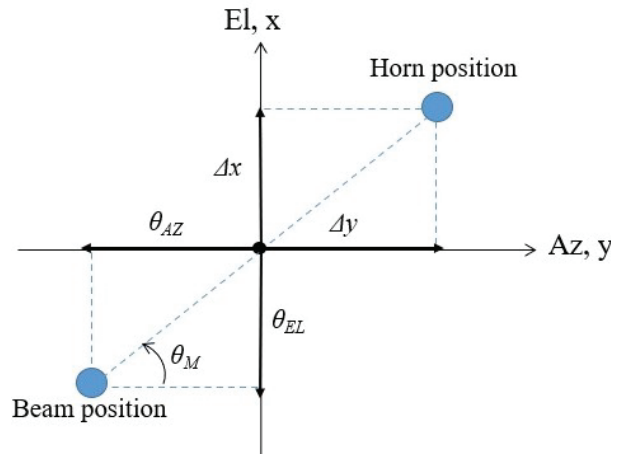


Fig. 13. Design concept of feed horn allocation.

the two-dimensional (2D) beam plot, the distances from the centre of the reflector to the caustic point can be estimated by the following equation, as described in [12]:

$$S(\Delta d, \Delta z) = F \cos \theta_M, \quad (16)$$

where

$$\Delta z = \sqrt{F^2 + \Delta d^2 - S^2}. \quad (17)$$

For the practical multi-beam allocations shown in Fig. 7, the corresponding feed positions are determined by equations (15), (16) and (17). Through calculation, the resulting beam and feed positions are summarized

Table 3: Feed position for multi beam

Beam	Beam Position		Feed Position		
	$\theta_{AZ} (^{\circ})$	$\theta_{EL} (^{\circ})$	Δy (m)	Δx (m)	Δz (m)
B1	-1.35	0.03	0.311	-0.007	-0.007
B2	-1.30	-0.29	0.307	0.068	-0.007
B3	-1.03	-0.42	0.243	0.099	-0.004
B4	-0.84	-0.75	0.207	0.161	-0.003
B5	-1.05	-0.10	0.268	0.023	-0.004

in Table 3. Based on the optimization of parameters in section II, all horns are arranged well without horn overlapping. Figure 14 shows the calculated feed horn arrangement for five beams.

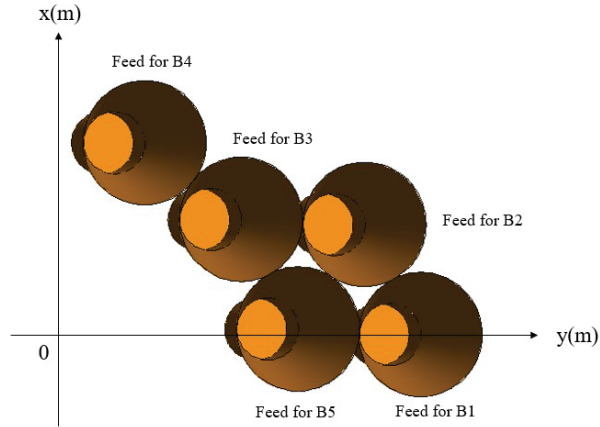


Fig. 14. Non-overlapping feed horn arrangement for five beams.

E. ANTENNA RADIATION PATTERN

The antenna configuration used in the electromagnetic simulations is shown in Fig. 15. The antenna parameters are assigned based on the values shown in Table 2 and the simulation parameters are summarized in Table 4. Method-of-Moments (MoM) technique was used to calculate the performance of feed horns and Large Element-Physical Optic (LE-PO) technique was applied to the parabolic reflector. For the case of five horn excitations, computer memory of 48.63 GB was utilized and the computation time was 142.25 hours.

Figure 16 shows the electric near-field amplitude distribution (V/m) calculated using FEKO simulator on the active region which is 75λ between the radiating ele-

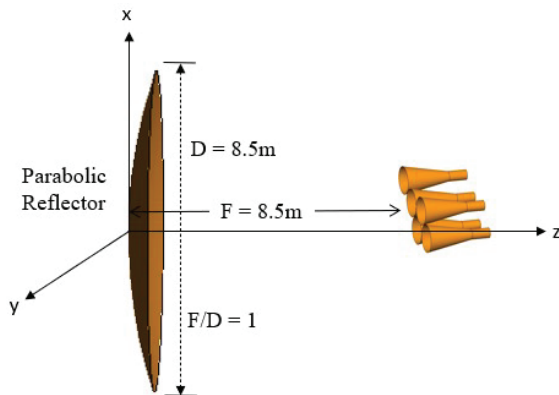


Fig. 15. Antenna configuration used in electromagnetic simulations.

ment aperture and the reflector. By observing the distribution, the on-focus near-field pattern, which is at (0,0) is demonstrated in Fig. 16 (a). Meanwhile, Figs. 16 (b) to (f) show the electric near-field pattern when the feed

Table 4: Simulation parameters used for the electromagnetic simulations

Item	Parameters	Details
Computer	Memory (RAM)	128 GB
	Clock time	1.8 GHz
	Simulator	FEKO
Simulation method	Reflector	LE-PO
	Feed Horn	MoM
	Radiation Pattern	PO
	Total radiation pattern	PO
Calculation process	Simulation memory	48.63 GB
	Simulation time	142.25 H

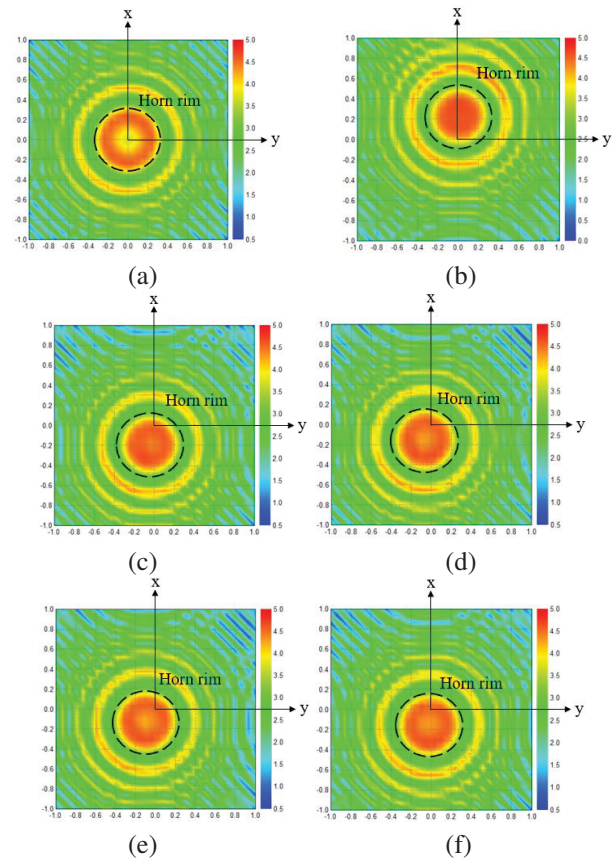


Fig. 16. (a) Aperture distribution for B0, (b) Aperture distribution for B1, (c) Aperture distribution for B2, (d) Aperture distribution for B3, (e) Aperture distribution for B4, and (f) Aperture distribution for B5.

position is shifted from the centre position at (0,0) for beams B1 to B5.

A two-dimensional (2D) calculated radiation pattern for Beam 1 (B1) and other beam allocations is shown in Fig. 17. B2 and B5 exist near the main lobe of B1, while other beams such as B3 and B4 are located in the side lobe area of B1. Each beam is connected at the beam separation angle, $\theta_S = 1.3\theta_{BA}$, where θ_{BA} is the -3 dB beam width of the reflector with a value of 0.3° . θ_S which is the beam separation corresponds to 0.39° and the crossover level becomes -6 dB from the peak level.

To validate the beam relations, the one-dimensional (1D) radiation patterns are calculated for Line 1 and Line 2 in Fig. 18. Figure 19 shows the radiation pattern generated for Line 1 at the azimuth plane, illustrating the cross-over point between B2 and B5 beam where the radiation level is reduced by -6 dB from the peak level with $\theta_S = 0.39^\circ$.

Figure 19 shows the radiation pattern generated for Line 2 at the elevation plane. The cross-over level of B3 and B4 becomes -6 dB from the peak level with $\theta_S = 0.39^\circ$. The beam shapes of the main lobe and side lobes become almost the same for B1, B3 and B4 with small deformation and gain reduction.

Finally, the antenna configuration depicted in Fig. 15 has successfully produced a contoured beam to cover Peninsular Malaysia as illustrated in Fig. 20. The design utilized five feed horns, each with identical amplitude and phase excitation coefficients to maximize the radiation towards the coverage area. The contoured beam achieved almost uniform amplitude distribution within the contour, and the Peninsular Malaysia shape is well-covered, as illustrated in Figs. 7, 4 and 17. This validates the adequateness of the contoured beam that was achieved using ‘no overlapping feed’ arrangement.

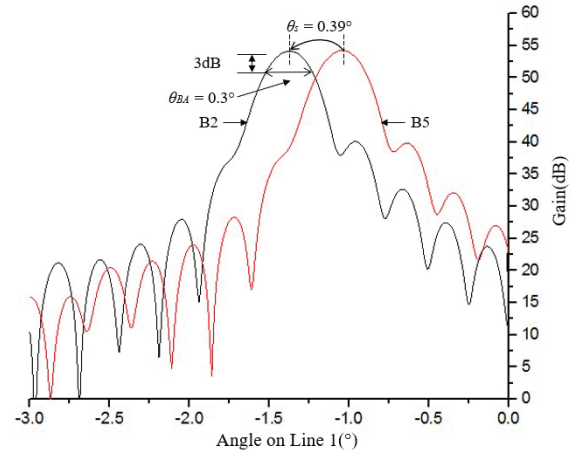


Fig. 18. Radiation patterns of B2 and B5 on the Line 1.

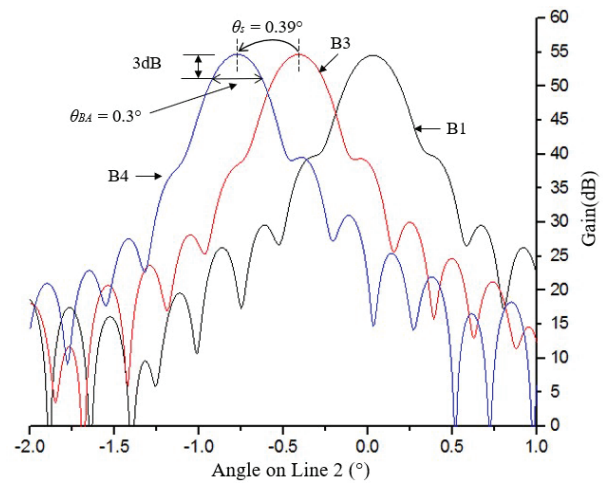


Fig. 19. Radiation patterns on B1, B3 and B4 on the Line 2.

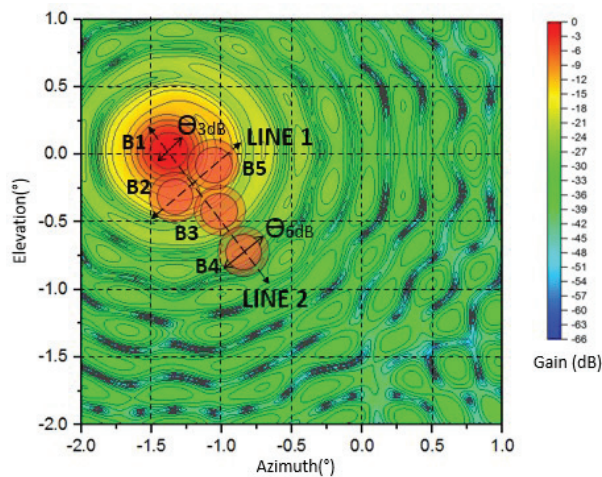


Fig. 17. Radiation pattern of B1 to B5 plotted individually in elevation and azimuth plane.

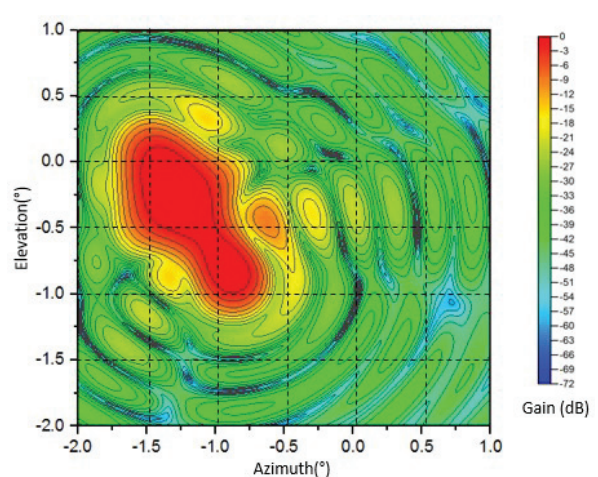


Fig. 20. Contoured beam of Peninsular Malaysia shaped.

Table 5: Comparison of the proposed technique for multi-beam antenna for contour beam shape

Ref.	Method	Description
[17]	Malaysian coverage using rectangular horn and array feed.	Rectangular horn overlapping for Malaysian coverage.
[18]	Beam coverage was synthesized based on beam amplitude and phase excitation only.	Feed is not considered.
[19]	To reduce feed size, small lens is attached at the surface of the horn.	Mutual coupling between adjacent horn is not discussed due to different frequency use.
[20]	Caribbean region coverage of Brasilsat satellite is achieved by combination of many sizes rectangular horns.	Horn overlapping escaped by employing different size of horns.
This paper	The design chart for optimisation of beam position and feed horn size is derived.	No overlapping feed horn with the same size is obtained for Malaysia beam coverage

IV. BENCHMARKING OF PRIOR RESEARCH

Previous researchers have done similar works on using multi-feed, as summarized in Table 5. Previously, feed overlapping problems or different horn sizes were shown. However, more positive trials have been developed in this paper to avoid feed overlapping.

In this paper, we proposed a useful design chart as shown in Fig. 6 that compromised equations (6), (9) and (10) that determine the feed displacement, d , horn size, H , and beam separation, θ_S . These three parameters are crucial in preventing feed overlapping. It demonstrates that the d/H value represents the judging value in mitigating overlapped horns. This value of d/H was directly proportional to θ_S , where when d/H increased, θ_S also increased, allowing feed overlapping and redundancy of beams to be omitted.

V. CONCLUSION

In this study, a method to prevent feed horn overlapping in a parabolic reflector antenna system has been proposed. To demonstrate the accuracy of the proposed method, a practical case of Malaysia contour beam design by a combination of five beams is shown. A universal design chart for feed horn sizes at many antenna configurations has been developed and, based on this design chart, the correlation between β and α to the

beam separation and horn size has been derived for no feed overlapping condition in the reflector system design. To ensure the practicality and accuracy of this design chart, a Peninsular Malaysia coverage beam antenna has been designed where the multi-beam allocations and feed horn allocations are obtained. The validity of the technique has been shown through the simulation results of the non-overlapping condition of the horn arrangement. Furthermore, the radiation beam produced for the targeted beam position is excellent, which indicates that the beam position design is accurate. The final Malaysia beam coverage obtained through the arrangement of five multi beams shows good agreement with the geographical shape of Malaysia, ensuring an excellent contour beam for Peninsular Malaysia. Overall, the proposed method has been shown to be practical and effective in mitigating feed horn overlapping in parabolic reflector antenna systems, paving the way for improved antenna system design and performance.

ACKNOWLEDGMENT

This work was supported by Universiti Teknologi MARA and Ministry of Higher Education (MOHE) for funding under the Prototype Development Research Grant Scheme (PRGS) 600-RMC/PRGS 5/3 (001/2022).

REFERENCES

- [1] measat.com. [2022, July 22]. MEASAT [Online]. Available: <http://www.measat.com/wp-content/uploads/2020/10/MEASAT-3d>. 2022.
- [2] R. C. Gupta, S. K. Sagi, K. P. Raja, N. K. Sharma, and R. Jyoti, "Shaped prime-focus reflector antenna for satellite communication," *IEEE Antennas and Wireless Propagation Letters*, vol. 16, pp. 1945-1948, Mar. 2017.
- [3] M. Maharajan, R. Jyoti, K. Sood, and S. B. Sharma, "A method of generating simultaneous contoured and pencil beams from single shaped reflector antenna," *IEEE Transaction on Antennas Propagation*, vol. 61, no. 10, pp. 5297-5301, Oct. 2013.
- [4] W. Bornemann, P. Balling, and W. English, "Synthesis of spacecraft array antennas for intelsat frequency reuse multiple contoured beams," *IEEE Transaction on Antennas Propagation*, vol. 33, no. 11, pp. 1186-1193, Nov. 1985.
- [5] S. K. Rao, "Parametric design and analysis of multiple-beam reflector antennas for satellite communications," *IEEE Antennas and Propagation Magazine*, vol. 45, no. 4, pp. 26-34, Aug. 2003.
- [6] N. J. G. Froseca and J. Sombrin, "Multi-beam reflector antenna system combining beam hopping and size reduction of effectively used spots," *IEEE Antennas and Propagation Magazine*, vol. 54, no. 2, pp. 88-99, Apr. 2012.

- [7] K. S. Rao, G. A. Morin, M. Q. Tang, S. Richard, and K. K. Chan, "Development of a 45 GHz multiple-beam antenna for military satellite communications," *IEEE Transactions on Antennas and Propagation*, vol. 43, no. 10, pp. 1036-1047, Oct. 1995.
- [8] E. R. Boudriau, "Multiple-beam antennas for military satellite communication systems," Defence Research Establishment, Ottawa, Technical Note 95-1, 1995.
- [9] N. H. Abd Rahman, M. T. Islam, N. Misran, Y. Yamada, and N. Michishita, "Generating contoured beams for malaysia region by using a caustic locus graph [Antenna Applications Corner]," *IEEE Antennas and Propagation Magazine*, vol. 56, no. 6, pp. 328-336, Dec. 2014.
- [10] J. Yahagi and M. Haneishi, "A consideration on beam-shaping of microstrip array antenna," in *Symposium on Antenna Technology and Applied Electromagnetics [ANTEM 2000]*, Winnipeg, Man, pp. 447-450, 2000.
- [11] H.-T. Chou, K.-H. Bai, C.-C. Sun, C.-T. Yu, and H.-T. Hsu, "Design of multi-beam antenna array using tapered slot elements," *2013 International Symposium on Electromagnetic Theory*, pp. 863-865, July 2013.
- [12] N. H. Abd Rahman, M. T. Islam, and Y. Yamada, "Design of shaped-beam parabolic reflector antenna for peninsular malaysia beam coverage, and its overlapping feed issues," *Applied Computational Electromagnetics Society (ACES) Journal*, vol. 30, no. 9, pp. 952-958, Aug. 2015.
- [13] T. Nurdan, T. Sonmez, and T. Fikret, "Influences of amplitude tapering and feed blockage on the radiation characteristics of Ku-band parabolic reflector antennas," *Applied Computational Electromagnetics Society (ACES) Journal*, vol. 35, no. 3, pp. 322-330, Mar. 2020.
- [14] W. L. Stunzian and G. A Thiele, *Antenna Theory and Design*, 3rd ed. New Jersey: John Wiley & Sons Inc, p. 139, 2012.
- [15] W. L. Stunzian and G. A Thiele, *Antenna Theory and Design*, 3rd ed. New Jersey: John Wiley & Sons Inc, p. 409, 2012.
- [16] C. A Balanis, *Antenna Theory Analysis and Design*, New Jersey: John Wiley & Sons Inc, p. 783, 2016.
- [17] N. H. Abd Rahman, M. T. Ali, M. T. Islam, and Y. Yamada, "Design and performance improvement of shaped-beam parabolic reflector antenna for small region coverage by non-symmetrical array feed technique," *International Journal of Applied Electromagnetics and Mechanics*, vol. 51, no. 3, pp. 307-318, Jan. 2016.
- [18] I. Aryanian and M. H. Amini, "Synthesis of contoured beam multifeed reflector antenna for optimum coverage," *Microwave and Optical Technology Letters*, vol. 63, no. 2, Feb. 2021.
- [19] Z.-Y. Zhang, Y. Zhao, N.-W. Liu, L.-Y. Ji, S. Zuo, and G. Fu, "Design of a dual-beam dual-polarized offset parabolic reflector antenna," *IEEE Transactions on Antennas and Propagation*, vol. 67, no. 2, pp. 712-718, Feb. 2019.
- [20] Y. T. Lo and S. W. Lee, *Antenna Handbook: Theory, Applications, and Design*. New York: Springer, pp. 15-80, 1993.



Nur Faiqah Fauzi received the B.Eng. in Computer Engineering from the Universiti Teknikal Malaysia Melaka (UTeM) in 2009, and the M.Sc. in Telecommunication and Information Engineering from Universiti Teknologi MARA (UiTM) in 2012. Currently she is pursuing her Ph.D. in Universiti Teknologi MARA (UiTM). Her Ph.D. works was on analyzing and designing Satellite-mount antenna for Malaysia contoured shaped coverage. Her current research interests include array antennas, antennas for space application, RF and microwave design and electromagnetic analysis.



Nurul Huda Abd Rahman (M'15) received her M.Eng. degree in electronic from University of Surrey, Guildford, United Kingdom in 2008 and Ph.D. degree in electric, electronic and systems engineering from Universiti Kebangsaan Malaysia in 2014. She joined Astronautic Technology (M) Sdn. Bhd. as a Spacecraft Engineer in 2008, where she was involved in various small-class satellite development and R&D projects. In 2014, she joined Universiti Teknologi MARA Malaysia (UiTM) and has been working in the same university until now, where she currently holds the position of Associate Professor. She also received a 2-year Postdoctoral Fellowship under the Malaysia-Japan International Institute of Technology, Universiti Teknologi Malaysia between 2018-2019. Her current research interests include antennas for space and terrestrial applications, array antennas, reflector and lens antennas, wearable and flexible antennas, RF and microwave design, and electromagnetic analysis. She is the Professional Engineer of the Board of Engineers Malaysia (BEM) since 2019. She has been appointed as the Executive Committee of the IEEE

Malaysia AP/MTT/EMC Joint Chapter for 2021-2022. She was also the recipient of the Best Professional Paper Award IEEE Malaysia Comsoc & VTS Joint Chapter in 2018 and the Best Paper Award from IEEE Malaysia AP/MTT/EMC Joint Chapter in 2018 and 2019.



Yoshihide Yamada received the bachelor's and master's degrees in Electronic Engineering from the Nagoya Institute of Technology, in 1971 and 1973, respectively, and the Ph.D. degree in electrical engineering from the Tokyo Institute of Technology, in 1989. He joined Electrical Communication Laboratories, Nippon Telegraph and Telephone Corporation (NTT) in 1973, and moved to NTT Mobile Communications Network, Inc. (NTT DoCoMo) in 1993. In 1998, he joined National Defense Academy as a Professor. In 2014, he joined the Malaysia-Japan International Institute of Technology, Universiti Teknologi Malaysia (UTM), Malaysia, as a Professor. His research interests are aperture antennas, array antennas, very small antennas, and radar cross sections. He is a fellow of IEICE Japan, a Senior Member of IEEE APS, and a member of ACES. He received the Excellent Paper Award and the Best Tutorial Paper Award from IEICE, in 2013 and 2014, respectively.



Robi'atun Adayiah Awang received the B.Eng. degree (Hons.) and M.Eng. Degree in computer & communication engineering from Universiti Kebangsaan Malaysia (UKM) in 2001 and 2005, respectively, and the Ph.D. degree from RMIT University, Melbourne, VIC, Australia, in 2016. She is currently a senior lecturer with Faculty of Electrical Engineering, Universiti Teknologi MARA (UiTM), Shah Alam, Malaysia. Her current research interests include antennas, microwave sensors and flexible and tunable electromagnetic devices. She has published several research papers in international peer-reviewed journals and proceedings.



Idnin Pasya become a member of IEEE in 2010. He received the B.E. and M.E. and Dr. Engineering degrees in Information and Communication Engineering from Tokyo Denki University in 2004, 2006 and 2015, respectively. He worked in Toshiba PC & Network, Tokyo, Japan, from 2006 to 2009 before joining the Faculty of Electrical Engineering, Universiti Teknologi MARA, Malaysia. His research interest include ultra wideband communication system, and MIMO radar and its application. He was the executive committee of Malaysia section IEEE AP/MTT/EMC joint chapter from 2017 to 2022. Dr. Idnin received the IEEE MTT Best Paper Award in 2014 IEEE Radio and Wireless Symposium. He joined University of Aizu in 2023 as an associate Professor.

Inductive Reactance Isolated Dynamic Seawater Monopole Antenna of High Efficiency

Lihua Li, Shimin Feng, and Menglei Xiu

Department of Communication Engineering
Naval University of Engineering, Wuhan 430033, China
1356521485@qq.com, fengshimin.86@126.com, menglei@163.com

Abstract – The dynamic-type seawater monopole antenna has the problem of direct connection between its radiation body and the seawater. This makes the radiation current flow into the seawater, which leads to low radiation efficiency. In this paper, a dynamic-type seawater monopole antenna of high efficiency is proposed using an inductive reactance isolated method. Based on this method, a dynamic seawater antenna of seawater inductance isolation structure is designed. According to its equivalent circuit diagram, the principle and design basis of isolation are analyzed. The FEKO software is then used to simulate the antenna's radiation efficiency. In addition, the impacts of the radius of the seawater inductance, the number of turns of the seawater coil, the diameter of the seawater coil, and the average turn spacing on the efficiency of the antenna are studied. Moreover, the experimental verification shows that the radiation efficiency of the designed dynamic seawater antenna with inductive reactance isolation structure can be greater than 70%. The value of the received carrier power in the case of inductance isolation is higher by 10 dB compared with the case without isolation.

Index Terms – Monopole antenna, radiation efficiency, seawater antenna.

I. INTRODUCTION

The water antenna has been widely studied because it is reconfigurable and it has high radiation efficiency and wide bandwidth. For different purposes, several researchers have proposed many different forms of water antenna structures, such as semi-seawater antennas [1], array seawater antennas [2], and hemispherical sea antennas [3]. This paper studies the simple monopole water antenna in structure form. From the supply side of the flow, the water antennas are divided into static and dynamic monopole antennas. Compared with the static water monopole antenna [4–8], carried by the insulating body and not flowing, the dynamic monopole water antenna [9, 10] can control the height and turn off or turn on the water stream in real time by controlling the water pump. Thus, the operating frequency band is

wider, the use is more flexible, and it is more suitable for maritime wireless communication such as the one used on ships and unmanned ships. However, the seawater radiation part of the dynamic seawater antenna is directly connected to the sea, which decreases its feeding and radiation efficiency [11]. The mode of feeding method of plate capacitive coupling, of which radiation efficiency is 35% at 110 MHz, is presented in [1]. The feeding method of a gamma-shape feeding arm, which can achieve radiation efficiency of 56.2 % at 56.5 MHz, was also proposed [12]. Although these feed methods solve the feeding problem and improve the efficiency to a certain extent, the seawater antenna is connected to the water. Therefore, its current will be diverted to it. Thus, this study focuses on the reduction of this partial current. This paper proposes an inductive reactance isolated method to improve the radiation energy of dynamic seawater antennas. Based on this method, a dynamic seawater antenna isolated by a novel seawater inductance is designed. The simulation and experiment demonstrate that the effect of the separating current of the two isolated methods is significant, and the antenna's radiation efficiency is improved.

II. STRUCTURE OF THE INDUCTIVE REACTANCE ISOLATED DYNAMIC SEAWATER MONOPOLE ANTENNA

Figure 1 shows a schematic diagram of a dynamic monopole seawater antenna isolated by a seawater inductance coil, which consists of seawater inductance, conductive jet (conducting strap), ground plane, and water stream supplied by a pump. When the antenna is in operation, the seawater is first pumped into the seawater inductance, which consists of a certain length of the spiral insulated tube from which the seawater is ejected to form a monopole seawater antenna. A metal tube is used as the seawater jet at the upper part of the seawater inductance. The method of feed is used for direct feeding. The signal end of the feeder is directly fed to the jet, and the signal is coupled to the seawater antenna through the jet to radiate out. The grounding end is connected to the ground plate, which is in contact with the seawater.

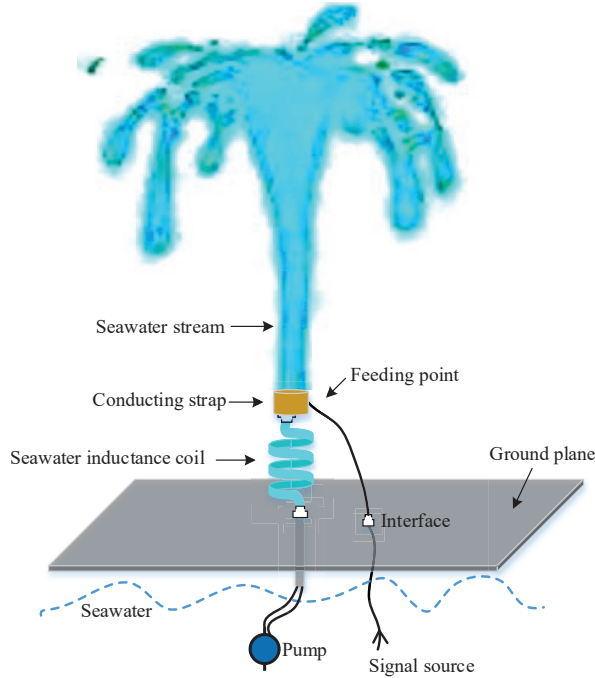


Fig. 1. Schematic of a dynamic seawater monopole antenna isolated by a seawater inductance coil.

In this study, the seawater inductance has a high impedance, acting as a barrier to high-frequency current.

III. THE PRINCIPLE OF INDUCTIVE ISOLATION

The inductive isolation shown in Fig. 1 consists of an inductance element formed by the flow of spiral seawater connected to the root of the seawater monopole antenna. When the antenna works at high frequency, it presents a high impedance characteristic, which isolates the upper seawater antenna radiator from the lower seawater surface. The seawater inductance has sufficient impedance characteristics at high frequency, equivalent to the insulator's function at the bottom of the common metal pole monopole antenna.

A. Impedance characteristics of the seawater inductance

The spiral seawater inductor is an inductance element that presents a distributed capacitance (C_d) between the turns of the spiral seawater inductor and the DC resistance (R_2). The equivalent circuit diagram formed by these three elements is shown in Fig. 2. The contribution of C_d to the overall impedance (Z) of the seawater inductance is significant [13], as shown in Equation (1). C_d is related to the radius of the seawater inductance, the average turn spacing, and the diameter of the seawater coil, as shown in Equation (2). Equation (3) presents the inductive resistance (X_{Total}), that is, the

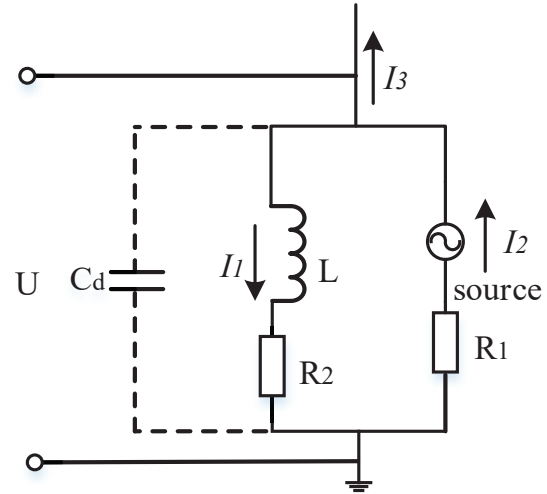


Fig. 2. Equivalent circuit diagram for the inductance isolation of seawater.

isolation impedance. The greater the value of X_{Total} , the more significant the isolation effect.

$$Z = \frac{R_2}{\omega^2 C_d^2 R_2^2 + (\omega^2 L C_d - 1)^2} + j \frac{\omega [L - C_d (R_2^2 + \omega^2 L^2)]}{\omega^2 C_d^2 R_2^2 + (\omega^2 L C_d - 1)^2}, \quad (1)$$

$$C_d = \frac{4\pi (r_0 \sqrt{2\omega\sigma\mu} - 1)}{N(N-1)(2\pi D + \bar{d})\omega^2\mu} \left(\omega > \frac{1}{2\sigma\mu r_0^2} \right), \quad (2)$$

$$X_{Total} = \frac{\omega [L - C_d (R_2^2 + \omega^2 L^2)]}{\omega^2 C_d^2 R_2^2 + (\omega^2 L C_d - 1)^2}, \quad (3)$$

where σ is the electrical conductivity of seawater, μ is the permeability of seawater, ω is the angular frequency, r_0 is the radius of the seawater inductance, N is the number of turns of the seawater coil, D is the diameter of the seawater coil, \bar{d} is the average turn spacing, which can be calculated as $\bar{d} = l/N$, l is the length of the water coil, and L is the seawater inductance, which is expressed as

$$L = \frac{\mu}{2\pi} N^2 r_0 \Phi, \quad (4)$$

where Φ is given by $a = N^2 \bar{d} / 2r_0$ in [14].

B. Radiation characteristics

The seawater spiral coil or ferrite ring that satisfies the inequation $X_{Total} \gg R_1$ is considered to isolate the following radiation current:

$$I_3 = I_1 - I_2 = \frac{U}{R_1} - \frac{U}{X_{Total}}. \quad (5)$$

The greater the value of $\frac{X_{Total}}{R_1}$, the lower the value of I_1 , and the greater the value of I_3 .

IV. SIMULATIONS

Based on the above theoretical analysis, an inductance isolation structure of the dynamic seawater antenna was designed. The structure design has a significant

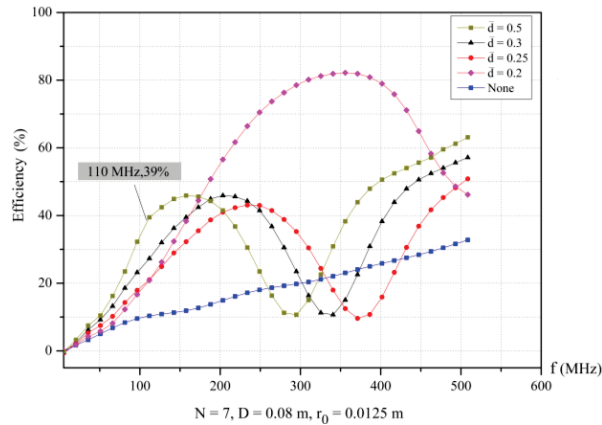


Fig. 3. Relationship between efficiency and frequency at different \bar{d} values.

impact on the radiation characteristics of the antenna. The relationship between radiation efficiency and frequency is determined through the simulation while taking into consideration the parameters r_0 , N , D , and \bar{d} .

It can be seen from Figs. 3-6 that the radiation efficiency of the dynamic monopole seawater antenna with seawater inductance is generally improved for different parameters, especially at a higher frequency band. However, the radiation efficiency decreases in some frequency bands depending on the selection of parameters. At a certain frequency, the radiation efficiency varies with the change of the inductance parameters of seawater, as shown in Fig. 3. When the average turn spacing is 0.2, the radiation efficiency of the entire band is higher than that without the isolation inductance. The radiation efficiency is 80% at 350 MHz, while at this frequency, if the average turn spacing is 0.25 or 0.3, the radiation efficiency is lower than that without the isolation inductance. However, in other frequencies, such as the frequency interval of less than 300 MHz, when the average turn spacing is 0.3, the radiation efficiency with the isolation inductance is significantly better than that without using it. It can also be seen that when the average turn spacing is 0.5, the obtained radiation efficiency is 39% at 110 MHz, which is higher than that of 35% obtained in [9]. Similarly, in Figs. 4-6, according to the difference of D , r , and n parameters, the appropriate operating frequency is selected, and the radiation efficiency can always be better than that without the isolation inductance. It can be seen from Fig. 6 that the higher radiation efficiency is at 215-245 MHz, which parameter of isolation inductance is consistent with the experiment. Therefore, the parameters of the seawater antenna can be reasonably optimized according to the operating frequency during the actual use.

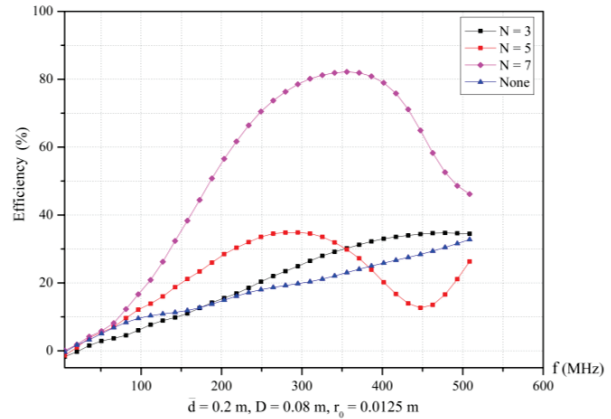


Fig. 4. Relationship between efficiency and frequency at different N values.

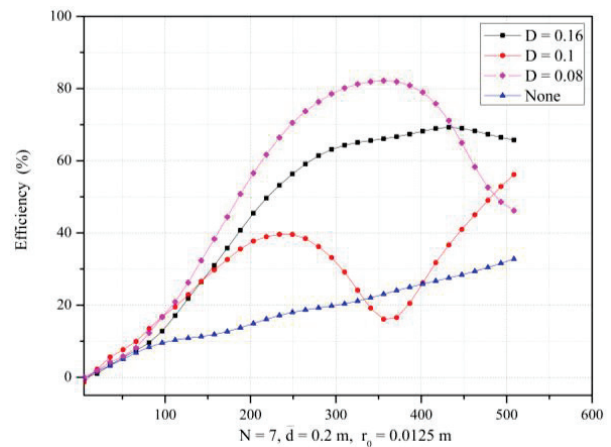


Fig. 5. Relationship between efficiency and frequency at different D values.

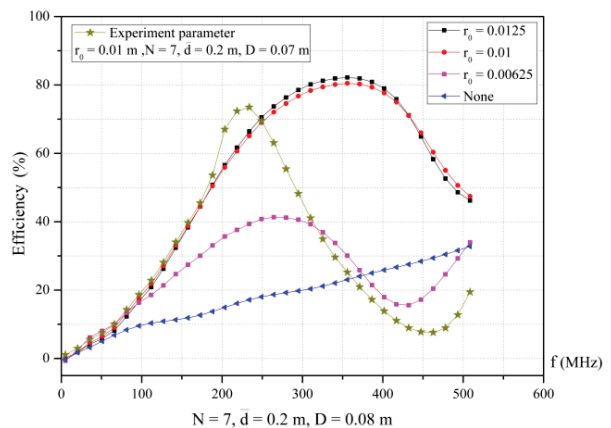


Fig. 6. Relationship between efficiency and frequency at different r_0 values.

V. EXPERIMENT

To verify the isolation effect of the inductive reactance part, the transceiver system shown in Fig. 7 is constructed. The transmitter is made of the seawater monopole antenna and an ICOM radio. The receiver is made of a ferrite antenna and a G39 software receiver model, which is used to measure the received average mean carrier power. Before transmitting, the voltage standing wave ratio (VSWR) is measured by network analyzer connected with the seawater antenna in order to choose the optimal working frequency.

The dynamic seawater monopole antenna with seawater inductance isolation and direct feeding shown in Fig. 8 was placed in a 3×5 m seawater test pool. At the bottom of the antenna, there is a metal foil plate connected with seawater. r_0 , N , D , \bar{d} , and the seawater inductance are equal to 1 cm, 7, 7 cm, 0.2 m, and 220 H, respectively. The seawater stream draws out from the seawater pool by a bump to form a seawater antenna hav-

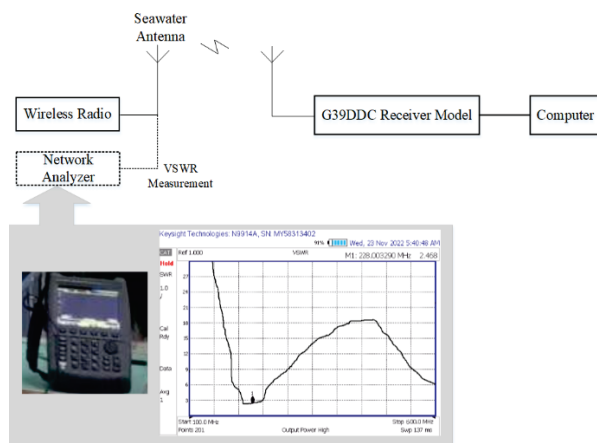


Fig. 7. Experiment of the transceiver system.



Fig. 8. The seawater antenna with isolation part.

ing a height of 1.3 m and a diameter of 4 cm. The seawater antenna is used as a transmitting antenna. Within the frequency range of 215-245 MHz, the VSWR can be determined using a network analyzer, as shown in Fig. 9. The green line in Fig. 6 represents the simulation results of the radiation efficiency of the antenna with the experiment parameters. Because the VSWR is less than 2.52 within the frequency range of 215-245 MHz, the loss of reflection power in this interval is 18.65% according to the relationship between the reflection coefficient and VSWR. Radiation efficiency is the ratio of antenna radiation power to input power, which is difficult to measure directly. While the radiation efficiency is related to matching characteristics and the loss of the antenna, and the seawater antenna has a higher conductivity, the radiation efficiency of the seawater antenna can be greater than 70%, assuming the resulting loss

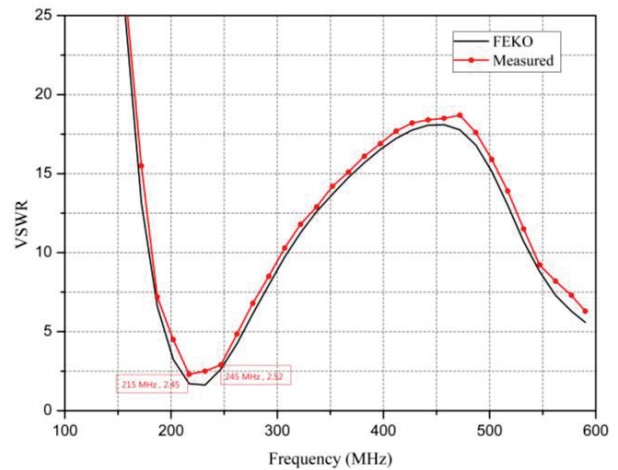


Fig. 9. VSWR of the seawater antenna with inductance isolation.

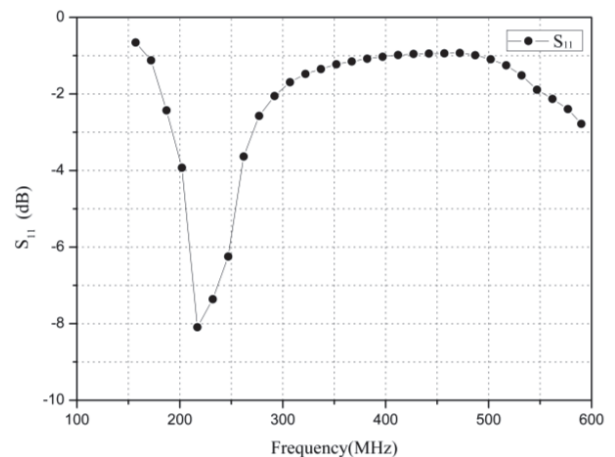


Fig. 10. S_{11} of the seawater antenna with inductance isolation.

is almost 10%. This is consistent with the simulation. Figure 11 shows the measured and simulated radiation pattern. In the experiment, it is measured once per 20 degrees in the largest radiation direction (theta = 55). Table 1 shows the mean value of the received carrier power (\bar{P}) with and without seawater inductance isolation. It can be seen that the value of \bar{P} in the case of inductance isolation is higher by 10 dB than that without isolation. Therefore, the method of inductive resistance can be used to increase the radiation efficiency.

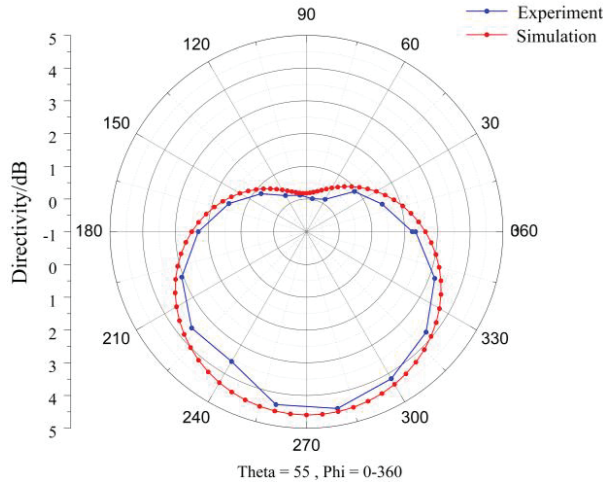


Fig. 11. Directivity of the seawater antenna with inductance isolation.

Table 1: Mean values of \bar{P} (dBm) with a receiving noise of -120 dBm

Operating Frequency	215 MHz	225 MHz	235 MHz	245 MHz
with seawater inductance isolation	-68	-65	-64	-62
without seawater inductance isolation	-79	-74	-73	-74

VI. CONCLUSION

In this paper, an improved dynamic seawater antenna is proposed. The radiation efficiency of the proposed antenna is improved using the inductance isolation method. This method solves the problem of direct connection between the radiation body of the dynamic seawater antenna and the seawater, which makes the radiation current flow into the seawater, leading to the low radiation efficiency. The simulation and experiment show that the proposed method can improve the radiation efficiency of the dynamic seawater antenna, and it can be greater than 70%. Optimization design is an important part of seawater antenna induction design. In future

research, the optimization algorithm of seawater parameters can be further studied, which could lead to better efficiency of radiation. The seawater inductance is perfectly combined with the single polar seawater antenna in structure.

In future work, we aim at conducting a sea test. The sea environment can verify the greater low-frequency segment radiation characteristics, and the impact of the sea waves on the radiation efficiency can be further analyzed, which is a factor that should be considered in practice.

ACKNOWLEDGMENT

This work was supported by the National Natural Science Foundation of China (41774021; 41874091; 42074074) and National Natural Science Foundation of China Youth Fund (62101579).

REFERENCES

- [1] C. Hua and Z. Shen, "Sea-water half-loop antenna for maritime wireless communications," *Proceedings of the 2015 IEEE 4th Asia-Pacific Conference on Antennas and Propagation (APCAP)*, Indonesia, Bali Island, June 2015.
- [2] X. Pan, Z. Hu, M. Zheng, Z. Ren, and Q. Chen, "A UHF sea-water array antenna for maritime wireless communications," *CSAA/IET International Conference on Aircraft Utility Systems (AUS 2353)*, China, Guiyang, June 2018.
- [3] F. Sun, X. Lei, Q. Xu, X. Kong, H. Wang, and G. Zhang, "An attitude independent liquid dielectric resonant antenna," *IEEE Antennas and Wireless Propagation Letters*, vol. 21, no. 11, pp. 1-4, 2022.
- [4] Y. Kosta, "Liquid antenna," *Proceedings of IEEE AP-S Int. Symp. Dig.*, USA, CA, June 2004.
- [5] H. Fayad and P. Record, "Broadband liquid antenna," *Electronics Letters*, vol. 42, no. 3, pp. 133-134, 2006.
- [6] E. Paraschakis, H. Fayad, and P. Record, "Ionic liquid antenna," *Proceedings of the Proc. IEEE Int. Workshop Antenna Tech.: Small Antennas and Novel Metamaterials*, Singapore, Mar. 2005.
- [7] L. Xing, Y. Huang, S. Alja'afreh, and S. Boyes, "A monopole water antenna," *Proceedings of IEEE 2012 Loughborough Antennas and Propagation Conference (LAPC)*, United Kingdom, Leicestershire, Nov. 2012.
- [8] G. Li, G. Gao, L. Bian, and Z. Lu, "A tunable antenna with the combination of two kinds of liquid materials," *Applied Computational Electromagnetics Society (ACES) Journal*, vol. 32, no. 11, pp. 966-973, 2017.
- [9] C. Hua, Z. Shen, and J. Lu, "High-efficiency seawater monopole antenna for maritime wireless

communications," *IEEE Trans. Antennas Propag.* vol. 62, no. 12, pp. 5968-5973, 2014.

- [10] SPAWAR, "Sea water antenna system," SSC Pacific, San Diego, CA, Apr. 2011. [Online] <http://www.public.navy.mil/spawar/Pacific/TechTransfer/ProductsServices/Pages/SeaWaterAntennaSystem.aspx> and <https://www.youtube.com/watch?v=9tIZUhu21sQ>.
- [11] A. Chatterjee, S. Chatterjee, S. Chatterjee, S. Ray, P. Adhikary, and B. Roy, "Analysis of sea water liquid antenna," *Proceedings of the 2020 4th International Conference on Electronics, Materials Engineering and Nano-Technology (IEMENTech)*, India, Kolkata, Oct. 2020.
- [12] C. Hua and Z. Shen, "Shunt-excited sea-water monopole antenna of high efficiency," *IEEE Trans. Antennas Propag.* vol. 63, no. 11, pp. 5185-5190, 2015.
- [13] Y. Wang, X. Luo, Y. Zhang, N. Zhang, and J. Gao, "Distributed capacitance of spiral coils and its magneto-capacitance effect," *Applied Physics*, pp. 44-49, 2013. [Online, Mar. 2013] <http://www.hanspub.org/journal/app.html>.
- [14] Каланга, *Inductance Calculation Manual*, China Machine Press, 1990.



Lihua Li was born in Hubei Province of China. She received her bachelors and masters degrees from the Naval Engineering University. She is studying for a Ph.D. degree in Naval Engineering University. The main research direction is wireless communication. Currently working as an associate professor in the Communication Engineering Teaching and Research Section of Naval Engineering University, mainly responsible for teaching and research tasks. She has published many papers in international conferences and journals and has been invited many times.



Menglei Xiu was born in Anhui Province of China. He received a bachelor of Science and Technology in 2016 and a masters degree from Naval University of Engineering in 2022. He is studying for a doctors. degree in Naval University of Engineering. He worked as an assistant in the Department of Communication Engineering at Naval University of Engineering. The main research direction is wireless communication. A total of 3 articles have been published in international conferences and journals and have been indexed.



Shimin Feng (corresponding author) received his B.S., M.S., and Ph.D. in 2009, 2001, 2015 from Naval Engineering University. The main research direction is wireless communication. Currently working as an associate professor in the Communication Engineering Teaching and Research Section of Naval Engineering University, mainly responsible for teaching and research tasks. He has published several papers in international conferences and journals.

Design of Wilkinson Power Dividers with SITL Compensated Microstrip Bandpass Filters

Ravee Phomlounsri¹, Somkuan Srisawat¹, Somchat Sonasang², and Mitchai Chongcheawchamnan³

¹Department of Computer and Communication Engineering, Faculty of Technology
Udon Thani Rajabhat University, Udon Thani 4100, Thailand
phravee@gmail.com, somkaun.srisawat@gmail.com

²Department of Electronics Technology, Faculty of Industrial Technology, Nakhon Panom University
Nakhom Panom, 48000, Thailand
somchat.s@npu.ac.th

³Department of Electrical Engineering
Prince of Songkla University, Hat Yai, Songkhla 90110, Thailand
mitchai@coe.psu.ac

Abstract – This paper presents a simple technique for improving performances of a conventional Wilkinson power divider. The technique is achieved by replacing bulky quarter-wave transmission lines with stepped impedance transmission lines (SITL) compensated coupled lines. With the internal function of bandpass filter integrated with the proposed coupled lines, the spurious response at 2nd harmonics frequencies that normally exists in the conventional divider is considerably reduced. Simulated and measured results at 2.1 GHz operating frequency of the proposed and conventional Wilkinson power divider were compared. The proposed divider achieves -3.8 dB insertion loss (S_{21}, S_{31}) and more than 25 dB return loss (S_{11}, S_{22}, S_{33}) across 10% fractional bandwidth. Based on this measurement, the proposed circuit achieves more than 34.5 dB suppression at the 2nd harmonic frequency.

Index Terms – Harmonic suppression, parallel-coupled line, step impedance transmission line, Wilkinson power divider.

I. INTRODUCTION

Microwave circuits have many applications such as filter circuit [1], reflectometer [2], diplexer [3], Wilkinson power divider/combiner [4–6], microstrip add-drop multiplexer [7, 8], and microwave sensor application [9, 10]. Since the microwave circuit is implemented and developed with the microstrip substrate material, the Wilkinson power divider is a general microwave and millimeter wave communication circuit [11].

The Wilkinson power divider was first introduced by Wilkinson [4] and is an essential component

for microwave and millimeter-wave applications. It is widely used because of its helpful property of being perfectly matched at all ports and sound isolation between the output ports [11, 12]. Moreover, the Wilkinson power divider is widely used to design and implement microstrip coupled lines. The non-homogeneous nature of physical parallel coupled lines microstrip gives rise to spurious frequencies, particularly beyond the second harmonic frequency. To address this issue, compensation techniques such as inductive [13, 14] and capacitive [15, 16] methods are commonly employed. These techniques play a crucial role in mitigating the effects of non-idealities, thereby enhancing the performance and reliability of microstrip-based circuits. Notwithstanding, researchers have presented Wilkinson power divider techniques for harmonic suppression frequencies such as an anti-coupled line [17], parallel-coupled line structure [18], looped coupled-line [19], inductively loaded microstrip line [20], and bandpass or band stop filter [21–23]. The utilization of power divider applications needing a narrowband divider and bandpass filter designs are prevalent in the construction of I-Q demodulator topologies, leading to the creation of simplified circuits [24–27]. For RF and microwave circuit design, including balanced amplifiers, phase shifters, image rejection mixers, I/Q modulators, and circularly polarized antenna polarizers, the techniques mentioned above can produce spurious harmonic frequencies. However, those techniques have limitations on the complexity of the circuit.

The Wilkinson power divider consists of two quarter-wavelength branches of transmission lines with a characteristic impedance and a termination resistor, as

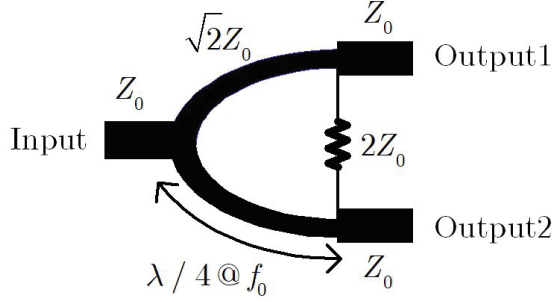


Fig. 1. Schematics of conventional Wilkinson power divider.

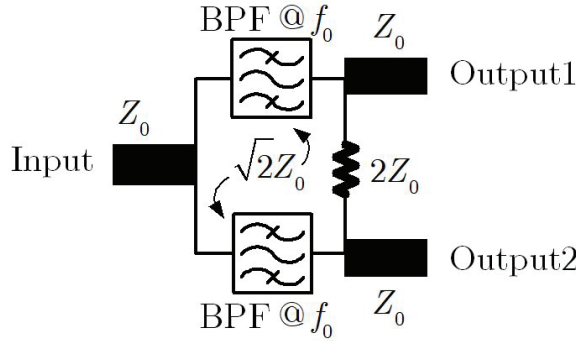


Fig. 2. Schematics of the proposed integrated bandpass filter Wilkinson power divider.

shown in Fig. 1. The power divider is designed based on the electrical length of a desired fundamental frequency. Still, high-order harmonic signals usually appear at the output ports due to the periodic characteristics of the transmission lines. Using the quarter-wavelength branches of transmission lines will unavoidably lead to poor selectivity in each transmission path. Intuitively, the selectivity can be improved by adding an extra high-order bandpass filter before the input or after each output port of the power divider. Still, the sizeable total circuit area may be a terrible problem. The concept of this research work is to add the BPF function in the divider without circuit size trade-off as shown in Figs. 1 and 2, a quarter-wave transformer is replaced with a transformer with integrated BPF. The basic theory of the proposed topology is described in Section II. Design and experimental results will be described in Section III. The paper is finally concluded in Section IV.

II. THEORY

A. The step impedance transmission lines resonator

Step impedance transmission lines (SITL) are non-uniform transmission lines, which were used in the filter design to reduce the circuit sizes [28, 29], to shift the spurious to higher band, and to suppress multiple spu-

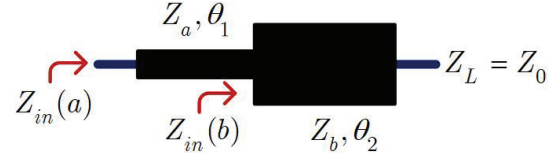


Fig. 3. Schematic of the proposed step impedance transmission line.

rious passband [29]. The SITL employed in this paper is shown in Fig. 1. It consists of two cascaded transmission lines with characteristic impedances Z_a and Z_b and electrical lengths θ_1 and θ_2 , respectively. In this technique, $Z_a > Z_b$, so the impedance ratio $R_z = Z_a/Z_b$ is aligned between $0 \leq R_z \leq 1$. As shown in Fig. 4, the SITL is proposed to connect at the coupled lines port to suppress signal transmission between port 1 and port 3 of the coupled lines. To achieve this condition, the electrical parameters of coupled lines ($Z_0, Z_{0e}, Z_{0o}, \epsilon_{effe}, \epsilon_{effo}$) should be chosen optimally.

Based on the above-mentioned condition, the optimum directivity at operating frequency (f_0) of coupled-line occurs when the signal transmission of ports 1 and 3 is enforced to be nearly zero or $S_{31}(f_0) \approx 0$, which will occur as the driving point impedance from the coupled port to the SITL for this design $Z_{in}(a)$ is also enforced to [30]:

$$Z_{ZT}(f_0) = -j \frac{(Z_{0o}^2 Z_{0e} \sin \theta_0 - Z_{0e}^2 Z_{0o} \sin \theta_e) + 2Z_0 Z_\beta + Z_0 Z_\alpha}{Z_\alpha + Z_\beta}, \quad (1)$$

where $Z_\alpha = jZ_0(\sin \theta_0 - \sin \theta_e)$ and $Z_\beta = Z_0^2(\cos \theta_0 - \cos \theta_e)$.



Fig. 4. The proposed coupled lines based SITL compensated coupled lines.

The input impedance $Z_{in}(a)$ of the SITL section at operating frequency (f_0) is related to the coupled lines electrical parameters. To preserve or minimize the change of the coupling coefficient of the proposed coupled lines, its electrical length $\theta_s(f_0)$ should be shortened and computed from:

$$\theta_s = \frac{1}{\Theta} \cot^{-1} \left(\frac{2\pi f_0 (Z_{in}(a) - Z_0)}{Z_{0o}} \right). \quad (2)$$

B. Proposed BPF resonator based SITL compensated coupled lines

Based on the impedance parameters [11], the relationship between voltages and currents at each port shown in Fig. 5, are given as follows:

$$V_1 = Z_{11}I_{11} + Z_{12}I_{12} + Z_{13}I_{13} + Z_{14}I_{14}, \quad (3)$$

$$V_2 = Z_{21}I_{21} + Z_{22}I_{22} + Z_{23}I_{23} + Z_{24}I_{24}, \quad (4)$$

$$V_3 = Z_{31}I_{31} + Z_{32}I_{32} + Z_{33}I_{33} + Z_{34}I_{34}, \quad (5)$$

$$V_4 = Z_{41}I_{41} + Z_{42}I_{42} + Z_{43}I_{43} + Z_{44}I_{44}, \quad (6)$$

where V_n and I_n ($n = 1..4$) are each ports voltage and current. From the initial condition in Fig. 5, where $V_4 = 0$ and $V_2 = -I_2Z_{ST}$, then 4-port network is transformed to 2-port bandpass filter, and the relationship between voltage, current and impedance of 2-port network are as in equation (7):

$$\begin{bmatrix} V_1 \\ V_2 \end{bmatrix} = \begin{bmatrix} Z_{11T} & Z_{12T} \\ Z_{21T} & Z_{22T} \end{bmatrix} \begin{bmatrix} I_1 \\ I_2 \end{bmatrix}, \quad (7)$$

where

$$Z_{11T} = \left(Z_{11} - \frac{Z_{12}^2}{Z_{ST} + Z_{11}} \right) + \left(Z_{14} - \frac{Z_{12}Z_{13}}{Z_{ST} + Z_{11}} \right) Z_{\Theta}, \quad (8)$$

$$Z_{12T} = \left(Z_{13} - \frac{Z_{12}Z_{14}}{Z_{ST} + Z_{11}} \right) + Z_{\Phi}, \quad (9)$$

$$Z_{21T} = \left(Z_{13} - \frac{Z_{12}Z_{14}}{Z_{ST} + Z_{11}} \right) + \left(Z_{12} - \frac{Z_{13}Z_{12}}{Z_{ST} + Z_{11}} \right) Z_{\Theta}, \quad (10)$$

$$Z_{22T} = \left(Z_{11} - \frac{Z_{12}Z_{14}}{Z_{ST} + Z_{11}} \right) + Z_{\Phi}, \quad (11)$$

when

$$Z_{\Theta} = - \left(\frac{Z_{14}(Z_{ST} + Z_{11} - Z_{12}Z_{13})}{Z_{11}(Z_{ST} + Z_{11}) - Z_{13}^2} \right), \quad (12)$$

and

$$Z_{\Phi} = - \left(\frac{Z_{12}(Z_{ST} + Z_{11} - Z_{13}Z_{14})}{Z_{11}(Z_{ST} + Z_{11}) - Z_{13}^2} \right). \quad (13)$$

From equation (7), the input reflection coefficient S_{11} and the forward transmission coefficient S_{21} of the synthesized BPF resonator are as shown in equations (14) and (15):

$$S_{11} = \frac{(Z_{11T}^2 - Z_0^2) - Z_{12T}^2}{(Z_{11T} + Z_0)(Z_{22T} + Z_0) - Z_{11T}^2}, \quad (14)$$

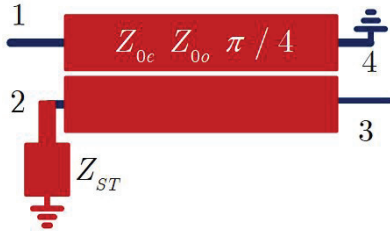


Fig. 5. The proposed BPF resonator based SITL compensated coupled lines.

$$S_{21} = \frac{2Z_0Z_{12T}}{(Z_{11T} + Z_0)^2 - Z_{12T}^2}. \quad (15)$$

These concepts, theories, and equations were employed to design a BPF resonator based SITL coupled lines at an operating frequency (f_0) of 2.1 GHz. In this paper, -10 dB coupled lines with even and odd-mode impedances of $Z_{0e} = 69.37 \Omega$, $Z_{0o} = 36.03 \Omega$, for a 50Ω system is chosen to design the proposed BPF resonator. $Z_{ST}(f_0)$ and $\theta_S(f_0)$ are calculated from equations (1) and (2). After that the impedance $Z_{ST}(f_0)$ and $\theta_S(f_0)$ electrical degree were used to calculate the electrical parameters Z_a , Z_b and θ_a , θ_b of SITL, respectively. Table 1 lists the electrical parameters of the conventional and the proposed BPF resonator based SITL compensation design for -10 dB while the electrical length of the conventional Wilkinson circuit is 0.50π rad and the proposed Wilkinson circuit is 0.42π rad, with the circuit size reduced by 0.08π rad in electrical length. The parameters of the SITL have an electrical length of 8 rad, respectively.

The frequency response (S_{21}) vs. return loss (S_{11}) curve of the conventional and the proposed BPF resonator based SITL compensated coupled lines simulated in this study are shown in Fig. 6. The simulation results of S_{21} and S_{11} presented frequency response at the same

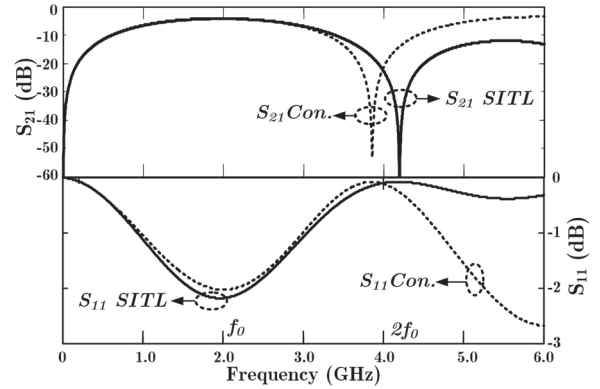


Fig. 6. S-parameters of 2.1 GHz conventional and the proposed BPF resonators.

Table 1: Parameters of the -10 dB coupled lines for BPF resonator at 2.1 GHz

Sections	Impedances (Ω)	Coupler's Length (θ , rad)	W,S,L (mm)
Cpl-SITL	$Z_{0e1} = 69.37$	0.42π	2.20, 0.17, 21.00
	$Z_{0o1} = 36.03$		
Con-Cpl	$Z_{0e1} = 69.37$	0.50π	2.20, 0.17, 25.00
	$Z_{0o1} = 36.03$		
SITL	$Z_{in}(a) = j22.20$	$Z_{a1} = 100\Omega$, $Z_{b1} = 62\Omega$	$\theta(Z_a) = \theta(Z_b) = 8^\circ$

level compensated by STIL. The resulting frequency at $2f_0$ is higher than in the conventional.

C. Transmission lines modified for second-order BPF frequency response characterization

In the paper presented here, the filter, as shown in Fig. 7 is designed using the Chebyshev bandpass prototype technique [32, 33]. The element values for the considered prototype were proposed to determine the even- and odd-mode impedances by using the admittance inverter. The method of using a higher-order parallel coupled-line bandpass filter to replace transformer [32, 33] can be utilized in the proposed equal-split Wilkinson power divider with favorable selectivity. The SITLs compensation coupled lines BPF design equations of the proposed divider can be employed [33], where N is the filter's order, z_{0ei} and z_{0oi} are the even- and odd-mode characteristic impedances of each coupled-line section, Z_0 and Δ are the system impedance and the 3-dB fractional bandwidth of the filter, $J_i, i=1,2,3,\dots,N+1$, are the admittance inverters (J-inverters), $g_i, i=1,2,3,\dots,N+1$ are the lumped element values for low-pass filter prototype. In this conventional Wilkinson power divider, the characteristic impedance of each branch of quarter-wavelength transmission lines in Fig. 1 is $\sqrt{2}Z_0$. In the proposed technique, each quarter-wavelength branch of transmission lines in the Wilkinson power divider can be replaced

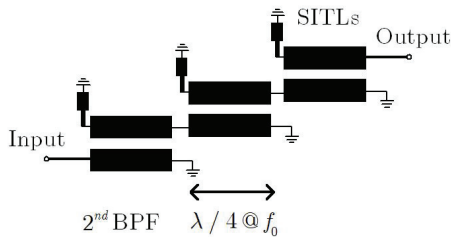


Fig. 7. Schematic of the proposed 2^{nd} order BPF SITL compensated coupled lines [31].

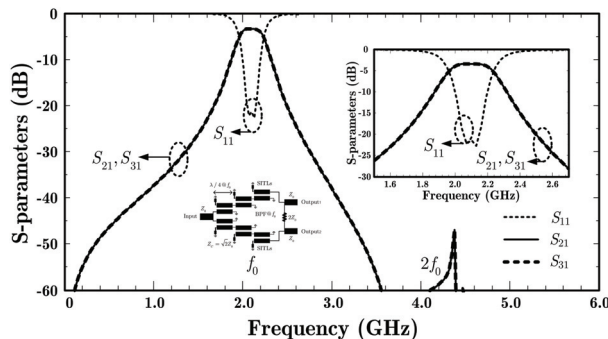


Fig. 8. Simulation results in S-parameters of the proposed Wilkinson power divider.

by the even-order coupled lines bandpass filter where the system characteristic impedance of the filter is $\sqrt{2}Z_0$ as shown in Fig. 8 and the proposed power divider has employed 2^{nd} order BPF based SITL compensated coupled lines instead of an ordinary quarter-wavelength branch of transmission lines to improve the desired selectivity in each output signal.

III. DESIGN AND EXPERIMENTAL RESULTS

To enhance the selectivity performance of the proposed Wilkinson power divider, the circuit prototype has been designed and fabricated on AD260 microwave substrate with the following design parameters: $\epsilon_r=2.60$, $h=1.00$ mm, $t=35\mu\text{m}$ and $\tan\delta=0.0017$. The centre frequency and 3-dB fractional bandwidth of each filter transformer (both upper- and lower-BPF) are around 2.1 GHz and 5% fractional bandwidth. The corresponding design parameters of each 0.5 dB equal-ripple Chebyshev filter transformer are $g_1=1.4029$, $g_2=0.7071$, $g_3=1.9841$, $Z_0J_1=0.2366$, $Z_0J_2=0.0792$, and $Z_0J_3=0.2366$. The even- and odd-mode characteristic impedances of each coupled-line section are $Z_{0e1}=91.40 \Omega$, $Z_{0o1}=57.93 \Omega$, $Z_{0e2}=76.75 \Omega$, $Z_{0o2}=65.55 \Omega$, $Z_{0e3}=91.40 \Omega$, and $Z_{0o3}=57.93 \Omega$, respectively. The physical and electrical design parameters of SITLs compensated BPF are shown in Table 2.

In Fig. 9, the simulated result of the proposed Wilkinson power divider shows the suppression performances at 4.2 GHz below the desired frequency of 2.1 GHz more than 43 dB. The measurement was performed with the E5071C Vector Network Analyzer as shown in Fig. 10, which is in good agreement with the simulated result. The implemented circuit has the measured results

Table 2: Parameters of the Wilkinson power divider with integrated BPF at 2.1 GHz

Sections	Impedances (Ω)	Coupler's Length (θ , rad)	W,S,L (mm)
Coupled lines 1	$Z_{0e1} = 91.40$ $Z_{0o1} = 57.93$	0.42π , 21.00	1.30, 0.59
Coupled lines 2	$Z_{0e2} = 76.75$ $Z_{0o2} = 65.55$	0.39π	1.50, 1.90 , 19.60
Coupled lines 3	$Z_{0e3} = 91.40$ $Z_{0o3} = 57.93$	0.42π	1.30, 0.59, 21.00
SITLs	$Z_{in}(a1) = j28.42$ $Z_{in}(a2) = j36.32$ $Z_{in}(a3) = j23.42$	$Z_{a1} = 100\Omega$ $Z_{b1} = 68\Omega$ $Z_{a2} = 100\Omega$ $Z_{b2} = 74\Omega$ $Z_{a3} = 100\Omega$ $Z_{b3} = 68\Omega$	$\theta(Z_a) = \theta(Z_b) = 8^\circ$

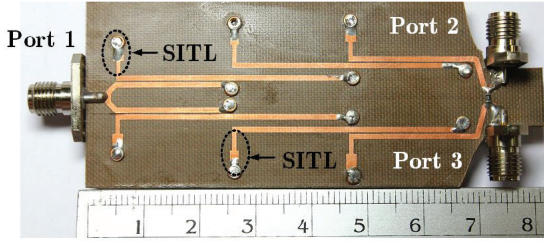


Fig. 9. PCB photograph of the proposed Wilkinson power divider.

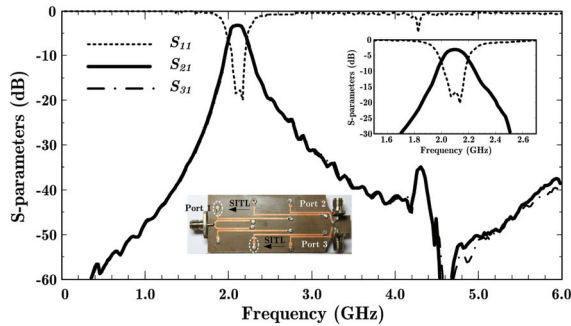


Fig. 10. Measured results s-parameters of the proposed Wilkinson power divider.

S_{21} -4.13 dB, S_{31} -4.12 dB, S_{11} -19.5 dB at the desired frequency 2.1 GHz and presents the suppression performances at 4.2 GHz more than 34.5 dB. The photograph of the PCB of the proposed frequency doubler based on a square ring resonator is shown in Fig. 11. The circuit size excluding the input and output SMA connectors of the proposed Wilkinson power divider is around 22.27 cm². Table 3 presents a summary of previous studies alongside

Table 3: The comparison of Wilkinson power dividers

Ref.	Techniques	Harmonic Suppression
Ref [4]	Open stub	> -70.00 dB
Ref [6]	LPFs	> -40.55 dB
Ref [12]	Lumped-distributed	NA
Ref [17]	Anti-coupled line	> -20.00 dB
Ref [18]	Parallel coupled line	> -30.00 dB
Ref [19]	Looped coupled-line	NA
Ref [21]	Open-short stubs	> -50.00 dB
Ref [23]	BSF	> -20.00 dB
This work	BPF	> -20.00 dB

our proposed circuit. Our design employs BPF coupled lines, which offers a simpler approach compared to the more intricate designs employed by other researchers. As a result, the proposed Wilkinson power divider proves to be more suitable for practical implementation.

IV. CONCLUSION

A modified Wilkinson power divider with integrated SITL compensated coupled lines bandpass filters has been proposed. The proposed topology has many attractive characteristics such as low insertion loss, good selectivity in each output signal path, wide stop band, and ease of design and implementation. The level of spurious response at a harmonic of the proposed Wilkinson power divider is then 34.5 dB at the 2nd harmonic frequency. It is believed that the proposed power divider can be simply modified for many microwave systems.

ACKNOWLEDGMENT

The authors would like to demonstrate gratitude toward the Faculty of Industrial Technology of the Nakhon Phanom University for research time and the Department of Computer and Communication Engineering (CCE), Faculty of Technology, Udon Thani Rajabhat University (UDRU) for the research grant, instrumentation and materials support.

REFERENCES

- [1] I. J. Bahl, *Lumped Elements for RF and Microwave Circuits*, Artech house, 2022.
- [2] S. Tantiwit, S. Somwong, and M. Chongcheawchamnan, "Dual-Frequency Six-Port Reflectometer Technique for Quality Determination of Para Rubber Latex," in *2022 International Electrical Engineering Congress (iEECON)*, pp. 1-5, IEEE, 2022.
- [3] S. Srisathit, S. Patisang, R. Phomloungsri, S. Bunjaveht, S. Kosulvit, and M. Chongcheawchamnan, "High isolation and compact size microstrip hairpin diplexer," *IEEE Microwave and Wireless Components Letters*, vol. 15, no. 2, pp. 101-103, 2005.
- [4] E. J. Wilkinson, "An N-way hybrid power divider," *IRE Transactions on Microwave Theory and Techniques*, vol. 8, no. 1, pp. 116-118, 1960.
- [5] M. Hayati and S. Roshani, "A novel Wilkinson power divider using open stubs for the suppression of harmonics," *Applied Computational Electromagnetics Society (ACES) Journal*, pp. 501-506, 2013.
- [6] S. Roshani, S. Koziel, S. Roshani, M. B. Jamshidi, F. Parandin, and S. Szczepanski, "Design of a patch power divider with simple structure and ultra-broadband harmonics suppression," *IEEE Access*, vol. 9, pp. 165734-165744, 2021.

- [7] S. Sonasang, M. Jamsai, M. Jalil, N. T. Pham, K. Ray, N. Angkawisittpan, P. Yupapin, S. Boonkirdram, M. A. Palomino-Ovando, M. Toledo-Solano, K. Misaghian, and J. Lugo, "Multiband Rabi antenna using nest microstrip add-drop filter (NMADF) for relativistic sensing applications," *Heliyon*, vol. 9, no. 2, 2023.
- [8] S. Sonasang, P. Prabpal, P. Sirikan, P. Hakaew, N. T. Pham, P. Yupapin, K. Ray, and S. Boonkirdram, "Rabi antenna using microstrip add-drop multiplexer for electron warp speed investigation," *Chinese Optics Letters*, vol. 20, no. 7, p. 073901, 2022.
- [9] S. Sonasang and R. Phromlounsri, "The measurement of water level based on parallel-coupled lines with capacitance compensation," *Creative Science*, vol. 14, no. 2, pp. 245039-245039, 2022.
- [10] S. Sonasang, S. Srisawat, R. Phromlounsri, W. Rattanangam, and N. Angkawisittpan, "Liquid Level Measurement Using Sensors with Microstrip Parallel Coupled Lines," in *2019 IEEE 2nd International Conference on Power and Energy Applications (ICPEA)*, pp. 106-109, IEEE, 2019.
- [11] D. M. Pozar, *Microwave Engineering*, John Wiley & Sons, 2011.
- [12] M. Chongcheawchamnan, N. Siripon, and I. Robertson, "Design and performance of improved lumped-distributed Wilkinson divider topology," *Electronics Letters*, vol. 37, no. 8, pp. 501-503, 2001.
- [13] R. Phromlounsri, M. Chongcheawchamnan, and I. D. Robertson, "Inductively compensated parallel coupled microstrip lines and their applications," *IEEE Transactions on Microwave Theory and Techniques*, vol. 54, no. 9, pp. 3571-3582, 2006.
- [14] S. Sonasang and N. Angkawisittpan, "Design of microstrip parallel-coupled lines with high directivity using symmetric-centered inductors," *Applied Computational Electromagnetics Society (ACES) Journal*, pp. 657-663, 2021.
- [15] M. Dydyk, "Accurate design of microstrip directional couplers with capacitive compensation," in *IEEE International Digest on Microwave Symposium*, pp. 581-584, IEEE, 1990.
- [16] M. Dydyk, "Microstrip directional couplers with ideal performance via single-element compensation," *IEEE Transactions on Microwave Theory and Techniques*, vol. 47, no. 6, pp. 956-964, 1999.
- [17] J. Zhang, L. Li, J. Gu, and X. Sun, "Compact and harmonic suppression Wilkinson power divider with short circuit anti-coupled line," *IEEE Microwave and Wireless Components Letters*, vol. 17, no. 9, pp. 661-663, 2007.
- [18] X. Yu, S. Sun, and Y. Liu, "Design of wideband filtering power dividers with harmonic suppression based on the parallel-coupled line structures," *Applied Computational Electromagnetics Society Journal (ACES)*, pp. 468-475, 2018.
- [19] H. Zhu, A. M. Abbosh, and L. Guo, "Wideband four-way filtering power divider with sharp selectivity and wide stopband using looped coupled-line structures," *IEEE Microwave and Wireless Components Letters*, vol. 26, no. 6, pp. 413-415, 2016.
- [20] E. N. Mohamed, A. G. Sobih, and A. M. El-Tager, "Compact Wilkinson power divider with Inductive loaded microstrip line for harmonics suppression," in *2016 IEEE Middle East Conference on Antennas and Propagation (MECAP)*, pp. 1-4, IEEE, 2016.
- [21] S. Lotfi, S. Roshani, S. Roshani, and M. S. Gilan, "Wilkinson power divider with band-pass filtering response and harmonics suppression using open and short stubs," *Frequenz*, vol. 74, no. 5-6, pp. 169-176, 2020.
- [22] H. S. Vaziri, S. Zarghami, F. Shama, and A. H. Kazemi, "Compact bandpass Wilkinson power divider with harmonics suppression," *AEU-International Journal of Electronics and Communications*, vol. 117, p. 153107, 2020.
- [23] R. Phromlounsri and S. Sonasang, "Design and implementation of a wilkinson power divider with integrated band stop filters based on parallel-coupled lines," *Applied Computational Electromagnetics Society (ACES) Journal*, vol. 38, no. 3, p. 208, 2023.
- [24] X. Wang, M. Yoshikawa, J. Kohagura, Y. Shima, R. Ikezoe, M. Sakamoto, T. Imai, Y. Nakashima, Z. Ma, I. Sakagami, and A. Mase, "A narrow band-pass filter type Wilkinson power divider for IQ demodulator in microwave interferometer system," *Journal of Instrumentation*, vol. 10, no. 11, p. C11005, 2015.
- [25] J.-H. Park, S.-J. Park, and M.-Q. Lee, "Quadrature Wilkinson power divider using cross-type short-circuited shunt stub for good amplitude and phase balance," *AEU-International Journal of Electronics and Communications*, p. 154783, 2023.
- [26] S. Zarghami and M. Hayati, "Narrow-band power dividers with wide range tunable power-dividing ratio," *Scientific Reports*, vol. 12, no. 1, p. 17351, 2022.
- [27] P. Cheong, K.-I. Lai, and K.-W. Tam, "Compact Wilkinson power divider with simultaneous

bandpass response and harmonic suppression,” in *2010 IEEE MTT-S International Microwave Symposium*, pp. 1588-1591, IEEE, 2010.

- [28] M. Makimoto and S. Yamashita, “Bandpass filters using parallel coupled stripline stepped impedance resonators,” *IEEE Transactions on Microwave Theory and Techniques*, vol. 28, no. 12, pp. 1413-1417, 1980.
- [29] S.-C. Lin, P.-H. Deng, Y.-S. Lin, C.-H. Wang, and C. H. Chen, “Wide-stopband microstrip bandpass filters using dissimilar quarter-wavelength stepped-impedance resonators,” *IEEE Transactions on Microwave Theory and Techniques*, vol. 54, no. 3, pp. 1011-1018, 2006.
- [30] S. Kumpang, R. Phromlounsri, and M. Chongcheawchamnan, “Design high-directivity parallel-coupled lines with step-impedance transmission lines,” in *2007 Asia-Pacific Microwave Conference*, pp. 1-4, IEEE, 2007.
- [31] S. Kumpang, R. Phromlounsri, M. Chongcheawchamnan, M. Krairiksh, and I. Robertson, “Design and application of microstrip parallel-coupled lines employing step-impedance transmission-line compensation,” *IET Microwaves, Antennas & Propagation*, vol. 3, no. 3, pp. 410-415, 2009.
- [32] G. Mahttei, L. Young, and E. Jones, “Microwave filters, impedance matching networks, and coupling Structure,” Norwood, MA, Artech House, 1980.
- [33] J.-S. G. Hong and M. J. Lancaster, *Microstrip Filters for RF/Microwave Applications*, John Wiley & Sons, 2004.



Ravee Phromlounsri was born in Khon Kaen, Thailand. He received the B.Sc. (Applied Physics in Solid State Electronics) from King Mongkut Institute of Technology, Ladkrabang (KMITL), in 1992, M.Eng. in Electrical Engineering (Telecommunication) from Mahanakorn University of Technology (MUT), in 2000 and he is currently working toward the D.Eng. in Electrical Engineering in MUT. From 1992 to 2009, he joined MUT as a lecturer in the telecommunication engineering department. Currently, he is an assistant professor in the Department of Computer and Communication Engineering at Udon Thani Rajabhat University. His research interests include IoT/Automation system, and RF/Microwave circuits design.



Somkuan Srisawat was born in Nongbua Lamphu, Thailand. He received the B.Eng. (Electronics Engineering) from Udon Thani Rajabhat University, in 2011, M.Eng. in Electrical and Computer Engineering from Mahasarakham University (MSU), in 2019, Thailand.

Currently, he is working in the Department of Computer and Communication Engineering at Udon Thani Rajabhat University. His research interests include IoT/Automation system, and RF/Microwave circuits design.



Somchat Sonasang was born in Nongbua Lamphu, Thailand. He received the B.Eng. (Electronics and Telecommunication-Telecommunication) from Rajamangala University of Technology Isan(RMUTI), Nakhon Ratchasima Campus, in 2006, M.Eng. in Electrical Engineering from Khon Kaen University (KKU), in 2009, Ph.D. degree in electrical and computer engineering from Mahasarakham University (MSU), Maha Sarakham, Thailand, in 2021. He is currently working in the Department of Electronic Technology, Faculty of Industrial Technology, Nakhon Phanom University, Thailand. His current research interests are microwave circuits, electromagnetic material characterization, non-destructive tests, Rabi oscillation and antenna.

His current research interests are microwave circuits, electromagnetic material characterization, non-destructive tests, Rabi oscillation and antenna.



Mitchai Chongcheawchamnan (Senior Member, IEEE) was born in Bangkok, Thailand. He received the B.Eng. degree in telecommunication from the King Mongkut's Institute of Technology Ladkrabang, Bangkok, in 1992, the M.Sc. degree in communication and signal processing from Imperial College London, London, U.K., in 1995, and the Ph.D. degree in electrical engineering from the University of Surrey, Guildford, U.K., in 2001.

He joined the Mahanakorn University of Technology, Bangkok, as a Lecturer, in 1992. In 2008, he joined the Faculty of Engineering, Prince of Songkla University, Songkhla, Thailand, as Professor. His current research interests include deep learning, microwave circuit design and microwave techniques for agricultural applications.

A Symmetrical Fractal-based Balanced Branch-Line Coupler for Simultaneous Low- and Mid-band 5G Frequencies Applications

Abdulkadir B. Shallah¹, Farid Zubir¹, Mohamad Kamal A. Rahim², and Zubaida Yusoff³

¹Wireless Communication Centre
Universiti Teknologi Malaysia, 81310 Johor Bahru, Johor, Malaysia
shallah@graduate.utm.my, faridzubir@utm.my

²Communication Engineering Department, Faculty of Electrical Engineering
Universiti Teknologi Malaysia, 81310 Johor Bahru, Johor, Malaysia
mdkamal@utm.my

³Faculty of Engineering
Multimedia University, Persiaran Multimedia, 63100 Cyberjaya, Selangor, Malaysia
zubaida@mmu.edu.my

Abstract – Symmetry is a key factor for Branch-Line Couplers (BLCs) in RF and microwave systems. This balanced approach evenly distributes power between two output ports, aiding impedance matching and reducing unwanted coupling and crosstalk, while increasing input-output isolation. Furthermore, the symmetrical design of BLCs ensures favorable return loss and phase balance, which are essential for phase-sensitive detectors and beamforming. This symmetry also guarantees consistent performance over a wide frequency range, making it suitable for broadband or multi-frequency applications. We present a compact BLC operating in two frequency bands, ideal for 5G sub-6 GHz applications. It uses T-shaped lines with folded lines and stubs in a Minkowski fractal shape, resulting in a size reduction of 90%. The design and simulation were performed using the CST Microwave Studio at 0.7 GHz and 3.5 GHz, achieving a new high frequency band ratio of 5. A prototype on Rogers RT5880 substrate ($\epsilon_r = 2.2, h = 0.787$ mm) was tested to validate the design's effectiveness, offering potential for modern wireless applications requiring versatile frequency band operation.

Index Terms – Balanced, Coupler, Fifth-generation, Fractal, Frequency ratio, Low-band, Mid-band, Minkowski, Simultaneous, Symmetrical.

I. INTRODUCTION

Recent advancements in technology and communication systems have spurred a growing demand for compact, multifrequency, and high-bandwidth devices to enhance circuit designs' efficiency and performance [1]. In the realm of microwave and millimeter wave frequen-

cies, maintaining symmetry in the design of microstrip couplers plays a crucial role in ensuring equal power distribution while minimizing undesirable coupling effects [2]. However, traditional BLC with four ports, including an input port, an isolated port, and two coupled ports with a 90° phase difference, no longer meet the requirements of modern device design trends, which emphasize the need for dual-band or multiple-band functionality [3].

Various methods have been proposed to achieve dual frequency operation in BLCs, including the introduction of stubs in T [4, 5] or π -shapes [6, 7] and coupling lines [8, 9] to convert single-band sections into dual-band counterparts. However, these approaches exhibit limitations such as large circuit sizes, small frequency ratios, complex structures, high insertion loss, and a restricted frequency range, making them unsuitable for lower 5G bands, such as 0.7 GHz and 3.5 GHz [10]. Recent research has reported dual-band BLCs with higher frequency ratios [11, 12], but their optimal performance is observed when the midpoint frequency is higher than 3 GHz.

To address the demands of lower sub-6 GHz 5G frequency bands with a wide frequency ratio, this paper introduces a compact and simple dual-band BLC design. It uses T-shaped technique with folded lines in the form of Minkowski fractal geometry (MFG) to achieve compact packing of transmission lines (TL), effectively reducing the overall size in comparison to traditional configurations. The paper presents analytical equations, design details, and prototype realization of this dual-band branch-line coupler (DB-BLC), showing excellent agreement between measured and simulated results at

frequencies below 4 GHz. In addition to 5G applications, the proposed BLC can be used in radar systems, where it can split incoming and outgoing signals between radar transmitters and receivers, facilitating tasks such as topography measurement, vegetation analysis, and weather monitoring [13].

II. DESIGN ANALYSIS OF THE DUAL-BAND STRUCTURE

A. Dual-band branch-line coupler

The traditional BLC's $\lambda/4$ -wave sections are transformed into dual-band equivalents by adding extra T or π stubs. In this work, we adopt the T-shaped TL approach for simplicity. Figures 1 (a) and (b) show the layout of a standard BLC and how the $\lambda/4$ -wave sections are converted into T-shaped segments. This design equates the ABCD matrix of the conventional $\lambda/4$ -wave TL to the ABCD matrix of the T-shaped segments as:

$$\begin{bmatrix} A_T & B_T \\ C_T & D_T \end{bmatrix} = [M_{se}] [M_{sh}] [M_{se}], \quad (1)$$

M_{se} and M_{sh} represent the ABCD matrices for the T-section's series and shunt elements, respectively.

And the ABCD matrix of the $\lambda/4$ -wave transmission line is given by:

$$\begin{bmatrix} A & B \\ C & D \end{bmatrix}_{\lambda/4} = \begin{bmatrix} 0 & \pm jZ_o \\ \pm j\frac{1}{Z_o} & 0 \end{bmatrix}, \quad (2)$$

Having Z_o as the characteristic impedance of the pri-

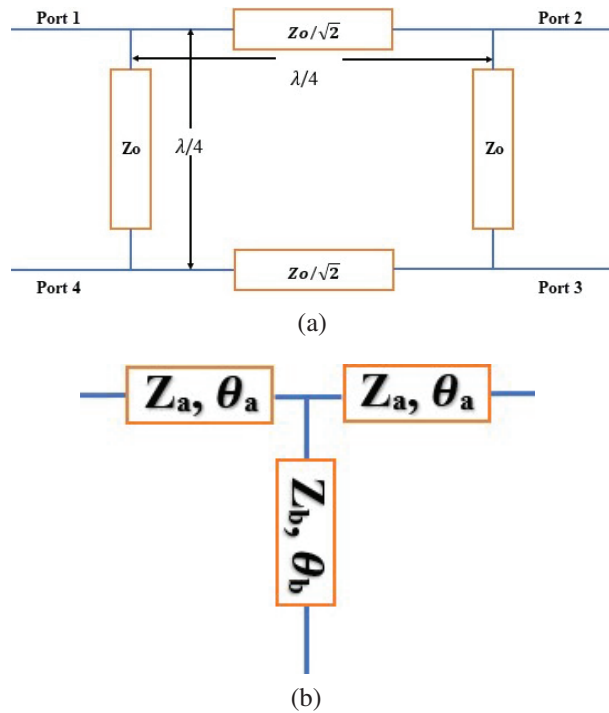
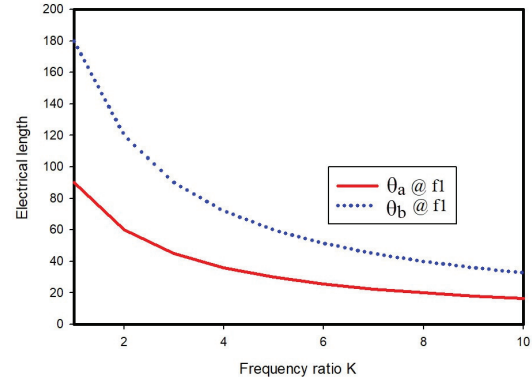


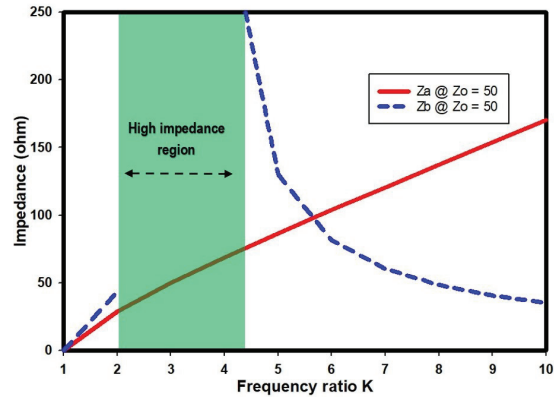
Fig. 1. The layout diagram of (a) conventional BLC and (b) proposed T-section.

mary branch line. The solutions to equations (1) and (2) results in:

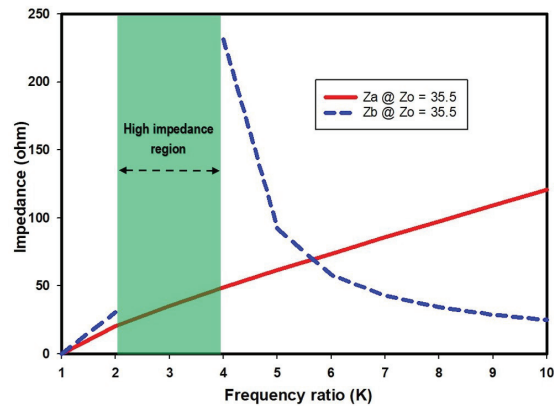
$$\tan \theta_b = 2 \times \left(\frac{Z_b}{Z_a} \right) \times \cot 2 \theta_a, \quad (3)$$



(a)



(b)



(c)

Fig. 2. The relationship between (a) the electrical lengths (θ_a, θ_b) and the frequency ratio K , (b) the relationship between the (Z_a, Z_b) when $Z_o = 35.35 \Omega$ and frequency ratio K , and (c) the relationship between (Z_a, Z_b) when $Z_o = 50 \Omega$ and the frequency ratio K .

$$Z_o = Z_a \times \tan \theta_a, \quad (4)$$

where θ_{af1} and θ_{af2} represent the electrical lengths of the lines at designed frequencies. Furthermore, the solution to equation (4) is obtained as:

$$p\pi = \theta_{af1} \pm \theta_{af2}, \quad p = 1, 2, 3, \dots, \quad (5)$$

$$\frac{\theta_{af2}}{\theta_{af1}} = \frac{f_2}{f_1} = K. \quad (6)$$

Therefore, from equations (3) and (5), we have:

$$\theta_{af1} = \frac{\pi}{K+1}, \quad \theta_{af2} = K \times \theta_{af1}, \quad (7a)$$

$$\theta_{bf1} = \frac{2\pi}{K+1}, \quad \theta_{bf2} = K \times \theta_{bf1}. \quad (7b)$$

The values for the line impedances can be deduced using the following equations:

$$Z_a = \frac{Z_o}{\tan \theta_{af1}}, \quad (8a)$$

$$Z_b = \frac{1}{2} \times Z_a \times \tan^2 2\theta_{af1}. \quad (8b)$$

By using equations (1) to (8), we can understand how electrical lengths change with the frequency ratio K , as shown in Fig. 2 (a). We also explore the behavior of characteristic impedances, denoted Z_a and Z_b , in our design. These operate at two different impedance values: 50 Ω and 35.35 Ω . Figures 2 (b) and (c) illustrate how these impedance values change with the frequency ratio K .

The practical impedance range for (Z_a, Z_b) is 22.5 Ω to 180 Ω , as shown in Figs. 2 (b) and (c). This limits frequency ratios K to 1.93-2.33 and 3.5-8.7. Achieving ratios between 2.34 and 3.49 is challenging due to high impedance.

Alternatively, in [11, 12], coupled lines achieve 2.34-3.49 ratios, but suffer high insertion loss [14]. T-sections in BLC [15–17] have limited ratios. For example, [15] and [16] achieve 2.22 and 2.42 ratios at 0.9/2 GHz and 2.4/5.2 GHz. The highest ratio in [17] is 4.8.

Our work achieves a ratio of 8.7, offering greater versatility for dual-band BLCs, as shown in Figs. 2 (a-c), Fig. 3 displays lumped elements in DB-BLC 1, designed using Table 1 parameters.

While DB-BLC 1 covers a wide frequency range, it is bulky at (162.58 mm \times 161.31 mm). To reduce size, we fractalize the structure with sharp-edged chamfered bends to minimize capacitive effects [18].

Table 1: The dimensions based on the theoretical parameters

Parameter	Z (Ω)	Width (mm)	Length (mm)
L_a	61.25	1.77	52.08
L_b	86.60	0.95	54.37
L_{s1}	91.88	0.90	51.70
L_{s2}	129.90	0.45	54.30

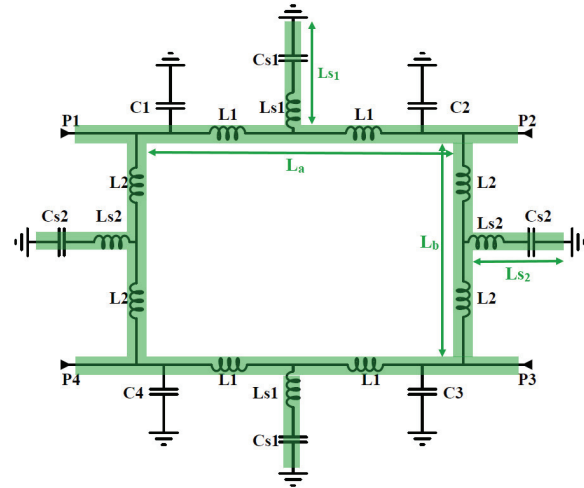


Fig. 3. The lumped elements representation superimposed with the layout of the DB-BLC 1.

B. Proposed miniaturized (DB-BLC 2)

To simplify the structure, we have modified the BLC series, shunt segments, and their stubs to resemble the first iteration MFG design. This change maintains device symmetry for reliable power distribution, strong isolation, consistent frequency response, low return loss, and phase balance, all vital for proper functionality.

The MFG implementation is based on three key parameters, as shown in Fig. 4: L for generator length, L_3 for the indentation width, and L_2 for the depth of the fractal or indentation. Figure 4 (a) illustrates the evolution from the generator to the first Minkowski fractal iteration. We use the one-third ratio, common in creating famous fractal curves such as the Koch and Cantor geometries [19], which is crucial.

The dimension D values follow logarithmic functions defined in equation (9). k denotes the number of segments in the geometry, and r signifies the segments divided during each iteration after initially dividing the geometry into k segments.

$$D = \frac{\log k}{\log r}. \quad (9)$$

Equation (9) yields a Minkowski fractal dimension of 1.465, which quantifies a fractal curve's space-filling ability. In particular, not all fractal curves are suitable for use in BLC design, although some have found success in antenna design [20]. This distinction arises from the different input-output coupling requirements in the BLC design.

To enhance the coupling and establish a practical fractal dimension range, we adopt a first-iteration geometry. We replace the standard 1/3 ratio for generating diverse fractal curves with an arbitrary ratio. Figure 4 (a)

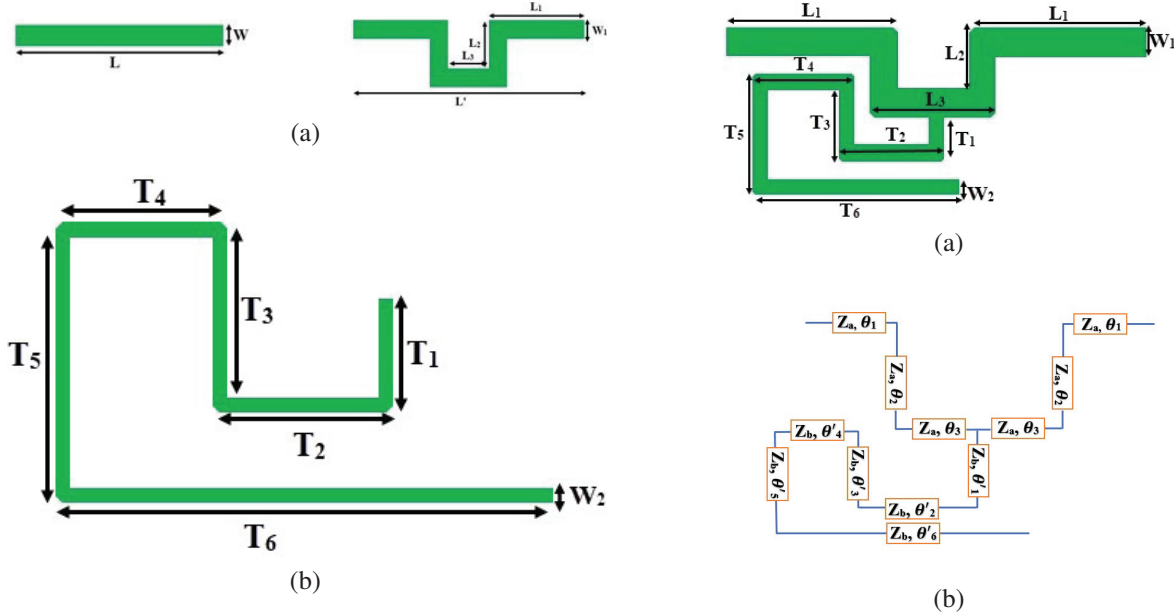


Fig. 4. The layout representations of (a) initiator and fractalized main line and (b) stub.

shows the initial iteration with five segments, two horizontal sections ($2 \times (L_1)$) considerably longer, and three segments approximately $2 \times (L_2)$ and L_3 in length.

The characteristic impedances for main-series and shunt TLs remain unchanged to maintain desired dimensions. However, equations (7a) and (7b) undergo adjustments. Electrical lengths for main lines (θ_1 - θ_3) and stubs (θ'_1 - θ'_6) in Fig. 4 (b) are calculated based on the chosen arbitrary ratio, and the total length is given in equation (10).

The optimized dimensions for the proposed horizontal and vertical line sections are summarized in Table 2:

$$\theta_{xf1(a,b)} = \theta_T = 2\theta_1 + 2\theta_2 + \theta_3. \quad (10)$$

Figures 5 (a) and (b) display a compact 35.35Ω horizontal TL for efficient signal transmission at 0.7 GHz and 3.5 GHz. Our aim is minimal signal loss (low S_{21}) and minimal reflection ($S_{11} < -10$ dB) to optimize power transfer.

Figures 5 (c) and (d) show the TL's magnitude and phase responses at 0.7 GHz and 3.5 GHz, providing a

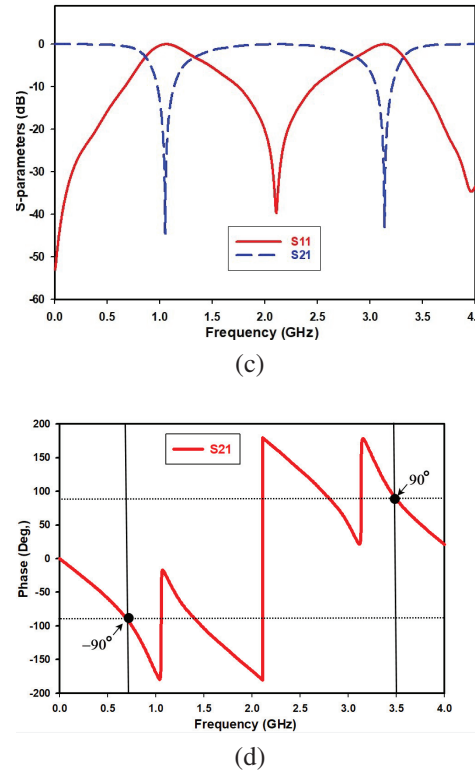


Fig. 5. The representations of (a) 35.35Ω horizontal section, (b) equivalent circuit, (c) S-parameter response, and (d) phase response of the line.

comprehensive view of signal behavior. In particular, Fig. 5 (d) achieves phase control with -90° and $+90^\circ$ at 0.7 GHz, and 3.5 GHz.

Figures 6 (a) and (b) detail the 50Ω vertical TL design and structure, revealing its physical arrangement.

Table 2: The optimized geometrical dimensions

Section	Series Line	Shunt Line	Elect., Length	Series Stub	Shunt Stub
L_1 (mm)	15.51	16.64	θ_1	19.20°	17.50°
L_2 (mm)	3.87	4.20	θ_2	5.20°	6.40°
L_3 (mm)	7.80	8.32	θ_3	9.60°	6.70°
T_1 (mm)	3.66	4.50	θ'_1	4.10°	4.95°
T_2 (mm)	7.25	6.00	θ'_2	8.11°	6.60°
T_3 (mm)	6.75	7.00	θ'_3	7.50°	7.70°
T_4 (mm)	7.25	9.00	θ'_4	8.11°	9.90°
T_5 (mm)	9.55	9.00	θ'_5	10.7°	9.90°
T_6 (mm)	17.25	18.00	θ'_6	19.3°	19.8°
W_1 (mm)	1.77	0.95	—	—	—
W_2 (mm)	0.85	0.55	—	—	—

On the contrary, Figs. 6 (c) and (d) analyze the vertical TL's S parameters and phase response, offering insights into system performance.

These figures highlight the vertical TL's impressive capabilities, ensuring effective signal transmission

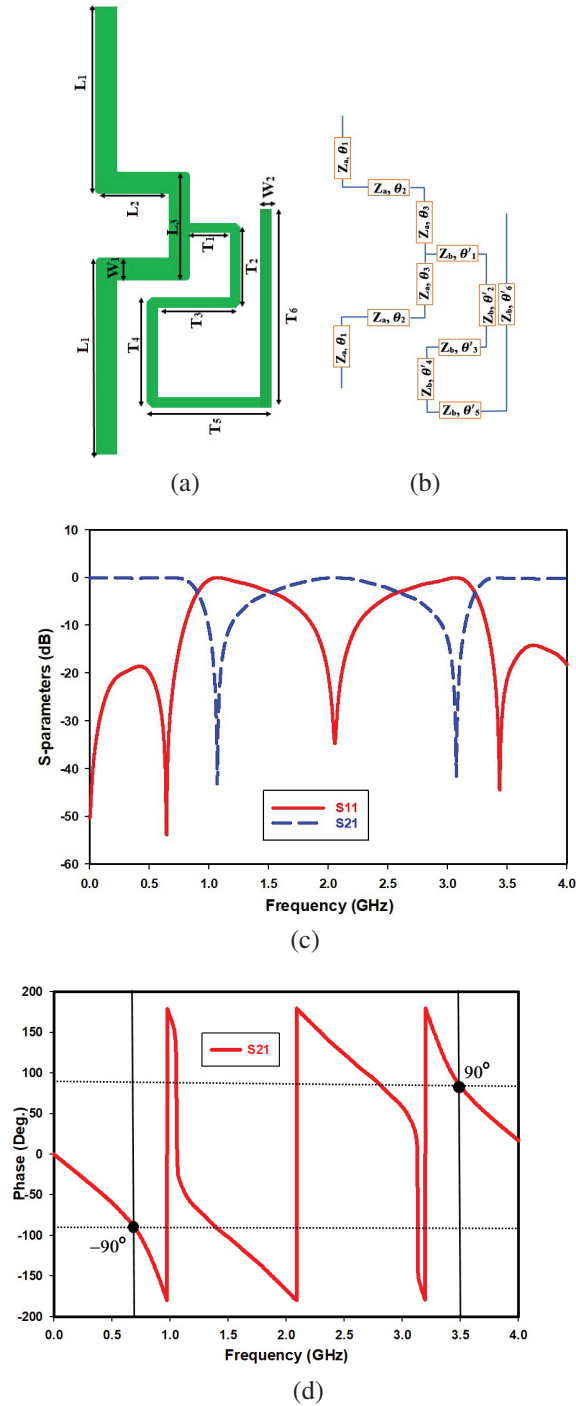


Fig. 6. Representations of (a) 50 Ω vertical section, (b) equivalent circuit, (c) S-parameter response, and (d) phase response of the line.

at 0.7 GHz and 3.5 GHz and precise phase shifts of -90° and $+90^\circ$ at these frequencies. These results affirm the vertical TL's reliability and significance in the system.

III. SIMULATIONS, FABRICATION, AND MEASUREMENTS

DB-BLC 1 and DB-BLC 2 were created for 5G below 6 GHz frequencies (specifically, 0.7 GHz and 3.5 GHz) using CST Microwave Studio software. DB-BLC 2, shown in Fig. 7, has a unique symmetrical design achieved by combining the TLs from Figs. 5 and 6. The gaps shown from the diagram are only for the purpose of demonstrating integration and do not reflect the actual configuration. It was developed on an RT/Duroid 5880 substrate, 0.787 mm thick, with a permittivity of 2.2 and a loss tangent of 0.0009.

To realize the prototype shown in Fig. 8 (a), the photoetching technique was used and SMA connectors were used for measurements. The S parameters of the prototype were measured using a Rohde & Schwarz

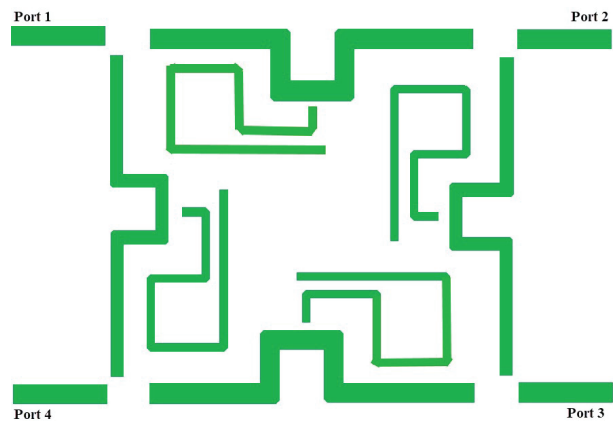
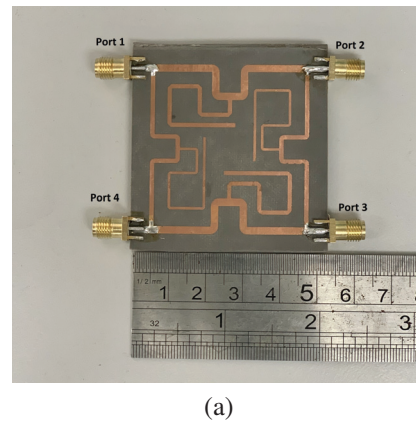


Fig. 7. The diagram showing the assembly process of the Minkowski-shaped DB-BLC 2.



(a)

Fig. 8. Continued



Fig. 8. The structure of the fabricated prototype for BLC-2 (a) with SMA connectors and (b) with VNA during S-parameter measurement.

ZNB 40 vector network analyzer (VNA), as illustrated in Fig. 8 (b).

IV. RESULTS AND DISCUSSION

Figures 9 (a) and (b) visually depict the current density distribution in the DB-BLC 2 structure at two critical frequencies, 0.7 GHz and 3.5 GHz. Figure 9 illustrates the equal division of the input signal between Port-2 and Port-3, with Port-1 as an input port, ensuring symmetric power distribution. This balance enhances device efficiency. Additionally, Port-4 remains isolated from the input signal, as evident in the figures, preventing unwanted signal leakage or interference at specified frequencies.

Figure 10 provides the (S- parameters), providing information on the interaction and transmission of the

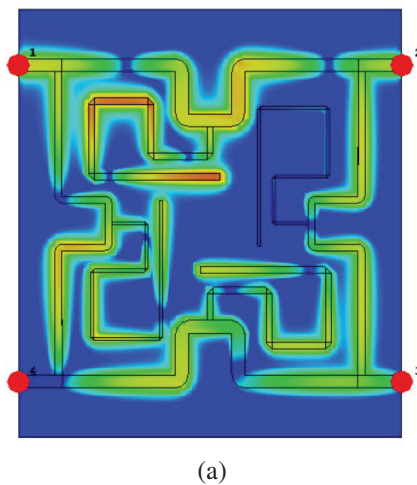


Fig. 9. Continued

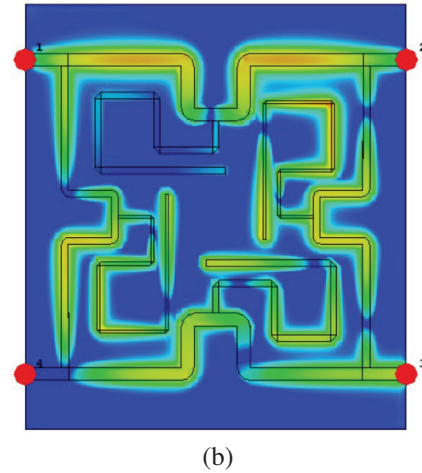


Fig. 9. The current density distribution of the proposed DB-BLC 2 with Port-1 as an input port (a) at 0.7 GHz and (b) at 3.5 GHz.

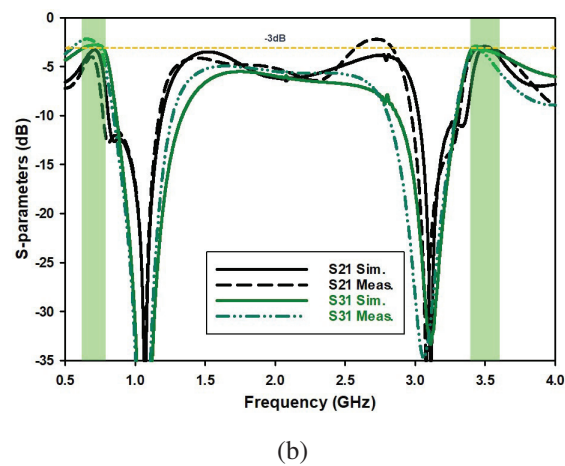
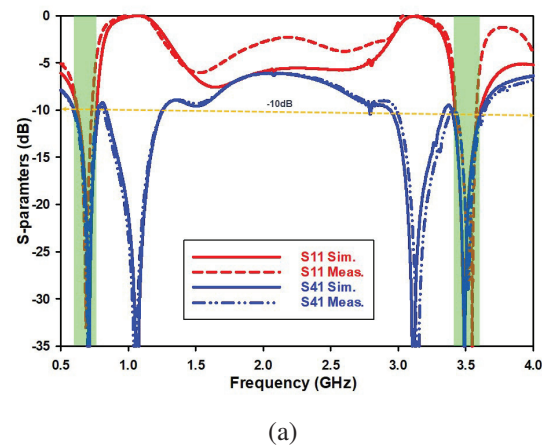


Fig. 10. The S-parameters results analysis of DB-BLC 2 (a) S_{11} and S_{41} simulated and measured and (b) S_{21} and S_{31} simulated and measured.

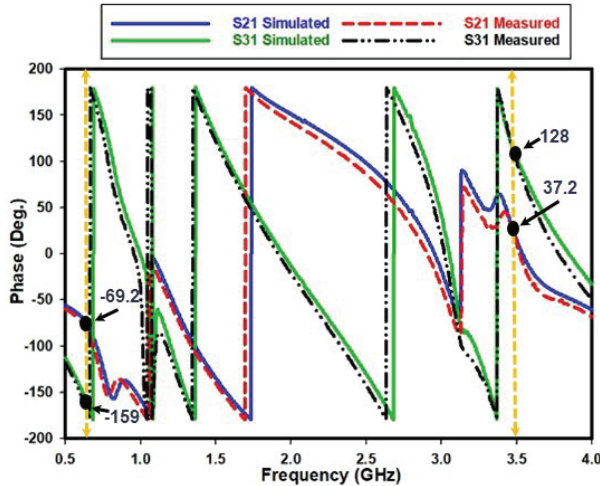


Fig. 11. The overlapped phase response of the proposed DB-BLC 2.

signal. Meanwhile, Fig. 11 presents the phase response across coupled and through ports, crucial for understanding phase shift characteristics in various applications.

Notably, miniaturization via MFG caused slight resonance frequency shifts and reduced return loss values, optimizing the design for desired frequency bands and improved performance. Figures 10 and 11 display S-parameter and phase responses, confirming the functionality of the BLC within the sub-6 GHz 5G dual frequency bands (0.7 GHz and 3.5 GHz). In particular, both S_{11} and S_{41} in Fig. 10 (a) exhibit values below -25 dB in these frequency bands. To ensure a balanced power distribution between the Port-2 and Port-3 out-

puts, both S_{21} and S_{31} should be around -3 dB. Consequently, the proposed design in Fig. 10 (b) shows values of -3.1 dB and -3.09 dB at 0.7 GHz and -2.98 dB and -3.21 dB at 3.5 GHz. Additionally, optimal power distribution requires a 90° phase difference between output ports Port-2 and Port-3. Figure 11 reveals phase differences ($\angle S_{31} - \angle S_{21}$) of -89.8° at 0.7 GHz and 90.6° at 3.5 GHz, translating to phase errors of 0.2° and 0.6° , respectively.

Table 3 provides a performance comparison between simulated DB-BLC 1, DB-BLC 2, and measured DB-BLC 2.

In the frequency range of 0.7 GHz to 3.5 GHz, DB-BLC 2 performed exceptionally well. The measured return loss (S_{11}) and the isolation loss (S_{41}) were better than -10 dB. Figure 10 illustrates that, at 0.7 GHz, the measured insertion loss (S_{21}) and coupling loss (S_{31}) were -3.61 dB and -2.65 dB, respectively, while at 3.5 GHz, they were -2.89 dB and -3.34 dB. The maximum insertion loss and coupling loss were 0.61 dB and 0.36 dB, respectively, closely approaching the standard -3 dB value.

The phase differences between the output Port-2 and Port-3 for DB-BLC 2 were measured at -88.9° and 91.2° , respectively, with a maximum measured phase error of 1.2° compared to the simulated 0.8° . It's worth noting that fabrication errors and dielectric losses may influence the measured phase error and other performance parameters. However, the proposed design exhibited good agreement with the overall simulated and measured results.

Table 4 provides a comparative assessment of DB-BLC 2 in the same frequency range as previous designs. Analysis shows that our design excels in simplicity, compactness, and a wider frequency band ratio. On the contrary, the closest predecessor achieves only a ratio of 4, while other designs require larger sizes, lower K values, or more complex structures. Notably, [29] and [21] achieve smaller dimensions but with a limited band ratio. In summary, these findings show the suitability of the proposed BLC design for sub-6 GHz 5G applications.

Table 3: Performance comparison between simulated DB-BLC 1, DB-BLC 2, and measured DB-BLC 2

Parameter	DB-BLC 1 (Sim)	DB-BLC 2 (Sim)	DB-BLC 2 (Mea)
Freq., (GHz)	0.7/3.5	0.7/3.5	0.7/3.5
S_{11} (dB)	-29.7/33.4	-30.4/-31.2	-29.0/-26.1
S_{21} (dB)	-3.31/-3.23	-3.10/-2.98	-3.61/-2.89
S_{31} (dB)	-2.86/-3.11	-3.09/-3.21	-2.65/-3.34
S_{41} (dB)	-31.4/-29.7	-31.8/-28.9	-29.1/-26.4
Phase diff., ($^\circ$)	-91.4/89.1	-89.8/90.6	-88.9/91.2

Table 4: Performance comparison with other related published works from the literature

Ref./Date	f_1/f_2 (GHz)	Ratio (K)	Size (mm)	$ S_{11} $ (dB)	$ S_{21} $ (dB)	$ S_{31} $ (dB)	$ S_{41} $ (dB)	Phase Error ($^\circ$)	Ampl. Error (dB)
[17]/2016	1/4	4	65×51	-/-	-3.28/-3.2	-3.43/ -3.37	-/-	-/-	-/-
[21]/2016	0.87/1.79	2.05	31×31	-26/-21.6	-3.3/-3.09	-3.67/-3.9	-34/-19.9	± 5	± 1
[22]/2018	0.82/2	2.43	55×32	-21/-13	-/-	-/-	-24/-14	-	1.4
[23]/2018	0.9/2.4	2.67	64×83	-27/-26	-3.47/ -3.56	-3.41/ -3.78	-24.5/-23.3	± 5	± 0.5
[24]/2019	0.75/1.32	1.76	-	>-14	-3.35/-4.0	-3.74/ -4.1	>-14	± 4	± 0.65
[25]/2021	0.9/1.8	2	124×60.4	-	-/-	-/-	-	-	-
[26]/2022	0.9/2.45	2.72	99×46	-20	-3.66/ -3.72	-3.42/ -3.53	-20	± 5	1
[27]/2022	1/2.5	2.5	68×65	-15	-2.9/-2.8	-3/-3.5	-20	± 2.7	-
[28]/2023	0.9/2.0	2.22	99.06 ×12.96	-26.8/ -35.6	-3.5/-3.4	-3.1/-3.3	-23.4/ -27.2	-	-
This work	0.7/3.5	5	54×48	-29.0/ -26.1	-3.61/ -2.89	-2.65/ -3.34	-29.1/ -26.4	1.2	0.61

V. CONCLUSIONS

In this paper, a miniaturized DB-BLC with an improved frequency band ratio is reported. The BLC's traditional transmission line (TL) is transformed into a T-shaped TL on both arms using ABCD-matrix analysis to attain dual-band properties. Symmetry is a fundamental design parameter that contributes to the effectiveness and efficiency of these components in communication, radar, and other high-frequency systems. By utilizing this fractal geometry, the designed branch-line coupler is further miniaturized achieving a 90% size reduction while maintaining its functionality.

This design is believed to be the first compact and low-profile DB-BLC with a large frequency ratio for lower frequency bands of 0.7 GHz and 3.5 GHz. The simulated and verified results show good agreement. Importantly, this proposed structure holds promise applications in sub-6 GHz 5G applications, where its compactness and dual-band capabilities can offer valuable advantages.

ACKNOWLEDGMENT

This work was supported in part by the Higher Institution Centre of Excellence (HICOE), Ministry of Higher Education Malaysia through the Wireless Communication Centre (WCC), Universiti Teknologi Malaysia, under Grant R.J090301.7823.4J610; in part by Universiti Teknologi Malaysia (UTM) under UTM Encouragement Research under Grant 20J65; in part by UTMShine Batch 6 under Grant 09G97; and in part by the Faculty of Engineering, Multimedia University, Cyberjaya (MMU).

REFERENCES

- [1] K.-K. Cheng and F.-L. Wong, "A novel approach to the design and implementation of dual-band compact planar 90°/spl deg/branch-line coupler," *IEEE Transactions on Microwave Theory and Techniques*, vol. 52, no. 11, pp. 2458-2463, 2004.
- [2] S. I. Yahya, F. Zubir, L. Nouri, F. Hazzazi, Z. Yusoff, M. A. Chaudhary, M. Assaad, A. Rezaei, and B. Nguyen Le, "A balanced symmetrical branch-line microstrip coupler for 5G applications," *Symmetry*, vol. 15, no. 8, p. 1598, 2023.
- [3] R. K. Barik, Q. S. Cheng, N. C. Pradhan, and K. S. Subramanian, "A miniaturized quad-band branch-line crossover for GSM/WiFi/5G/WLAN applications," *AEU-International Journal of Electronics and Communications*, vol. 134, p. 153611, 2021.
- [4] N. Zheng, L. Zhou, and W.-Y. Yin, "A novel dual-band Π -shaped branch-line coupler with stepped-impedance stubs," *Progress In Electromagnetics Research Letters*, vol. 25, pp. 11-20, 2011.
- [5] P. Liu and D. Yang, "A dual-band compact branch line coupler based on Γ -shaped transformer," in *2016 17th International Conference on Electronic Packaging Technology (ICEPT)*, pp. 1476-1479, IEEE, 2016.
- [6] H. Zhang, W. Kang, and W. Wu, "A novel compact dual-band branch-line coupler with cross-shaped stubs," in *2016 IEEE International Conference on Ubiquitous Wireless Broadband (ICUWB)*, pp. 1-4, IEEE, 2016.
- [7] W. Feng, X. Duan, Y. Shi, X. Y. Zhou, and W. Che, "Dual-band branch-line couplers with short/open-ended stubs," *IEEE Transactions on Circuits and Systems II: Express Briefs*, vol. 67, no. 11, pp. 2497-2501, 2020.
- [8] J.-H. Yu, J.-C. Cheng, and Y.-H. Pang, "Design of a dual-band miniaturized 90 branch-line coupler with coupled lines," in *Asia-Pacific Microwave Conference 2011*, pp. 21-24, IEEE, 2011.
- [9] C.-H. Yu and Y.-H. Pang, "Dual-band unequal-power quadrature branch-line coupler with coupled lines," *IEEE Microwave and Wireless Components Letters*, vol. 23, no. 1, pp. 10-12, 2012.
- [10] A. B. Shallah, F. Zubir, M. K. A. Rahim, H. A. Majid, U. U. Sheikh, N. A. Murad, and Z. Yusoff, "Recent developments of butler matrix from components design evolution to system integration for 5g beamforming applications: A survey," *IEEE Access*, vol. 10, pp. 88434-88456, 2022.
- [11] A. M. Zaidi, M. T. Beg, B. K. Kanaujia, K. Srivastava, and K. Rambabu, "A dual band branch line coupler with wide frequency ratio," *IEEE Access*, vol. 7, pp. 25046-25052, 2019.
- [12] L. Xia, J.-L. Li, B. A. Twumasi, P. Liu, and S.-S. Gao, "Planar dual-band branch-line coupler with large frequency ratio," *IEEE Access*, vol. 8, pp. 33188-33195, 2020.
- [13] F. A. Ghaffar, T. Y. Al-Naffouri, M. Mobeen, K. N. Salama, and A. Shamim, "A compact QPSK modulator with low amplitude and phase imbalance for remote sensing applications," *Institute of Electrical and Electronics Engineers*, 2012.
- [14] S. Roshani, S. I. Yahya, S. Roshani, and M. Rostami, "Design and fabrication of a compact branch-line coupler using resonators with wide harmonics suppression band," *Electronics*, vol. 11, no. 5, p. 793, 2022.
- [15] H. Zhang and K. J. Chen, "A stub tapped branch-line coupler for dual-band operations," *IEEE Microwave and Wireless Components Letters*, vol. 17, no. 2, pp. 106-108, 2007.
- [16] K.-S. Chin, K.-M. Lin, Y.-H. Wei, T.-H. Tseng, and Y.-J. Yang, "Compact dual-band branch-line and rat-race couplers with stepped-impedance-stub lines," *IEEE Transactions on Microwave Theory*

- and Techniques*, vol. 58, no. 5, pp. 1213-1221, 2010.
- [17] M. A. Maktoomi, M. S. Hashmi, and F. M. Ghanouchi, "Systematic design technique for dual-band branch-line coupler using T-and Pi-networks and their application in novel wideband-ratio crossover," *IEEE Transactions on Components, Packaging and Manufacturing Technology*, vol. 6, no. 5, pp. 784-795, 2016.
- [18] A. C. Das, L. Murmu, and S. Dwari, "A compact branch-line coupler using folded microstrip lines," in *2013 International Conference on Microwave and Photonics (ICMAP)*, pp. 1-3, IEEE, 2013.
- [19] K. Falconer, J. Fraser, and X. Jin, "Sixty years of fractal projections," in *Fractal Geometry and Stochastics V*, pp. 3-25, Springer, 2015.
- [20] M. Kumar and V. Nath, "Introducing multiband and wideband microstrip patch antennas using fractal geometries: Development in last decade," *Wireless Personal Communications*, vol. 98, pp. 2079-2105, 2018.
- [21] C. Gai, Y.-C. Jiao, and Y.-L. Zhao, "Compact dual-band branch-line coupler with dual transmission lines," *IEEE Microwave and Wireless Components Letters*, vol. 26, no. 5, pp. 325-327, 2016.
- [22] D. A. Letavin, "Compact dual-frequency microstrip branch-line coupler using artificial transmission lines," in *2018 19th International Conference of Young Specialists on Micro/Nanotechnologies and Electron Devices (EDM)*, pp. 185-188, IEEE, 2018.
- [23] A. M. Zaidi, S. A. Imam, B. Kanaujia, and K. Rambabu, "A new equal power quadrature branch line coupler for dual-band applications," *Progress In Electromagnetics Research Letters*, vol. 74, pp. 61-67, 2018.
- [24] W. Feng, M. Xun, Y. Zhao, and W. Che, "Dual-band branch line coupler with high isolation isolation using loaded coupled lines," in *2018 International Applied Computational Electromagnetics Society Symposium-China (ACES)*, pp. 1-2, IEEE, 2018.
- [25] R. Islam, A. I. Omi, M. A. Maktoomi, C. Zakzewski, and P. Sekhar, "A new coupled-line based dual-band branch-line coupler with port-extensions," *Progress in Electromagnetics Research M*, vol. 105, no. 2021, 2021.
- [26] H. Naseri, P. PourMohammadi, Z. Mousavirazi, A. Iqbal, G. A. Vandenbosch, and T. A. Denidni, "A low-profile dual-band hybrid coupler with flexible frequency band ratio," *Progress in Electromagnetics Research Letters*, vol. 107, pp. 119-124, 2022.
- [27] H. Chang, T. Lim, K. C. Dimitrov, and Y. Lee, "Dual-band branch-line coupler based on crossed lines for arbitrary power-split ratios," *Sensors*, vol. 22, no. 15, p. 5527, 2022.
- [28] X.-Y. Zhang and J.-C. Lee, "A dual-band branch-line coupler with ultra-wideband harmonic suppression," *Journal of Electromagnetic Engineering and Science*, vol. 23, no. 1, pp. 57-62, 2023.
- [29] S. Singh, R. P. Yadav, and A. Jain, "Miniaturized dual-band branch-line coupler with folded stubs," in *2019 IEEE 5th International Conference for Convergence in Technology (I2CT)*, pp. 1-4, IEEE, 2019.



Abdulkadir Bello Shallah (Member, IEEE) was born in Gwandu, Kebbi, Nigeria, in 1984. He received the B.Eng. Degree in electrical and electronics engineering from Bayero University, Kano, in 2014, and the M.Eng. degree in electronics and telecommunications from Universiti Teknologi Malaysia, in 2017, where he is currently pursuing a Ph.D. degree from the School of Electrical Engineering.

He has been a Lecturer with the Electrical and Electronics Engineering Department, Faculty of Engineering, Kebbi State University of Science and Technology, Aliero, Kebbi. His research interests include RF and microwave devices, reflectarray antennas, beamforming networks, and metamaterials.



Farid Zubir (Member, IEEE) received the B.Eng. degree in electrical (majoring in telecommunication) and the M.Eng. RF and microwave degree from Universiti Teknologi Malaysia (UTM), in 2008 and 2010, respectively, and Ph.D. degree from the University of Birmingham, UK, in 2016, for research into direct integration of power amplifiers with antennas in microwave transmitters.

He is currently an Assistant Professor and a Research Fellow with the Department of Communication Engineering, School of Electrical Engineering, and the Wireless Communication Centre, UTM, respectively. He was an Honorary Postdoctoral Research Fellow with The University of British Columbia (UBCO), Okanagan, BC, Canada, from September 2019 to August 2021, where he conducted research into highly efficient and linear amplification power amplifier topology for wireless power systems. His research interests include the area of RF and microwave technologies, including linearization and high-efficiency techniques for PAs, beamforming networks, planar array antenna, dielectric resonator antenna (DRA) and active integrated antenna (AIA).

**Mohamad Kamal A. Rahim**

(Senior Member, IEEE) was born in Alor Setar, Malaysia, in 1964. He received the B.Eng. degree in electrical and electronic engineering from the University of Strathclyde, UK, in 1987, the Master's degree in engineering from the University of New South Wales, Australia, in 1992, and the Ph.D. degree in wideband active antenna from the University of Birmingham, UK, in 2003. From 1992 to 1999, he was a Lecturer with the Faculty of Electrical Engineering, Universiti Teknologi Malaysia, where he was a Senior Lecturer with the Department of Communication Engineering, from 2005 to 2007, and is currently a Professor.

His research interests include the design of active and passive antennas, dielectric resonator antennas, microstrip antennas, reflectarray antennas, electromagnetic bandgap, artificial magnetic conductors, left-handed metamaterials, and computer-aided design for antennas.

**Zubaida Yusoff** (Senior Member,

IEEE) received the B.Sc. degree (cum laude) in electrical and computer engineering and the M.Sc. degree in electrical engineering from The Ohio State University, USA, in 2000 and 2002, respectively, and the Ph.D. degree from Cardiff University, Wales, UK, in 2012. She worked with Telekom Malaysia International Network Operation in 2002, before joining Multimedia University, Malaysia, in 2004, where she currently holds the position of a Senior Lecturer at the Faculty of Engineering. She has authored and coauthored more than 50 journals and conference papers.

Her teaching and research focus in the area of power amplifier design, antenna, 5G communications, and analog/mixed signal RF circuit design. She has presented technical papers at conferences nationally and internationally. One of her conference papers has received the "Honorable Mention" for the Student Paper Competition at the International Microwave Symposium, USA, in 2011.

Single-mode Condition and Bending Loss Analysis of Ultrafast Laser-inscribed Mid-infrared Waveguides in GeAsSe Chalcogenide Glass

Takashi Yasui

Faculty of Engineering
Kitami Institute of Technology, Kitami-shi, Hokkaido, 090-8507, Japan
yasui@mail.kitami-it.ac.jp

Abstract – In this study, single-mode conditions and bending losses of optical waveguides based on Ge₃₃As₁₂Se₅₅ chalcogenide glass, commercially known as IG2, for astrophotonic devices in the mid-infrared spectral range are numerically analyzed. The scalar finite-element method was used to analyze single-mode conditions. For the bending-loss analysis, equivalent straight waveguides of bent waveguides were analyzed using the two-dimensional finite-difference beam-propagation method. The results revealed design rules for astrophotonic optical integrated circuits in the mid-infrared spectral range.

Index Terms – Astrophotonics, beam-propagation method, bending-loss analysis, finite-element method, optical waveguide, single-mode condition.

I. INTRODUCTION

Optical integrated circuits (OICs), which are vital in current optical telecommunication systems, are being widely used in astrophysics to meet the astronomers' ever-increasing demand for higher angular, spectral, and temporal resolutions over a broad wavelength range among astronomers. Astronomers hope to understand the formation of planets, stars, and galaxies to characterize the atmospheres of exoplanets in habitable zones and unravel the physics of black holes. The application of the OICs in astronomy is referred to as astrophotonics. The OIC-based solutions have advantages in terms of size, weight, and cost compared to solutions based on conventional free-space optics. In addition, they can realize functionalities that are difficult or impossible to achieve using conventional solutions. Astrophotonics will be important in the new era of extremely large 30-m class telescopes [1, 2].

Various astrophotonic instruments have been developed [3–15]. Most of them are operated in the near-infrared (IR) spectral range owing to the availability of technologies in the field of optical telecommunication. However, astrophotonic instruments operating in

the mid-IR spectral range have also been considered for the direct detection and characterization of exo-earths. Spectral features in the mid-IR range offer signatures of important chemicals in habitable zones such as water, ozone, and carbon dioxide [16, 17].

Chalcogenide glasses are promising materials for mid-IR OICs because of their broad transparency ranges. In addition, the ultrafast laser inscription (ULI) technique, which generates permanent refractive index changes, is a highly cost-effective and convenient method for inscribing waveguides in chalcogenide glasses [5, 11–15, 18]. The change in the refractive index due to ULI can be controlled by the pulse energy.

Ge₃₃As₁₂Se₅₅ chalcogenide glass, also known as IG2 [19], is a well-established chalcogenide composition commonly used in mid-IR applications [14, 15, 20]. Because IG2 glass is transparent from 1 μm up to 12 μm of the wavelength range [15] that covers the two atmospheric transmission windows (3-5 and 8-12 μm), IG2 glass is suitable for astrophotonic OICs operated in mid-IR. Ultrafast laser-inscribed IG2 glass waveguides for mid-IR OICs, such as directional couplers with rectangular waveguides operating at a single wavelength, have been fabricated and demonstrated. Measured coupling ratio of a fabricated coupler was compared to the ones by an analytical and a numerical method [14]. Although characterizations such as the single-mode operation of the rectangular waveguides have been experimentally performed at a single wavelength, their single-mode condition has been theoretically analyzed only for square waveguides at a single wavelength [15].

Bent waveguides are important building blocks of OICs. Although bent waveguides with small radii are vital for realizing compact OICs, the losses that occur in bent waveguides increase as the bending radii decrease. A smaller bend loss is required for astrophotonic OICs because astronomical observation programs are inherently photon starved. However, to the best of our knowledge, the bending losses of ultrafast laser-inscribed IG2 glass waveguides have not been experimentally or theoretically characterized.

In this study, the analysis of single-mode conditions using the scalar finite-element method (FEM) [21] and bending-loss analysis using the two-dimensional finite-difference beam-propagation method (FD-BPM) [22] were carried out for IG2-glass-based waveguides. These results provide fundamental information for designing high-performance astrophotonic devices based on IG2 glass in the mid-IR spectral range.

II. CONFIGURATION AND NUMERICAL METHODS

A. Bent waveguides

We consider a bent waveguide shown in Fig. 1. The bent waveguide consists of a rectangular core, whose width, thickness, and refractive index are, respectively, w , t , and n_{core} . The core is surrounded by a cladding material with a refractive index of n_{clad} . It is assumed that two uniform straight waveguides, whose cores and claddings are identical to the ones of the bent waveguide, are connected to the input and output of the bent waveguide.

In this study, we assumed that the cladding material was IG2 glass, and that the core was fabricated using the ULI technique. The refractive index of the cladding, n_{clad} , is expressed as follows[19]:

$$n_{clad}^2(\lambda) = A + \frac{B_1 \lambda^2}{\lambda^2 - C_1^2} + \frac{B_2 \lambda^2}{\lambda^2 - C_2^2}, \quad (1)$$

where $A = 3.3408$, $B_1 = 2.9626$, $C_1 = 0.3600$, $B_2 = 0.8298$, and $C_2 = 35.0011$. The refractive index of the core is expressed as $n_{core} = n_{clad} + \Delta n$, where Δn denotes the refractive-index change by the ULI, whose range covers 0.008-0.02[15]. In this study, we considered the waveguides operated in E^x modes.

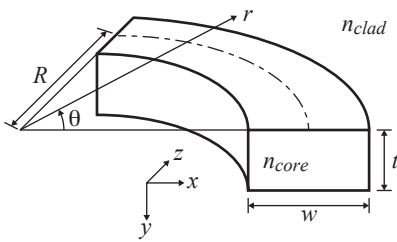


Fig. 1. Three-dimensional view of a bent waveguide, whose core is surrounded by a cladding material.

B. Brief review of FEM

In this section, we briefly review the scalar FEM. The scalar FEM is applied to analyze the single-mode condition of the straight waveguides connected to the bent waveguide. We note that a single cross-section of the bent waveguide is necessary for the analysis. Suppose the cross-section is placed on the xy -plane. Under a

scalar wave approximation, the following wave equation is derived from the Maxwell's equations:

$$p_F \frac{\partial^2 \Psi}{\partial x^2} + p_F \frac{\partial^2 \Psi}{\partial y^2} + q_F k_0^2 \Psi - p_F \beta^2 \Psi = 0, \quad (2)$$

where $\Psi = E_x$, $p_F = 1$, $q_F = n^2(x, y)$ for E^x modes, $\Psi = H_x$, $p_F = 1/n^2(x, y)$, $q_F = 1$ for E^y modes, and $n(x, y)$ denotes the cross-sectional refractive-index distribution.

After dividing the cross-section by the second-order triangular elements and applying the scalar finite-element method, the following finite-element equation was derived [21]:

$$[K]\{\Psi\} - k_0^2 n_{eff}^2 [M]\{\Psi\} = \{0\}, \quad (3)$$

where $[K]$ and $[M]$ denote the finite-element matrices, $\{\Psi\}$ is the nodal electric/magnetic field vector, $\{0\}$ is the null vector, and k_0 and n_{eff} are, respectively, the wave number in vacuum and the effective refractive index. Here, n_{eff}^2 and $\{\Psi\}$ are, respectively, an eigenvalue and eigenvector of equation (3). The Neumann boundary condition is imposed on the computational window edges.

C. Two-dimensional equivalent straight waveguide

Figure 2 (a) shows an equivalent two-dimensional waveguide of the bent waveguide shown in Fig. 1. The refractive indices of the core and cladding are, respectively, denoted as n_{co} and n_{cl} , which are evaluated using the effective index method.

The bent waveguide can be mapped onto an equivalent straight waveguide (ESW), as shown in Fig. 2 (b), using a conformal transformation[23]. It is noted that the ESW is also applicable to cylindrical waveguides[24, 25]. Here, $u = R \ln(1 + \frac{q}{R})$, $q = r - R$, and $s = R\theta$. The refractive index distribution of the ESW, $n'(u)$, is expressed as follows [23–27]:

$$n'(u) = n(q) \left(1 + \frac{q}{R}\right), \quad (4)$$

where, $n(q)$ denotes the refractive index distribution of the bent waveguide and is expressed as follows:

$$n(q) = \begin{cases} n_{co} & (-\frac{w}{2} \leq q \leq \frac{w}{2}) \\ n_{cl} & (\text{otherwise}) \end{cases}. \quad (5)$$

D. Brief review of FD-BPM

Herein, we briefly review the two-dimensional FD-BPM. We consider an ESW as shown in Fig. 2 (b). From Maxwell's equations, the following wave equation is obtained:

$$\frac{\partial}{\partial u} \left(p_B \frac{\partial \Phi}{\partial u} \right) + \frac{\partial}{\partial s} \left(p_B \frac{\partial \Phi}{\partial s} \right) + k_0^2 q_B \Phi = 0, \quad (6)$$

where, $\Phi = E_y$, $p_B = 1$, $q_B = n^2(u)$ for the transverse electric (TE) modes, and $\Phi = H_y$, $p_B = 1/n^2(u)$, $q_B = 1$ for the transverse magnetic (TM) modes.

Substituting the solution of the form:

$$\Phi(u, s) = \varphi(u, s) \exp(-jk_0 n_0 s), \quad (7)$$

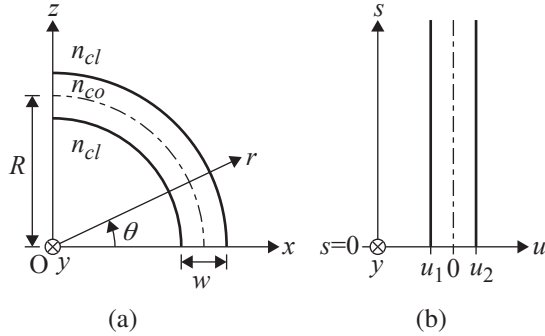


Fig. 2. (a) Two-dimensional bent waveguide and (b) its ESW for 2-D FD-BPM. Here, $u_1 = R \ln \left(1 - \frac{w/2}{R} \right)$ and $u_2 = R \ln \left(1 + \frac{w/2}{R} \right)$.

into equation (6), we obtain the following equation for the slowly varying complex amplitude φ :

$$p_B \frac{\partial^2 \varphi}{\partial s^2} - 2jk_0 n_0 p \frac{\partial \varphi}{\partial s} + \frac{\partial}{\partial u} \left(p_B \frac{\partial \varphi}{\partial u} \right) + k_0^2 (q_B - n_0^2 p_B) \varphi = 0, \quad (8)$$

where n_0 is the reference refractive index.

After applying the Padé approximation [28] and the finite-difference procedure, the following system of equations is derived [22]:

$$a_i^+ \varphi_{i-1}(s + \Delta s) + b_i^+ \varphi_i(s + \Delta s) + c_i^+ \varphi_{i+1}(s + \Delta s) = a_i^- \varphi_{i-1}(s) + b_i^- \varphi_i(s) + c_{i+1}^- \varphi_{i+1}(s), \quad (9)$$

where a^+ , b^+ , c^+ , a^- , b^- , and c^- are finite-difference coefficients; i represents values at the i th sampling point in the u -direction; and Δs denotes the propagation step size in the s -direction. equation (9) results in a system of N linear equations, when $\varphi_i(s)$ ($i = 1, 2, \dots, N$) are given. Here, N denotes the number of transverse sampling points. After solving equation (9), the propagating field of $\varphi_i(s + \Delta s)$ ($i = 1, 2, \dots, N$) are obtained. The transparent boundary condition [29] is used.

III. NUMERICAL RESULTS

A. Single-mode conditions

Figure 3 shows the boundary between single- and multi-mode regions for the rectangular waveguides with $\Delta n = 0.011$ at the wavelength of $9 \mu\text{m}$ evaluated by the FEM, where filled and open circles, respectively, represent single- and multi-mode operation. Hereafter, we consider square waveguides with $w = 15 \mu\text{m}$ and $t = 15 \mu\text{m}$, and rectangular waveguides with $w = 20 \mu\text{m}$ and $t = 15 \mu\text{m}$, which are operated in single mode.

Figure 4 shows the normalized propagation constant, $b = (n_{eff}^2 - n_{clad}^2) / (n_{core}^2 - n_{clad}^2)$, as a function of the wavelength for the square and rectangular waveguides with Δn of 0.09, 0.011, 0.013, and 0.015. Notably, no higher-order mode was found for each value of Δn

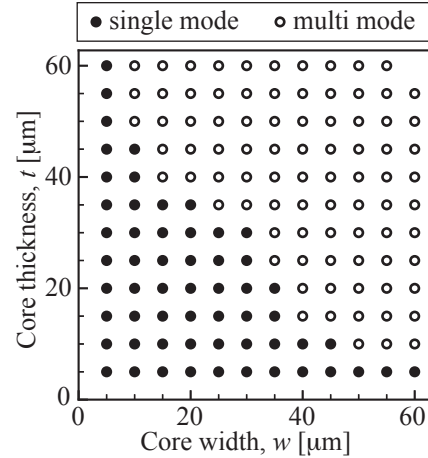


Fig. 3. Single-mode region for the IG2-glass-based waveguides with the refractive change, Δn , of 0.011 at a wavelength of $9 \mu\text{m}$.

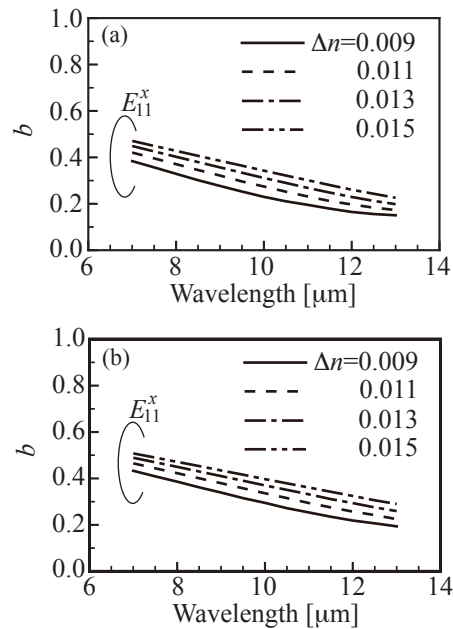


Fig. 4. Dispersion curves as a function of wavelength for waveguides with (a) $w = 15 \mu\text{m}$ and $t = 15 \mu\text{m}$ and (b) $w = 20 \mu\text{m}$ and $t = 15 \mu\text{m}$. No higher-order mode was found in the wavelength range.

over the wavelength range. Evidently, the waveguides are operated in single mode over the wavelength range and in the range of Δn .

It was experimentally and numerically shown that square waveguides with $w = t = 15 \mu\text{m}$ whose Δn s were in the range from 0.0097 to 0.0142 were operated in a single mode at the wavelength of $7.8 \mu\text{m}$ [15]. We can see that Fig. 4 (a) shows the same tendency.

B. Bending loss analysis

The two-dimensional FD-BPM was employed to estimate the bending losses of the ESWs. The fundamental mode of the original two-dimensional straight waveguide with a refractive index distribution of $n(q)$ was launched in the ESWs at the $s = 0$. The distribution of the fundamental mode is given as an initial field of the BPM calculation, which are denoted $\phi_i(0)$ ($i = 1, 2, \dots, N$) in equation (9). The spacing between transverse sampling points is $\Delta u = 0.1 \mu\text{m}$. The propagation step size $\Delta s = 5 \mu\text{m}$. The transverse computational window size was $100 \mu\text{m}$. A core of an ESW was placed in the center of the computational window. The pure bend loss (PBL) was evaluated using the steady-state differential power loss (DPL) level[30]. DPL was evaluated as follows [26, 31, 32]:

$$\Gamma(s) = -\frac{10}{\Delta s'} \log_{10} \left[\frac{P(s + \Delta s')}{P(s)} \right], \quad (10)$$

where $P(s)$ denotes the modal power at s , estimated by the overlap integral between the incident and propagating fields [27], and s and $s + \Delta s'$ represent the two points used to estimate the modal power. In other words, PBL is the slope of the graph of $\log_{10}(P(s))$ [22].

Figure 5 shows the bending radius and wavelength dependence of PBL on bent waveguides whose refractive index changes, Δn , are 0.11 with the square and rectan-

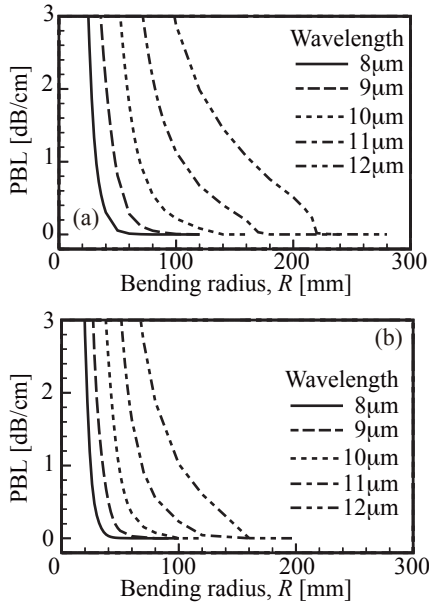


Fig. 5. Pure bend loss as a function of bending radius for bent waveguides, whose refractive index change, Δn , of 0.011, with (a) $w = 15 \mu\text{m}$ and $t = 15 \mu\text{m}$ and (b) $w = 20 \mu\text{m}$ and $t = 15 \mu\text{m}$.

gular core. Evidently, operation at a longer wavelength requires a larger bending radius to suppress the PBL, and the rectangular waveguides show smaller PBLs than the square waveguides because of the stronger confinement of optical waves due to the relatively larger cross-sectional areas of the cores.

Figure 6 shows the DPL levels as functions of propagation distance for the square bent waveguides with bending radii are $R = 20, 26,$ and 40 mm . Here, the refractive index changes, Δn , are 0.011, and the operation wavelengths are $8 \mu\text{m}$. Total lengths of these bent waveguides are taken as $R\pi/2$. The DPL values reached steady-state levels at the ends of the waveguides. The

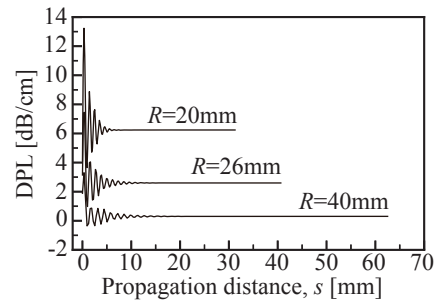


Fig. 6. Differential power loss (DPL) values of waveguides with $w = 15 \mu\text{m}$, $t = 15 \mu\text{m}$, and $\Delta n = 0.011$, at the wavelength of $8 \mu\text{m}$ for bending radii of 20, 26, and 40 mm.

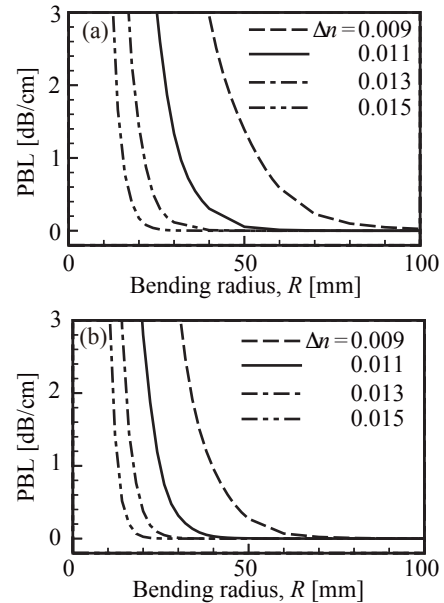


Fig. 7. Pure bend loss at a wavelength of $8 \mu\text{m}$ as a function of bend radius for bent waveguides with (a) $w = 15 \mu\text{m}$ and $t = 15 \mu\text{m}$ and (b) $w = 20 \mu\text{m}$ and $t = 15 \mu\text{m}$.

oscillatory nature of the DPL is due to coupling from higher-order modes of the bent waveguide back into the fundamental mode of the straight waveguide[26].

Figure 7 shows the PBL as a function of bending radius at the wavelength of $8\ \mu\text{m}$ for the square and the rectangular waveguides with $\Delta n = 0.009, 0.011, 0.013,$ and 0.015 . Evidently, the PBL strongly depends on the refractive index change, Δn . When the refractive index change decreases, the required bending radius rapidly increases to realize low-loss OICs.

As an practical example, we consider rectangular waveguides with $w = 20\ \mu\text{m}$, $t = 15\ \mu\text{m}$ and $\Delta n = 0.013$, whose cross-sections are approximately identical to the fabricated waveguides[14]. Figure 7 (b) shows that the PBL of the waveguides are less than 1.2×10^{-3} dB/cm for $R > 36$ mm at the wavelength of $8.0\ \mu\text{m}$.

IV. CONCLUSION

In this study, the single-mode conditions and the bending loss characteristics of IG2-glass-based optical waveguides operating in the mid-IR spectral range are revealed. Guided-mode analysis was performed using a scalar FEM. As a result, the single-mode region was shown for the waveguide with $\Delta n = 0.011$ at the wavelength of $9\ \mu\text{m}$, is shown. In addition, the square and the rectangular waveguides, whose core widths and heights are in the single-mode region, were operated in a single-mode over the mid-IR spectral range. Two-dimensional ESW models of the bent waveguides were analyzed using a two-dimensional FD-BPM. The dependence of the loss characteristics on the waveguide parameters was investigated. Through ULI, the loss characteristics were found to strongly depend on the refractive index change, Δn .

ACKNOWLEDGMENT

This study was supported by JSPS KAKENHI (grant number: JP22K03668).

REFERENCES

- [1] A. N. Dinkelaker, A. Rahman, J. Bland-Hawthorn, F. Cantalloube, S. Ellis, P. Feautrier, M. Ireland, L. Labadie, and R. R. Thomson, "Astrophotonics: Introduction to the feature issue," *J. Opt. Soc. Am. B*, vol. 38, no. 7, pp. AP1-AP6, July 2021.
- [2] J. Bland-Hawthorn and P. Kern, "Astrophotonics: A new era for astronomical instruments," *Opt. Express*, vol. 17, no. 3, pp. 1880-1884, Feb. 2009.
- [3] J. Bland-Hawthorn and S. G. Leon-Saval, "Astrophotonics: Molding the flow of light in astronomical instruments," *Opt. Express*, vol. 25, no. 13, pp. 15549-15557, June 2017.
- [4] S. Xie, J. Zhan, Y. Hu, Y. Zhang, S. Veilleux, J. Bland-Hawthorn, and M. Dagenais, "Add-drop filter with complex waveguide Bragg grating and multimode interferometer operating on arbitrarily spaced channels," *Opt. Lett.*, vol. 43, no. 24, pp. 6045-6048, Dec. 2018.
- [5] A. S. Nayak, T. Poletti, T. K. Sharma, K. Madhav, E. Pedretti, L. Labadie, and M. M. Roth, "Chromatic response of a four-telescope integrated-optics discrete beam combiner at the astronomical L band," *Opt. Express*, vol. 28, no. 23, pp. 34346-34361, Nov. 2020.
- [6] N. Cvetojevic, "Starlight on a chip: Astrophotonic technologies for interferometry," in P. G. Tuthill, A. Mérand, and S. Sallum, editors, *Optical and Infrared Interferometry and Imaging VII*, vol. 11446, p. 1144616, International Society for Optics and Photonics, SPIE, 2020.
- [7] M.-A. Martinod, P. Tuthill, S. Gross, B. Norris, D. Sweeney, and M. J. Withford, "Achromatic photonic tricouplers for application in nulling interferometry," *Appl. Opt.*, vol. 60, no. 19, pp. D100-D107, July 2021.
- [8] A. Benoît, F. A. Pike, T. K. Sharma, D. G. MacLachlan, A. N. Dinkelaker, A. S. Nayak, K. Madhav, M. M. Roth, L. Labadie, E. Pedretti, T. A. ten Brummelaar, N. Scott, V. C. du Foresto, and R. R. Thomson, "Ultrafast laser inscription of asymmetric integrated waveguide 3 dB couplers for astronomical K-band interferometry at the CHARA array," *J. Opt. Soc. Am. B*, vol. 38, no. 9, pp. 2455-2464, Sep. 2021.
- [9] M. M. Roth, K. Madhav, A. Stoll, D. Bodenmüller, A. N. Dinkelaker, A. Rahman, E. Hernandez, A. Günther, and S. Vjesnica, "Astrophotonics: Photonic integrated circuits for astronomical instrumentation," in S. M. García-Blanco and P. Cheben, editors, *Integrated Optics: Devices, Materials, and Technologies XXVII*, vol. 12424, p. 124240B, International Society for Optics and Photonics, SPIE, 2023.
- [10] M. Benisy, J.-P. Berger, L. Jocou, P. Labeye, F. Malbet, K. Perraut, and P. Kern, "An integrated optics beam combiner for the second generation VLTI instruments," *Astron. Astrophys.*, vol. 498, pp. 601-613, Oct. 2009.
- [11] R. R. Thomson, A. K. Kar, and J. Allington-Smith, "Ultrafast laser inscription: An enabling technology for astrophotonics," *Opt. Express*, vol. 17, no. 3, pp. 1963-1969, Feb. 2009.
- [12] J. E. McCarthy, H. T. Bookey, N. D. Psaila, R. R. Thomson, and A. K. Kar, "Mid-infrared spectral broadening in an ultrafast laser inscribed gallium lanthanum sulphide waveguide," *Opt. Express*, vol. 20, no. 2, pp. 1545-1551, Jan. 2012.
- [13] A. Ródenas, G. Martin, B. Arezki, N. Psaila, G. Jose, A. Jha, L. Labadie, P. Kern, A. Kar,

- and R. Thomson, "Three-dimensional mid-infrared photonic circuits in chalcogenide glass," *Opt. Lett.*, vol. 37, no. 3, pp. 392-394, Feb. 2012.
- [14] H. L. Butcher, D. G. MacLachlan, D. Lee, R. R. Thomson, and D. Weidmann, "Ultrafast laser-inscribed mid-infrared evanescent field directional couplers in GeAsSe chalcogenide glass," *OSA Continuum*, vol. 1, no. 1, pp. 221-228, Sep. 2018.
- [15] H. L. Butcher, D. G. MacLachlan, D. Lee, R. R. Thomson, and D. Weidmann, "Demonstration and characterization of ultrafast laser-inscribed mid-infrared waveguides in chalcogenide glass IG2," *Opt. Express*, vol. 26, no. 8, pp. 10930-10943, Apr. 2018.
- [16] L. Labadie and O. Wallner, "Mid-infrared guided optics: A perspective for astronomical instruments," *Opt. Express*, vol. 17, no. 3, pp. 1947-1962, Feb. 2009.
- [17] B. R. M. Norris, N. Cvetojevic, T. Lagadec, N. Jovanovic, S. Gross, A. Arriola, T. Gretzinger, M.-A. Martinod, O. Guyon, J. Lozi, M. J. Withford, J. S. Lawrence, and P. Tuthill, "First on-sky demonstration of an integrated-photonic nulling interferometer: The GLINT instrument," *Monthly Notices of the Royal Astronomical Society*, vol. 491, no. 3, pp. 4180-4193, Nov. 2019.
- [18] N. Hô, M. C. Phillips, H. Qiao, P. J. Allen, K. Krishnaswami, B. J. Riley, T. L. Myers, and N. C. Anheier, "Single-mode low-loss chalcogenide glass waveguides for the mid-infrared," *Opt. Lett.*, vol. 31, no. 12, pp. 1860-1862, June 2006.
- [19] Vitron, "IG2 datasheet," https://www.vitron.de/files/VITRON_IG-2_Datenblatt_Okt_2020_1_1_.pdf, Oct. 2020.
- [20] W. Hu, M. Kilinc, W. Gebremichael, C. Dorrer, and J. Qiao, "Morphology and waveguiding properties of ultrafast-laser-inscribed type-II waveguides in IG2," *Opt. Mater. Express*, vol. 12, no. 1, pp. 360-373, Jan. 2022.
- [21] M. Koshiba, *Optical Waveguide Theory by the Finite Element Method*, Tokyo, KTK Scientific Publishers, 1992.
- [22] G. Pedrola, *Beam Propagation Method for Design of Optical Waveguide Devices*, John Wiley & Sons, 2015.
- [23] M. Heiblum and J. Harris, "Analysis of curved optical waveguides by conformal transformation," *IEEE J. Quantum Electron.*, vol. 11, no. 2, pp. 75-83, Feb. 1975.
- [24] K. Petermann, "Microbending loss in monomode fibers," *Electron. Lett.*, vol. 12, no. 4, pp. 107-109, Feb. 1976.
- [25] J. Saijonmaa and D. Yevick, "Beam-propagation analysis of loss in bent optical waveguides and fibers," *J. Opt. Soc. Am.*, vol. 73, no. 12, pp. 1785-1791, Dec. 1983.
- [26] R. Baets and P. E. Lagasse, "Loss calculation and design of arbitrarily curved integrated-optic waveguides," *J. Opt. Soc. Am.*, vol. 73, no. 2, pp. 177-182, Feb. 1983.
- [27] Y. Nito, D. Kadowake, J. Yamauchi, and H. Nakano, "Bent embedded optical waveguide with a loaded metal film for reducing a polarization dependent loss," *J. Lightwave Technol.*, vol. 31, no. 19, pp. 3195-3202, Oct. 2013.
- [28] G. R. Hadley, "Wide-angle beam propagation using Padé approximant operators," *Opt. Lett.*, vol. 17, no. 20, pp. 1426-1428, Oct. 1992.
- [29] G. R. Hadley, "Transparent boundary condition for beam propagation," *Opt. Lett.*, vol. 16, no. 9, pp. 624-626, May 1991.
- [30] J. Yamauchi, T. Ando, M. Ikegaya, and H. Nakano, "Effects of trench location on the attenuation constant in bent step-index optical waveguides," *IEICE Trans. Electron.*, vol. E77-C, no. 2, pp. 319-321, Feb. 1994.
- [31] M. Rivera, "A finite difference BPM analysis of bent dielectric waveguides," *J. Lightwave Technol.*, vol. 13, no. 2, pp. 233-238, Feb. 1995.
- [32] W. J. Song, G. Song, B. H. Ahn, and M. Kang, "Scalar BPM analyses of TE and TM polarized fields in bent waveguides," *IEEE Trans. Antennas Propag.*, vol. 51, no. 6, pp. 1185-1198, June 2003.



Takashi Yasui graduated with the B.S. degree in Electronic Engineering from Fukui University, Fukui, Japan, in 1997, and the M.S. and Ph.D. degrees in Electronic Engineering from Hokkaido University, Sapporo, Japan, in 1999 and 2001, respectively. From 1999 to 2002, he

was a Research Fellow of the Japan Society for the Promotion of Science. In 2002, he joined Fujitsu Ltd., Chiba, Japan. From 2004 to 2011, he was an Assistant Professor of the Department of Electronic and Control Systems Engineering, Shimane University, Matsue, Japan. Since 2011, he has been an Associate Professor of the Faculty of Engineering, Kitami Institute of Technology, Kitami, Japan. He has been engaged in research on wave electronics. Yasui is a member of the IEEE, the Optica, and the Institute of Electronics, Information and Communication Engineers (IEICE) of Japan. In 2018, he was awarded the Excellent Paper Award from IEICE.

An Investigation of the Relationship between Effective Relative Permittivity and Infill Density in a 3D Printed Slab

Bibek Kattel, Winn Elliott Hutchcraft, and Richard K. Gordon

Department of Electrical and Computer Engineering
University of Mississippi, Oxford, MS, USA
{bkattel1, eeweh, eegordon}@olemiss.edu

Abstract – This paper presents a simulation-based study on the relative permittivity of 3D printed dielectric slabs printed with varying infill densities. In this study, a percentage volumetric model has been employed to model the infill density in a 3D printed dielectric slab. The relative permittivity of the filament material used to design the slab is assumed to be 2.45. The modeled slab is fitted into various rectangular waveguides with varying dimensions corresponding to different frequency ranges. As the infill density decreases, the relative permittivity of the dielectric slabs decreases. This lower value of relative permittivity is referred to as effective relative permittivity ($\epsilon_{r,\text{eff}}$) throughout the paper. The study concludes that the effective relative permittivity of the slab decreases linearly as the infill density is decreased for the model. This study offers valuable insights into the effective relative permittivity of dielectric slabs under varying infill densities, providing implications for applications in areas such as antenna design.

Index Terms – 3D printing, antenna optimization, effective relative permittivity, infill density model, patch antenna, waveguide.

I. INTRODUCTION

3D printing, a technique that constructs a structure by successively depositing layers, is governed by several parameters, one of which is the infill density. This parameter represents the amount of printed material used to create a structure. When manufacturing 3-dimensional antennas via 3D printing, a dielectric material is often necessary as a support structure. While it may seem beneficial to design an antenna with 100% infill density for enhanced mechanical strength of the dielectric material, utilizing a lower infill density can expedite the prototyping process. Moreover, it contributes to lowering other design parameters such as dielectric loss, manufacturing cost, the overall mass of the printed structure, and the relative permittivity of the dielectric material [1, 2]. Furthermore, it has been demonstrated in [3] that lower infill densities can achieve equivalent results in antenna design, underscoring the potential advantages of employ-

ing lower infill densities in antenna design. The permittivity of the dielectric material affects the optimal operating frequency of an antenna, as evidenced in [4]. Therefore, an appropriate infill density serves as a valuable parameter in radio frequency and antenna designs.

The existence of a linear relationship between the effective relative permittivity and infill density has been identified experimentally for various infill patterns in [1, 2, 5]. However, a comprehensive investigation into the modeling of infill density and patterns, establishing a conclusive correlation between these 3D printing parameters and electrical parameters, remains unexplored in the literature. Additionally, the phenomena behind this observed linear relationship remain yet to be elucidated.

This paper aims to model the infill density in a 3D printed dielectric slab to study the correlation between infill density and relative permittivity. The infill model is used to compute the effective relative permittivity ($\epsilon_{r,\text{eff}}$) of the dielectric slab at 30%, 50%, and 70% infill density by placing the modeled slab within 7 distinct waveguides of varying dimensions. Additionally, the paper presents an equation formulated to determine $\epsilon_{r,\text{eff}}$ for the infill densities lower than 100%. It further demonstrates the practical implementation of the infill model in optimizing a patch antenna's substrate designed with infill densities lower than 100%. The relative permittivity for the printed material at 100% infill was set at 2.45. CST Microwave Studio, a 3D electromagnetic simulation software, was used for the simulations conducted in this study.

II. MODELING INFILL DENSITY

In this study, a simple model has been developed for infill density, which is based on the ratio of the volume of the printed material to the volume of the fabricated dielectric structure. This volumetric model implies that for a fabricated dielectric structure, 100% infill corresponds to the entire volume of the structure being composed of 3D printing filament material. Conversely, 50% infill indicates that only half of the total volume is the 3D printed material, with the remaining 50% being an

air-gap. The infill pattern is designed to be straightforward, featuring a repeated block of printed material and air-gap alternately on the top layer, with the same pattern repeated in the layers underneath.

Figure 1 presents a cross-sectional view of the dielectric slab represented by the proposed model where the printed material is represented by cyan-colored blocks within the yellow-colored waveguide. It can be seen that 70% infill exhibits higher material density compared to the 50% infill. The thickness of the slab is along the z-axis. The model was constructed such that both the larger and smaller cross-sectional inner dimensions (“a” and “b” in Figs. 1 and 2) of the waveguide were subdivided each into 10 small unit cells. The x-length of the unit cell was multiplied by the infill density factor to get the length of the printed material within the unit cell in the x direction so that the volume of the printed material in the unit cell to the volume of the unit cell represents the infill density for the dielectric slab. This approach allows for an easy method to vary the infill density by adjusting the infill percentage factor and accurately modeling infill density in terms of the volume of the printed material.

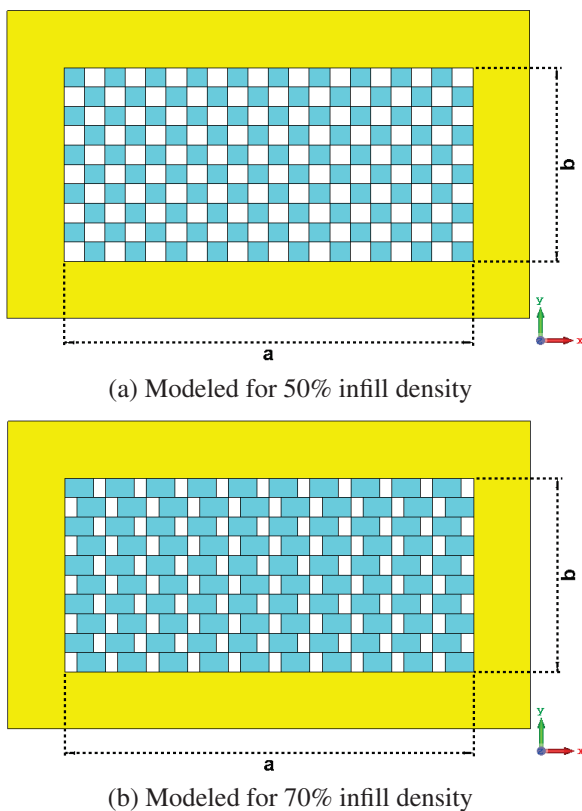


Fig. 1. Cross-sectional view of modeled slabs within waveguide, each cyan block representing a unit cell.

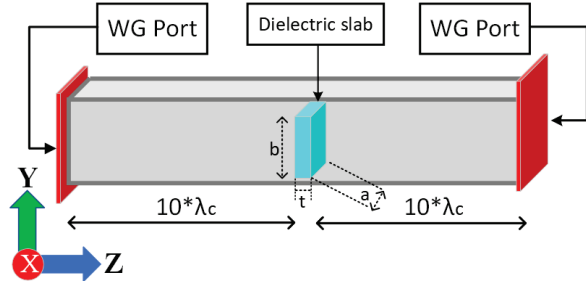


Fig. 2. Model of the simulation setup depicting the waveguide and the dielectric slab.

III. SIMULATION SETUP

In this study, 7 waveguides were employed for simulations, with their dimensions listed in Table 1. These waveguides served as a basis for planned experimental assessments, based on these simulations. The frequency range encompassed by the waveguides spanned from 1 GHz (approximately 376 MHz below the WR430 cutoff frequency) to 21 GHz (within the operational range of WR42). In the simulation setup demonstrated in Fig. 2, both waveguide ends were excited by identical waveguide ports, with the dielectric slab positioned between two air-filled waveguide sections. These sections extended a length equivalent to 10 times the cutoff wavelength (based on TE_{10} mode of operation) from each side of the slab to each end of the waveguides. This configuration emulates the intended experimental setup, facilitating the attenuation of higher-order modes present at the air/material interface.

Table 1: Waveguide parameters for simulations

Waveguide	Cross Section (a * b)	f_c (GHz)
WR430	109 mm × 55 mm	1.37
WR284	72 mm × 34 mm	2.08
WR187	48 mm × 22 mm	3.13
WR137	35 mm × 16 mm	4.29
WR90	23 mm × 10 mm	6.52
WR62	16 mm × 7.9 mm	9.38
WR42	11 mm × 4.3 mm	13.63

The various slabs used in this study share a common thickness (“t” in Fig. 2) of 27 mm, while their cross-sectional dimensions adapt to the respective waveguide dimensions. The design ensures that the inner dimensions of the waveguide fit snugly with the outer dimensions of the dielectric slabs. The dielectric slabs were oriented such that their thickness was along the z-axis as seen in Fig. 2.

The simulation results were expressed in terms of S-parameters. Since the waveguide sections were identical,

the simulations yielded equivalent S_{11} and S_{22} and equivalent S_{12} and S_{21} , as expected. The S_{11} results were utilized to derive the $\epsilon_{r,\text{eff}}$, as detailed in subsequent sections. It was observed that the S_{12} values were closer to 0 dB above the cutoff frequency ranges, indicating that most of the power was transmitted between the ports, as the dielectric slabs were considered to be lossless. These values could be used to estimate the loss tangent of lossy dielectric slabs in future studies, but we did not use them for further analysis in this study, as our primary focus was investigating the real part of the permittivity.

IV. METHODOLOGY

To elucidate the methodology used to estimate the permittivity values, initially, the parameters of the simulations were defined. A specific notation was introduced for clarity and conciseness throughout the simulation process:

$$\text{WG}(\text{infill}\%, \epsilon_{ra}),$$

where “WG” corresponds to one of the specific waveguides in Table 1, “infill%” represents the infill density of the dielectric slab, “ ϵ_{ra} ” signifies the relative permittivity value of the filament material used to fabricate the slab. For instance, WR187(70%, 2.45) represents a WR187 waveguide in which a dielectric slab with 70% infill density is inserted. The permittivity value of the filament material used to fabricate the slab was 2.45.

The algorithm proposed for determining the $\epsilon_{r,\text{eff}}$ for a specific dielectric slab is delineated as follows:

1. *Initialization:* Define a dielectric slab for which the effective relative permittivity needs to be ascertained, e.g., WR187(50%,2.45).
2. *Primary Simulation:* Simulate the waveguide setup with the dielectric slab and record the S_{11} result, e.g., S_{11} :WR187(50%,2.45).
3. *Record Minimum:* Document the frequency at which the minimum occurs for S_{11} , e.g., f_m :WR187(50%,2.45).
4. *Secondary Simulation:* Simulate the same waveguide setup identical to Step 2, but with the slab at 100% infill density with ϵ_{ra} set as a variable, e.g., WR187(100%, ϵ_{ra}). Record the minimum as mentioned in Step 3, e.g., f_m :WR187(100%, ϵ_{ra}).
5. *Iteration/Optimization:* Repeat Step 4 until the absolute difference between the minimum of the Primary and Secondary simulations is less than an error threshold (e_{th}).

The error threshold (e_{th}) was set as 0.02 GHz for this study. So, the condition that had to be satisfied for the proposed algorithm was

$$|f_m : \text{WR187}(50\%, 2.45) - f_m : \text{WR187}(100\%, \epsilon_{ra})| \leq e_{th}. \quad (1)$$

The ϵ_{ra} value that satisfies expression 1 is considered to be the $\epsilon_{r,\text{eff}}$ for WR187(50%,2.45). An

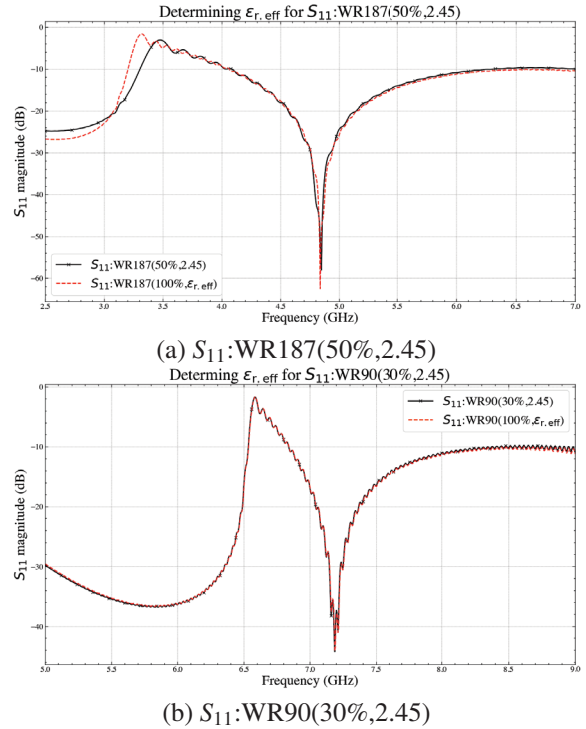


Fig. 3. Illustration of the proposed algorithm to determine $\epsilon_{r,\text{eff}}$.

example of the result obtained using this methodology is presented in Fig. 3 (a), where two data sets for WR187 namely, S_{11} :WR187(50%,2.45) and S_{11} :WR187(100%, $\epsilon_{r,\text{eff}}$) have been plotted together. The two data sets exhibit a good match, thereby indicating that the determined $\epsilon_{r,\text{eff}}$ indeed represents the appropriate permittivity for WR187(50%,2.45) dielectric slab. Another example has been presented in Fig. 3 (b), where the permittivity for S_{11} :WR90(30%,2.45) has been estimated. This simulation-based optimization methodology was employed to determine the $\epsilon_{r,\text{eff}}$ values for each of the dielectric slabs at 30%, 50%, and 70% infill density.

V. RESULTS

Table 2 lists the permittivity values estimated using the proposed algorithm for each of the dielectric slabs at 30%, 50%, and 70% infill density. From Table 2, it can be seen that the $\epsilon_{r,\text{eff}}$ is in close range of 1.4, 1.7, and 2 for 30%, 50%, and 70% infill, respectively, for all the dielectric slabs considered in this study.

The algorithm was further employed for WR187 to estimate $\epsilon_{r,\text{eff}}$ for all the infill densities between WR187(0%,1) and WR187(100%,2.45) in the interval of 10%. The results for the estimated $\epsilon_{r,\text{eff}}$ (black dots) were plotted against infill density in Fig. 4. Additionally, a straight line joining the two endpoints, i.e., WR187(0%,1) and WR187(100%,2.45) was drawn (red

colored line) to aid in visualizing the variation in estimated $\epsilon_{r,\text{eff}}$ values with infill density.

VI. DISCUSSION

The estimated permittivity values presented in Table 2 elucidate that regardless of the variations in waveguide dimensions and operating frequencies, the estimated permittivity of dielectric slabs remained nearly consistent at each specific infill density. This suggests that the proposed infill model is frequency independent.

Table 2: Estimated $\epsilon_{r,\text{eff}}$ with proposed algorithm

Dielectric Slab	30% Infill	50% Infill	70% Infill
WR430 slab	1.400	1.653	1.990
WR284 slab	1.425	1.715	2.025
WR187 slab	1.411	1.715	2.008
WR137 slab	1.422	1.728	2.000
WR90 slab	1.413	1.716	2.011
WR62 slab	1.416	1.722	2.005
WR42 slab	1.410	1.721	1.997

Furthermore, when the estimated $\epsilon_{r,\text{eff}}$ values are plotted against their corresponding infill densities as presented in Fig. 4, a consistent linear relationship between $\epsilon_{r,\text{eff}}$ values and infill density is evident. This is denoted by the fact that the estimated $\epsilon_{r,\text{eff}}$ values (black dots) closely align with the straight red line. While this was specifically tested for WR187, it is reasonable to conclude that this relationship should hold true for the other waveguides across the entire range of simulation frequencies. This assertion is based on the consistent results generated by the proposed infill model at each of the specified infill densities outlined in Table 2. The results of the model proposed in this study are consistent with the experimental study in [1, 2, 5], where a linear correlation between $\epsilon_{r,\text{eff}}$ and infill density was observed. This indicates that the slicer software used in those 3D printers produces the infill density appropriately similar to

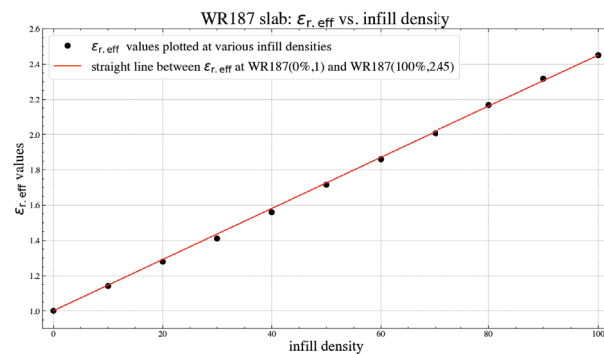


Fig. 4. Linearity demonstrated between $\epsilon_{r,\text{eff}}$ values and infill density in WR187 waveguide.

the model used in this study. However, if the slicer software does not add material for a particular infill density accordingly, possibly for structural integrity or other reasons, the relationship may deviate from being linear. This underscores the importance of standardizing slicer software, a point emphasized in [1].

From the results obtained, this relationship can be leveraged to estimate $\epsilon_{r,\text{eff}}$ using the linear relation described by the equation:

$$\epsilon_{r,\text{eff}} = \frac{\epsilon_{r100} - \epsilon_{r0}}{100} * (\text{infill}\%) + \epsilon_{r0}, \quad (2)$$

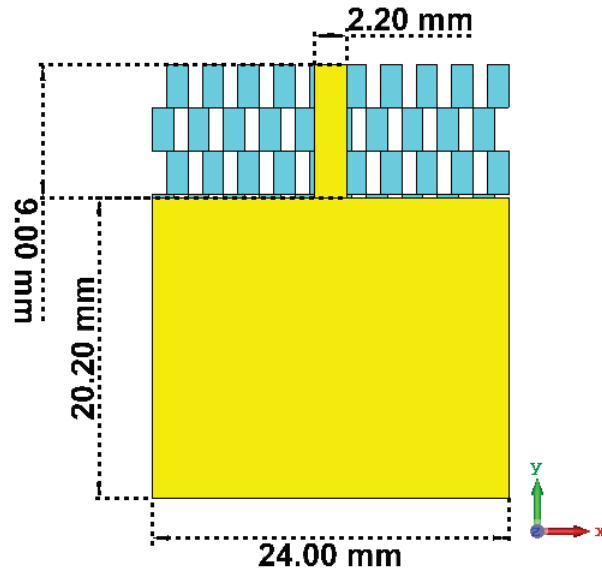
where $\epsilon_{r,\text{eff}}$ represents the effective relative permittivity to be determined for a lower infill%, ϵ_{r100} , and ϵ_{r0} are the relative permittivity of the printed material/slab at 100% infill density and air, respectively. Utilizing equation 2 for a material with $\epsilon_{r100} = 2.45$, with the fact that $\epsilon_{r0} = 1$, we computed $\epsilon_{r,\text{eff}}$ at 30%, 50%, and 70%, resulting in 1.435, 1.725, and 2.015 respectively. These values align closely with those obtained in Table 2, demonstrating that equation 2 effectively evaluates the simulation results.

The simulations performed in this study successfully implement an infill density model that establishes a clear linear relationship between $\epsilon_{r,\text{eff}}$ and infill density. These findings have broader implications, as they can be used to interpolate $\epsilon_{r,\text{eff}}$ values at specific infill densities. This capability could be leveraged for design purposes, offering a valuable tool for optimizing permittivity for various applications while utilizing the same core filament material. An example to demonstrate its effectiveness has been presented in the subsequent subsection.

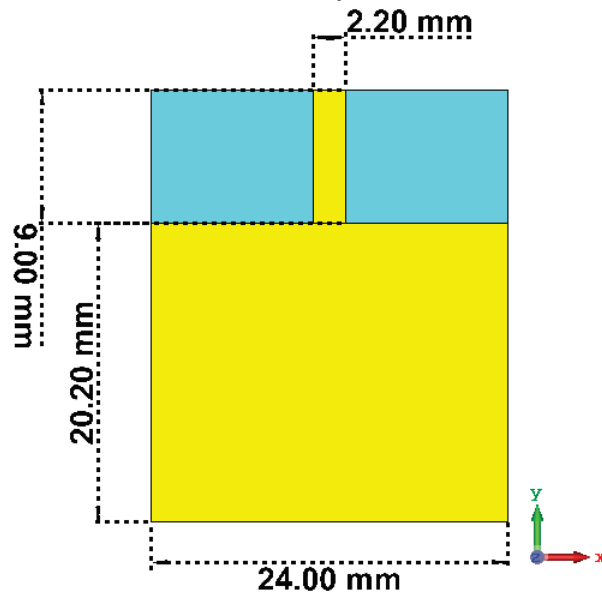
A. Implementing the model to optimize permittivity for the substrate of a patch antenna

In this section, the implementation of the model in optimizing the permittivity of the substrate of a simple patch antenna is demonstrated. Two patch antennas, as illustrated in Fig. 5, were designed in CST Microwave Studio. Patch 1 substrate is modeled with 60% infill density using the volumetric model as shown in Fig. 5 (a), while Patch 2 presented in Fig. 5 (b) is without substrate modeling. Both patches share identical dimensions, as detailed in Fig. 5 with a 2 mm substrate thickness. The yellow color denotes the copper layer, while blue represents the substrate. Notably, both patches have a full ground plane on the backside, hidden in Fig. 5 for clarity of the infill model.

Consider a scenario where a patch antenna achieving resonance at 5 GHz necessitates a substrate with permittivity of 1.87, yet only filament with $\epsilon_r = 2.45$ is available. The hypothesis questions if using that filament ($\epsilon_r = 2.45$) to design a substrate requiring $\epsilon_r = 1.87$ is feasible. To investigate, patch1 (60%, 2.45) was simulated and, simultaneously, another patch patch2 (100%, $\epsilon_{r,\text{eff}}$) was simulated with its substrate permittivity set



(a) Patch 1 with substrate modeled for 60% infill density



(b) Patch 2 with unmodeled substrate

Fig. 5. Implementing the model to optimize patch antenna.

as $\epsilon_{r,\text{eff}} = 1.87$, computed using equation 2. The results of both simulations are presented in Fig. 6, indicating a close overlap between the two plots. This suggests that the substrate printed at 60% infill using a filament with $\epsilon_r = 2.45$ accurately represents a permittivity of 1.87, potentially utilizing infill density as a parameter for antenna design.

Additionally, a simulation for patch2 (100%, 2.45) demonstrates the repercussions of unoptimized infill

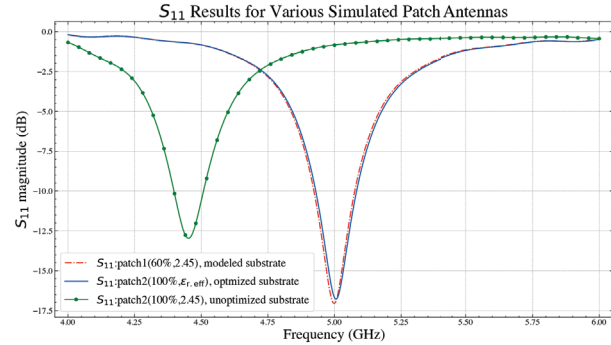


Fig. 6. Demonstrating optimized patch antenna vs. a non-optimized patch antenna.

density, causing the antenna to operate at an unintended frequency range, as seen in Fig. 6. The green solid line with dots representing this result underscores the importance of utilizing appropriate infill density for the antenna substrate to achieve the desired antenna performance. Indeed, our initial experimental research of 3D printing antennas resulting in unexpected resonances due to inadequate knowledge of infill density is what led to this research in the first place.

The results obtained for patch1(60%,2.45) and patch2(100%, $\epsilon_{r,\text{eff}}=1.87$) in Fig. 6, suggest a simplification in modeling. It highlights the potential to bypass explicit infill density modeling for future antenna substrate simulations by simply using the $\epsilon_{r,\text{eff}}$ from equation 2. This “100% infill” substrate with the $\epsilon_{r,\text{eff}}$ can at a minimum, initially, negate the need for infill modeling in the design process, and that should result in quicker simulation times.

VII. CONCLUSION AND FUTURE WORK

This study contributes valuable insights into modeling infill density, elucidating a consistent linear relationship between $\epsilon_{r,\text{eff}}$ values and infill densities. The study reveals that the increment of printed material should align linearly with increasing infill density to preserve this relationship, a crucial aspect demonstrated through the volumetric model. The derived linear equation for the model facilitates precise estimation of relative permittivity for optimizing design parameters requiring lower infill or permittivity values in specific applications. Additionally, the significance of standardizing slicer software in 3D printing processes is also highlighted to preserve this relationship.

In this study, the unit cells were designed to vary solely along the x and y directions. However, for future studies extending it to vary along the z-axis for each unit cell could allow more design flexibility and still retain the volumetric method to regulate the infill density for the printed structure as demonstrated in [6]. In upcoming

research, the focus will be on experimentally validating the simulation model. This entails manufacturing dielectric slabs with different infill densities for various waveguides and subsequently comparing the effective relative permittivity obtained from simulations with empirically measured data. Additionally, attention will be given to investigating an analytical approach to develop a theoretical model on the effective relative permittivity for the lower infill densities. These studies hold substantial promise for designing and manufacturing customized dielectric substrates with tailored dielectric properties, further broadening the scope of applications of 3D printing technology across various domains.

ACKNOWLEDGMENT

We are thankful to the Raytheon Co. and the National Science Foundation as this work was supported in part by the NSF Industry-University Cooperative Research Centers (I-UCRC) under Grant 1822104. We acknowledge the use of SciencePlots [7] and Matplotlib for creating the plots in this paper.

REFERENCES

- [1] B. Kattel, W. E. Hutchcraft, and R. K. Gordon, "Exploring infill patterns on varying infill densities on dielectric properties of 3D printed slabs," *2023 Antenna Measurement Techniques Association Symposium (AMTA)*, pp. 1-5, 2023.
- [2] B. T. Malik, V. Doychinov, S. A. R. Zaidi, I. D. Robertson, and N. Somjit, "Antenna gain enhancement by using low-infill 3D-printed dielectric lens antennas," *IEEE Access*, vol. 7, pp. 102467-102476, 2019.
- [3] B. Kattel, W. E. Hutchcraft, and R. K. Gordon, "3D printed patch antennas with varying infill densities," *2023 Antenna Measurement Techniques Association Symposium (AMTA)*, pp. 1-5, 2023.
- [4] B. Kattel, "Evaluation of wireless router antennas and 3D-printed simulated antenna designs," *Electronic Theses and Dissertations*, vol. 1769, 2019.
- [5] H. Hu, S. Sinha, N. Meisel, and S. G. Bilén, "Permittivity of 3D-printed nylon substrates with different infill patterns and densities for design of microwave components," *Designs*, vol. 4, no. 3, 2020.
- [6] B. F. LaRocca and M. S. Mirotznik, "Modeling the performance impact of cubic macro cells used in additively manufactured luneburg lenses," *Applied Computational Electromagnetics Society (ACES) Journal*, vol. 37, no. 10, pp. 1077-1088, 2023.
- [7] J. D. Garrett, "garrettj403/SciencePlots," *Zenodo*, Sep. 2021.



Bibek Kattel is a doctoral candidate in the Department of Electrical and Computer Engineering at the University of Mississippi, Oxford, MS. He earned his M.Sc. in Electrical Engineering with an emphasis in Electromagnetics from the same university in 2019.

His current research focuses on the design and fabrication of 3D printed antennas, RF and antenna measurements, and exploring novel materials for 3D printing applications. In addition to research, he has a passion for teaching and has taught an electronics course at the University of Mississippi in Fall 2023. He is a member of Phi Kappa Phi.



W. Elliott Hutchcraft was born in Lexington, Kentucky on April 29, 1973. He earned his B.S. in electrical engineering at the University of Mississippi, Oxford, MS in 1996, his M.S. in electrical engineering at the University of Mississippi, Oxford, MS in 1998, and his Ph.D. in electrical engineering at the University of Mississippi, Oxford, MS in 2003.

He is an Associate Professor in the Department of Electrical and Computer Engineering at the University of Mississippi in Oxford, Mississippi. Dr. Hutchcraft is a member of Eta Kappa Nu, IEEE, Tau Beta Pi, and Phi Kappa Phi.



Richard K. Gordon is from Birmingham, Alabama. He earned his B.S. in physics at Birmingham-Southern College, Birmingham, AL in 1983, his M.S. in applied mathematics at the University of Illinois, Urbana, IL in 1986, and his Ph.D. in electrical engineering at the University of Illinois, Urbana, IL in 1990.

He is an Associate Professor in the Department of Electrical and Computer Engineering at the University of Mississippi in Oxford, Mississippi. Dr. Gordon is a member of Eta Kappa Nu, Phi Beta Kappa, and Tau Beta Pi.

Resonant Frequency Modelling of Microstrip Antennas by Consensus Network and Student's-T Process

Xuefeng Ren¹, Yubo Tian², Qing Li³, and Hao Fu⁴

¹Ocean College Jiangsu University of Science and Technology
Zhenjiang, 212100, China
211110302104@stu.just.edu.cn

²School of Information and Communication Engineering Guangzhou Maritime University
Guangzhou 510725, Guangdong, China
tianyubo@just.edu.cn

³Ocean College Jiangsu University of Science and Technology
Zhenjiang, 212100, China
leo199808@163.com

⁴Ocean College Jiangsu University of Science and Technology
Zhenjiang, 212100, China
2841689068@qq.com

Abstract – When modelling and optimizing antennas by machine learning (ML) methods, it is the most time-consuming to obtain the training samples with labels from full-wave electromagnetic simulation software. To address the problem, this paper proposes an optimization method based on the consensus results of multiple independently trained Student's-T Process (STP) with excellent generalization ability. First, the STP is introduced as a surrogate model to replace the traditional Gaussian Process (GP), and the hyperparameters of the STP model are optimized. Afterwards, a consistency algorithm is used to process the results of multiple independently trained STPs to improve the reliability of the results. Furthermore, an aggregation algorithm is adopted to reduce the error obtained in the consistency results if it is greater than the consistency flag. The effectiveness of the proposed model is demonstrated through experiments with rectangular microstrip antennas (RMSA) and circular microstrip antennas (CMSA). The experimental results show that the use of multiple independently trained STPs can accelerate the antenna design optimization process, and improve modelling accuracy while maintaining modelling efficiency, which has high generalization ability.

Index Terms – Antenna optimization, Consensus network, Gaussian Process, Student's-T Process.

I. INTRODUCTION

In the past research, the optimal design of electromagnetic (EM) components has often relied on numerical simulation or full-wave EM simulation software, such as High-Frequency Structure Simulator (HFSS), Computer Simulation Technique (CST), and combined with global optimization algorithms [1, 2] to perform research experiments with significant results. Although these numerical simulation tools can provide high fidelity simulation results, the process of evaluating the performance of EM components requires multiple calls to the EM simulation software, and each calculation is time-consuming and inefficient. As a result, the focus of current research has shifted to the surrogates of EM simulation software to assess the suitability of EM components. The introduction of surrogates offers the advantage of saving time and resources, especially for the more complex EM components. Surrogates are approximate models that allow predictions and evaluations in a short time by analyzing and modelling a small amount of EM simulation data, thereby improving computational efficiency while maintaining some accuracy. Some modelling methods such as Artificial Neural Networks (ANN) [3–5], Support Vector Machines (SVM) [6, 7], Extreme Learning Machines (ELM) [8–10], Gaussian Processes (GP) [11–13] and Backpropagation (BP) [14] are currently

in use and can effectively solve electromagnetic problems.

ANN has a powerful self-learning capability to handle complex problems, but it requires a large amount of simulation data, and determining its structure is very difficult. SVM has good generalization ability and is suitable for small samples, which can effectively avoid "dimensional disaster" due to its final decision function, but the predicted output is not probabilistic and its kernel parameters are difficult to determine. As a classical surrogate, GP can not only face complex mathematical problems, but also solve mathematical problems in high-dimensional space, and its mathematical theoretical foundation is more rigorous [15]. However, the posterior distribution of the GP always depends on the observations, and its outliers are a preferential assumption, leading to extreme outlier observations that cannot effectively be ignored [16]. The Student's-T Process (STP) obeys the Student's-T distribution rather than the Gaussian distribution, it has a more flexible posterior variance and more robust performance compared to the GP. Shah et al. obtained the closed expressions for the marginal likelihood and predictive distribution of the STP by inverting the Wishart integral process over the covariance kernel of the GP model, and it was shown that the STP not only retains the properties of the non-parametric representation of the GP but also has greater flexibility concerning the predicted covariance [17]. Sloin and Särkkä added a noise covariance function to the parametric kernel to construct the STP, and used it as an alternative to GP, which can make the computation more concise [18]. Tang et al. proposed STP with the Student's-T likelihood for dealing with input and target outliers [19]. Chen et al. constructed a unified framework to derive a multivariate STP model, which not only addressed some of the shortcomings of existing methods in solving multiple output prediction problems but was also more effective compared to the traditional GP [20].

As a Machine Learning (ML) technique, STP is easy to implement with few parameters in the learning process, achieves better results in solving non-linear, high-dimensional problems with small sample sizes, and the final result has probabilistic significance [21]. STP can effectively map the non-linear functional dependencies between the input and output, and become a valuable tool for the modelling and optimization of complex EM problems. However, sometimes, the accuracy and reliability of STP results remain problematic. Even after adequate training, the predicted results of STP still have errors that cannot be neglected compared with ones obtained by full-wave EM simulation software. When STP is used to optimally design an antenna, these deviations can temporarily or permanently lead the optimization in

the wrong direction, thereby prolonging the optimization time or rendering the antenna design infeasible.

This paper proposes a generic method for the optimal design of antennas, reducing the uncertainty of the results obtained from a single STP. It is based on consensus results from multiple independently trained STPs. First, STP is introduced as a surrogate to replace the conventional GP and its hyperparameters are optimized. Then, a consensus algorithm is used to process the results of multiple independently trained STPs to improve the reliability of the results. Moreover, an aggregation algorithm is adopted to reduce the error of the consensus results if it is greater than the consistency flag.

The rest of this paper is structured as follows. The second part gives a brief description of GP and STP. The third part details the basic principles, model structure and algorithm flowchart and pseudo-code of the consistency-based STP model. The fourth part is the experiments, including the resonant frequencies of rectangular microstrip antennas (RMSA) and circular microstrip antennas (CMSA), and the modelling results of different methods show that the proposed consensus STP network, named C-STP, is more effective. The last part is the conclusion and outlook.

II. BACKGROUND INFORMATION

A. Gaussian process

GP is a powerful ML method, which can be determined only by the mean function and covariance function, as shown in equation (1):

$$\begin{cases} m(x) = E(f(x)) \\ k(x, x') = E\{[f(x) - m(x)][f(x') - m(x')]\} \end{cases} \quad (1)$$

In the above formula, $x, x' \in R^d$ are any random variables, $m(x)$ is the mean value function, and $k(x, x')$ is the covariance function. GP can be further expressed by the following equation [22]:

$$f(x) \sim GP(m(x), k(x, x')). \quad (2)$$

If there are n observations in the training set $D = \{(x_i, y_i) | i = 1, 2, \dots, n\}$, $X_i = [x_1, x_2, \dots, x_n]$ is a $d \times n$ -dimensional input training matrix with n d-dimensional input training vectors. $y = [y_1, y_2, \dots, y_n]^T$ is a training output vector with n training output scalar y_i . If there is noise ε , the regression model can be expressed as $y = f(x) + \varepsilon$, where ε is a random variable obeying a normal distribution with a mean of 0 and a variance of σ_n^2 , which can be expressed as:

$$\varepsilon \sim N(0, \sigma_n^2). \quad (3)$$

Then the prior distribution of the observed target value is as follow:

$$y \sim N(0, K + \sigma_n^2 I), \quad (4)$$

where $K = K(X, X)$ is a symmetric positive definite covariance matrix of order $n \times n$, and I is the identity matrix. Outputs y of n training samples and f^* of n^* test

samples forms a joint Gaussian prior distribution, which can be expressed as:

$$\begin{bmatrix} y \\ f^* \end{bmatrix} \sim N(0, \begin{pmatrix} K(X, X) + \sigma_n^2 I & K(X, X^*) \\ K(X^*, X) & K(X^*, X^*) \end{pmatrix}). \quad (5)$$

In the above equation, $K(X, X^*)$ is the $n \times n^*$ order covariance matrix between n^* test samples and n training samples, and $K(X^*, X^*)$ is the $n^* \times n^*$ order covariance matrix of n^* test samples.

Typically, the covariance matrix of GP regression model, also known as kernel function, is chosen from the Automatic Relevance Determination (ARD) series of squared exponential kernels, which contain a set of hyperparameters that determine the nature of the GP model. In the actual modelling process, the hyperparameters of the GP model are determined through calculating the maximum likelihood function. First, the conditional probabilities of the log marginal likelihood functions of the training samples are constructed, and then the bias derivatives of the hyperparameters contained therein are obtained. Finally, the hyperparameters are optimized using a conjugate gradient optimization method to find the optimal solution. The expression for the negative log-likelihood function is given by:

$$l = \log p(y|\theta, X) = -\frac{1}{2}y^T K^{-1}y - \frac{1}{2} \log |K| - \frac{n}{2} \log 2\pi. \quad (6)$$

After the optimal value of the hyperparameter is obtained, the trained GP is used for predictions.

Given a new set of data input x^* , based on the trained GP model with the training set (X, y) , the posterior distribution of the predicted value y^* of the new input x^* can be written:

$$p(y^*|x^*, X, y) = N(\mu, \Sigma), \quad (7)$$

where formula (8) is the predicted mean value matrix, and formula (9) is the predicted covariance matrix:

$$m = K(X^*, X)K(X, X)^{-1}y, \quad (8)$$

$$\Sigma = K(X^*, X^*) - K(X^*, X)K(X, X)^{-1}K(X, X^*). \quad (9)$$

Through the above series of calculations, the GP can predict the output corresponding to the x^* .

B. Student's-T process

STP is a function distribution of an infinite set of random variables subject to multivariate Student's-T distribution, which is an extension of GP. We describe the Student's-T distribution in this way [23]:

$$T(\mu, \Sigma, \nu) = \frac{\Gamma((\nu+n)/2)}{\Gamma(\nu/2)\nu^{n/2}\pi^{n/2}|\Sigma|^{1/2}} \cdot \left(1 + \frac{1}{\nu}(y-\mu)^T \Sigma^{-1}(y-\mu)\right)^{-(\nu+n)/2}. \quad (10)$$

In the above equation, n is the dimension of the Student's-T distribution, μ is the mean vector, Σ is the correlation matrix, ν is the degree of freedom and $\nu > 2$:

$$E[(y-\mu)(y-\mu)^T] = \frac{\nu}{\nu-2}\Sigma. \quad (11)$$

STP includes mean function $\mu(x)$, kernel function $k(x, x')$ and degree of freedom ν , and they also determine STP properties. If $x, x' \in R^d$ is any random variable, STP can be given by:

$$f(x) \sim STP(m(x), k(x, x'), \nu). \quad (12)$$

If the degrees of freedom ν increase infinitely and finally converge to infinity, the multivariate Student's-T distribution will become a multivariate Gaussian distribution, which has the same mean and correlation function.

In STP, the prior expected value of each position x is defined by the mean function $\mu(x)$. The covariance between the values of x and x_0 at any two positions is represented by the kernel function, and then the joint probability distribution of a finite subset of positions can be expressed as:

$$p(y|x) = T(\mu, \Sigma, \nu)(y) = T\left(\mu, \frac{\nu-2}{\nu}K, \nu\right)(y). \quad (13)$$

In the above equation, μ represents means vector, $\mu_i = \mu(x_i)$ $\ell \nu$ is the degree of freedom, K is the kernel matrix $K_{i,j} = k(x_i, x_j)$.

Given a set of samples $D = [(x_1, y_1), (x_2, y_2), (x_3, y_3), \dots]$, a posteriori of STP is given by:

$$p(y|x, D) = T\left(\hat{\mu}, \frac{\nu-2}{\nu}\hat{K}, \hat{\nu}\right)(y), \quad (14)$$

where

$$\hat{\mu} = K_{x,x}K_{x,x}^{-1}\tilde{y}, \quad (15)$$

$$\hat{K} = \frac{\nu-2 + \tilde{y}^T K_{x,x}^{-1}\tilde{y}}{\nu-2 + |D|}(K_{x,x} - K_{x,x}K_{x,x}^{-1}K_{x,x}), \quad (16)$$

$$\hat{\nu} = \nu + |D|. \quad (17)$$

Generally, the kernel of the square index is selected as kernel function [24] and is given by:

$$K_{SE}(x, x') = s_f^2 \exp\left(-\frac{\|x-x'\|^2}{2\ell^2}\right), \quad (18)$$

where s_f^2 is the signal variance and can also be the output scale amplitude, and the parameter ℓ is the input (length or time) scale.

The combination of equation (14) and the kernel function shows that the posterior covariance of STP is dependent on not only the test observations but also the training observations [25]. Therefore, as a surrogate model, STP has more flexible post-verification difference. In addition, using the same method as the GP, its hyperparameter can be estimated by the maximum marginal likelihood. The form of its negative logarithmic likelihood function can be given by:

$$\begin{aligned} L(\theta) &= -\log p(y|x, \theta) \\ &= \frac{N}{2} \log((\nu-2)\pi) + \frac{1}{2} \log |K_\theta| \\ &\quad - \log \Gamma\left(\frac{\nu+N}{2}\right) + \log \Gamma\left(\frac{\nu}{2}\right) \\ &\quad + \frac{\nu+N}{2} \log\left(1 + \frac{\beta}{\nu-2}\right) \end{aligned} \quad (19)$$

III. THE PROPOSED MODEL

The consensus STP, named C-STP, is proposed in this paper, as shown in Fig. 1, which is constructed by multiple individual STPs that map the physical parameter X of an antenna to the output parameter Y , such as resonant frequency. The nonlinear transform $y = f_{STP}(x)$, where $x = [x_1 x_2 \dots x_l]$ $y = [y_1 y_2 \dots y_n]$ implements the mapping, where l, n is the length of x, y .

For the STP used in this paper, the ARD series square index kernel (20) is selected, and the hyperparameter is optimized through nonlinear optimization method. STP's degree of freedom ν , noise variance σ_f^2 , signal variance s_f^2 , and kernel function hyperparameter ℓ are all targets that need to be optimized. The optimization process is shown in Fig. 2. Taking the negative log-marginal likelihood function of STP as the objective function, gradient-based numerical optimization techniques including the conjugate gradient method or other intelligent optimization algorithms are used to calculate the minimum value of the negative log-marginal likelihood function and obtain the final hyperparameter. When a new observation is given, the output can be accurately predicted:

$$K_{SEard}(x, x') = s_f^2 \exp\left(-\frac{(x-x')^T \Theta^{-1} (x-x')}{2}\right), \quad (20)$$

where Θ is the element component $\{\ell_i^2\}_{i=1}^p$, which represents the length scale of each corresponding input dimension.

A. Consensus of STP

Training STP to predict y as accurately as possible for any input x requires non-linear optimization method to find the minimum value of the negative log marginal likelihood function and determines the value of the hyperparameter. The training process can start with random values of the hyperparameter or some predefined

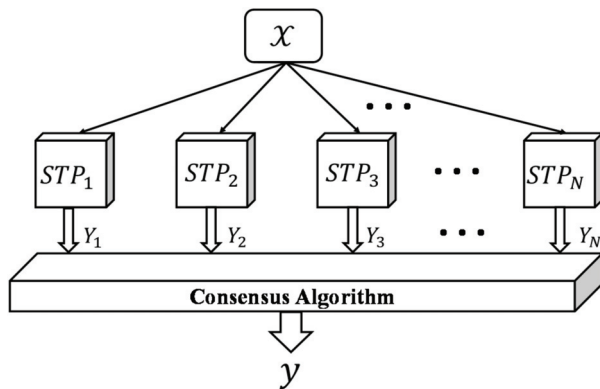


Fig. 1. Structure diagram of consistent Student's-T Process model.

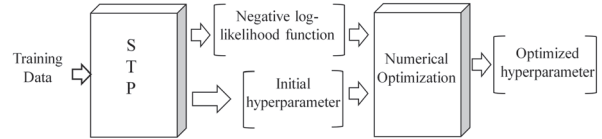


Fig. 2. STP hyperparameter optimization flow chart.

values. These values, along with the optimization algorithm used to adjust the hyperparameters, determine the final STP. If a random method is used, the final result is random, that is, each training will produce a slightly different STP instance. In theory, training might produce the same STP, but we don't observe it in the experiments.

If only one STP is trained for antenna frequency modelling, even if it is well trained, its output results may have uncertainties related to the STP training. The effectiveness of the trained STP result depends on its kernel functions, hyperparameters, training programs and data set. To improve the effectiveness of independently trained STP results and make them more accurate, we use multiple STP instances instead of one STP, as shown in Fig. 1. This topology is called consensus STP, referred to as C-STP in this paper, and similar methods have been used in previous studies in medicine, EM and computer science [26–28]. The core idea of consensus STP is to use multiple STPs simultaneously by providing an identical training task to each STP separately. If the input is same for all STPs, then the consensus algorithm is performed for the output of all STPs, i.e. y_1, y_2, \dots, y_N , where N is the total number of STPs. The consensus module can give the final output as shown in Fig. 1, and the threshold determines whether all the results are consistent. Usually, x and y can be either real set of data, which is common in antenna design, or discrete set data, and the C-STP can be used for both types of data. There are some methods to implement the consensus algorithm, including majority voting, arithmetic or other mean algorithms. The decision is mostly influenced by the tasks specifications and the outputs characteristics.

The training process of multiple STPs can be performed in parallel because all STPs are independent of each other, and there is no data exchange. Therefore, the C-STP approach is well suited for applications on multi-core computing architectures. Typically, the STPs may have the same or different kernel functions and hyperparameters, but all STPs must perform the same training task.

B. Consensus algorithm

In the whole work, we use multiple training sets to train STP randomly. The training process is repeated for N times, therefore N different STPs can be generated.

The consistency algorithm is to calculate the arithmetic mean y_{avg} from the output of all the STPs.

$$y_{avg} = \frac{1}{N} \sum_{k=1}^M y_k, \quad (21)$$

we can find the output $y_{k_{max}}$ that deviates the most from y_{avg} , i.e.

$$|y_k - y_{avg}| \leq |y_{k_{max}} - y_{avg}| \quad k = 1, 2, \dots, N. \quad (22)$$

Then we exclude the output of the $k_{max}th$ STP and calculate the arithmetic mean of all other STPs as:

$$y = \frac{1}{N-1} \sum_{\substack{k=1 \\ k \neq k_{max}}}^N y_k. \quad (23)$$

In addition, for each pair of STP outputs, y_p and y_q , $p, q = 1, 2, \dots, N, p \neq k_{max}$ and $q \neq k_{max}$, if (24) is satisfied, we believe that the two STPs are consistent.

$$|y_p - y_q| \leq \varepsilon, \quad (24)$$

where ε is a pre-defined threshold. In this case, it is the final output of the C-STP. Otherwise, it is no consensus, and the C-STP cannot predict the output correctly. In this case, the output is computed by other methods. In general, the ε is set according to the problem we are facing, and it is different depending on the problem.

When it is no consensus, we adopt the aggregation method proposed by Goel et al. [29] to construct the final result. This method is simple in operation and has good usability, especially with high modelling efficiency. The weight factor solution method of each model is as follows:

$$w_i^* = (E_i + \alpha E_{avg})^\beta, w_i = \frac{w_i^*}{\sum_i w_i^*}, \quad (25)$$

$$E_{avg} = \frac{\sum_{i=1}^N E_i}{N}, \alpha = 0.05, \beta = -1. \quad (26)$$

The parameters α and β are used to measure the importance of the average model and a single approximate model. Experiments show that $\alpha = 0.05, \beta = -1$ can obtain an accurate consensus model for most problems. E_i is the global error of the i th approximate model, and the value can be determined by the specific error index used.

The consensus algorithm allows a STP to predict the output inaccurately, while the proposed C-STP can give a more accurate output because the algorithm eliminates the worst predictions. On the flip side, if the outputs of all STPs predictions are within ε , excluding one result does not affect the final output. Therefore, compared with the simple arithmetic mean of independent STP output, the consistency algorithm is more accurate. The proposed consensus algorithm meets $N \geq 3$.

The pseudo-program code for the proposed algorithm is shown in Algorithm 1.

Algorithm 1

Input: Data set, $x = [x_1, x_2 \dots x_l]$;

Output: Data set, $y = [y_1, y_2 \dots y_n]$

Process:

- 1: **parfor** $i = 1, 2, \dots, N$
 - 2: Numerical optimization technique is used to optimize STP hyperparameter and train individual STP;
 - 3: A posterior prediction mean μ_{i-1} and posterior difference σ_{i-1}^2 of x_i are obtained;
 - 4: $y_N \leftarrow STP \leftarrow x_i$;
 - 5: $y = [y_1, y_2 \dots y_N]$;
 - 6: **end parfor**
 - 7: $y_{avg} \leftarrow$ Calculated arithmetic average from the outputs of all STPs;
 - 8: Find the output $y_{k_{max}}$ that deviates from y_{avg} ;
 - 9: $|y_k - y_{avg}| \leq |y_{k_{max}} - y_{avg}| \quad k = 1, 2, \dots, N$;
 - 10: $y \leftarrow$ The calculated arithmetic mean of the remaining STP by excluding the $k_{max}th$ STPs output;
 - 11: Define a threshold ε in advance, $p, q = 1, 2, \dots, N, p \neq k_{max}$ and $q \neq k_{max}$;
 - 12: **if** ($|y_p - y_q| \leq \varepsilon$) **then**
 - 13: The STPs are considered to be consensus and get the final result y ;
 - 14: **else**
 - 15: $E_{avg} = \sum_{i=1}^N E_i / N, \alpha = 0.05, \beta = -1$;
 - 16: $w_i^* = (E_i + \alpha E_{avg})^\beta, w_i = w_i^* / \sum_i w_i^*$;
 - 17: $y = w_1 y_{STP_1} + w_2 y_{STP_2} + \dots + w_N y_{STP_N}$;
 - 18: **end if**
-

IV. EXPERIMENTS

A. Single STP regression

First, a single STP is trained and tested. Ten regression data sets are selected from the database [30] of the University of California, Irvine (UCI). These data sets have different capacities, which can verify the effectiveness of STP. Experimental results from STP and related parameters for these 10 regression problems are shown in Table 1, Table 2 and Fig. 3. The results obtained by SVM [31], Least Squares Support Vector Machine (LSSVM) [32], ELM [33], GP [34] and other classical models are selected to compare with STP, verifying the effectiveness of the STP. Root mean square error (RMSE) is adopted as the performance evaluation index to measure the prediction error of different models. Table 2 shows the prediction results of each model, and the best ones for different problems are shown in bold.

$$RMSE = \sqrt{\frac{1}{N} \sum_{i=1}^N (y_i - Y_i)^2}, \quad (27)$$

where y_i is the real value, Y_i is the predicted value, and is the total number of samples.

Table 1: Details of data sets

Data	Train Samples	Test Samples	Input Feature
Strike	416	209	6
Pyrim	49	25	27
Housing	337	169	13
Weather Izmir	974	487	9
Abalone	2784	1393	8
Quake	1452	726	3
Cleveland	202	101	13
Mortgage	699	350	15
Bodyfat	168	84	14
Basketball	64	32	4

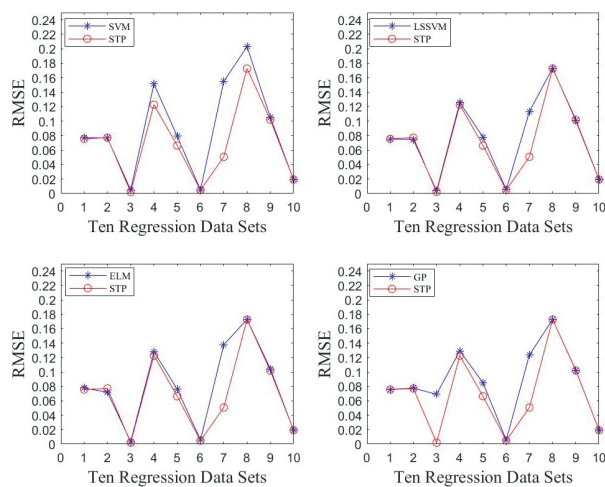


Fig. 3. Comparison of different models with STP.

It can be seen that the STP used in this paper outperforms other models in at least 7 out of 10 datasets. Moreover, it outperforms anyone of the classical models

in at least 9 out of 10 datasets. Therefore, the STP has good predictive ability.

B. Antennas resonant frequency

To gain insight into the performance of the proposed C-STP and demonstrate its effectiveness, we generate 10 STPs for the following experiments. Since there are multiple groups of data in the test set, each STP prediction output will also have multiple groups. In order to unify the calculation, we use the average difference between the predicted result and the true value as output, so that each STP will only have one predicted result, and then it is compared in pairs to compute the consistency. From several experiments, the threshold setting $\epsilon = 0.5$ for CMSA and $\epsilon = 1$ for RMSA are considered reasonable. Of course, the number of STPs in the C-STP as well as the threshold are determined according to the problem.

The CMSA [35] selected in this paper is shown in Fig. 4, and the proposed C-STP is used to predict its resonant frequency. The input variables of the CMSA are a, h, ϵ_r , where a is the radius of the circular patch,

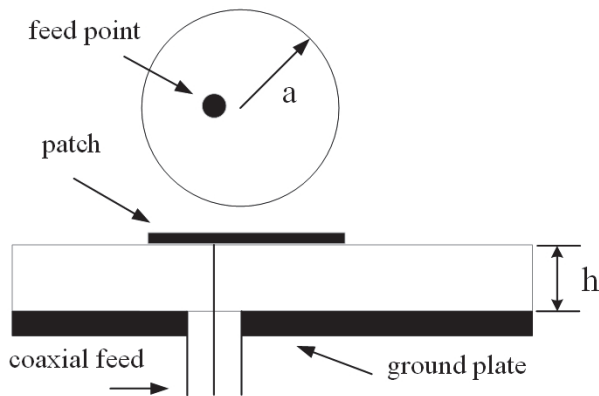


Fig. 4. Schematic diagram of the CMSA.

Table 2: Error of different models

Data Set	SVM	LSSVM	ELM	GP	STP
Strike	0.1053	0.1007	0.1043	0.1023	0.1020
Pyrim	0.15497	0.1133	0.1376	0.1236	0.0507
Housing	0.0792	0.0780	0.0762	0.0849	0.0663
Weather Izmir	0.0190	0.0191	0.0191	0.0194	0.0193
Abalone	0.0773	0.0756	0.0777	0.0758	0.0756
Quake	0.2029	0.1733	0.1729	0.1728	0.1728
Cleveland	0.1514	0.1256	0.1281	0.1293	0.1227
Mortgage	0.0049	0.0053	0.0057	0.0056	0.0048
Bodyfat	0.0049	0.0038	0.0033	0.0690	0.0020
Basketball	0.0767	0.0744	0.0719	0.0776	0.0772

h is the thickness of the dielectric layer, and ϵ_r is the relative dielectric constant, and the output is the resonant frequency f corresponding to each group of samples. There are 20 groups of experimental data, among which 16 groups are selected as the training set, and the remaining 4 groups labelled with * symbol are selected as the test set, as shown in Table 3. At the same time, we also select four different modelling methods, including BP, SVM, GP and STP, to compare with the proposed C-STP. The test results are shown in Table 4 and Fig. 5. The evaluation metric is the average percentage error (APE), i.e.

$$APE = \frac{1}{N} \sum_{i=1}^N \frac{|Y_i - y_i|}{|y_i|} \times 100, \quad (28)$$

where y_i is the real value, Y_i is the predicted value, and is the total number of samples.

As shown in Table 4 and Fig. 5, the prediction accuracy of the proposed C-STP is 84.96% higher than that

Table 3: Samples of the CMSA for the proposed C-STP method

Number	a/cm	h/cm	ϵ_r	f/MHz
1*	6.8	0.08	2.32	835
2	6.8	0.159	2.32	829
3	2	0.2350	4.55	2003
4	5	0.159	2.32	1128
5	3.8	0.1524	2.49	1443
6	4.85	0.318	2.52	1099
7*	3.493	0.3175	2.5	1510
8	1.27	0.0794	2.59	4070
9	3.493	0.1588	2.5	1570
10	4.95	0.235	4.55	825
11	3.975	0.235	4.55	1030
12	2.99	0.235	4.55	1360
13*	6.8	0.318	2.32	815
14	1.04	0.235	4.55	3750
15	0.77	0.235	4.55	4945
16	1.15	0.15875	2.65	4425
17	1.07	0.15875	2.65	4723
18	0.96	0.15875	2.65	5524
19	0.74	0.15875	2.65	6634
20*	0.82	0.15875	2.65	6074

Table 4: Test results of different methods for the CMSA

f/MHz	BP	SVM	GP	STP	Proposed
835	618	837.6	825.4	829.7	829
1510	1313	1462.7	1547.2	1553.8	1549
815	831.9	779.9	814.6	829	829
6074	6018	6136.4	6297.9	6297.9	6155.9
APE(%)	10.3012	2.2629	1.8340	1.6718	1.5498

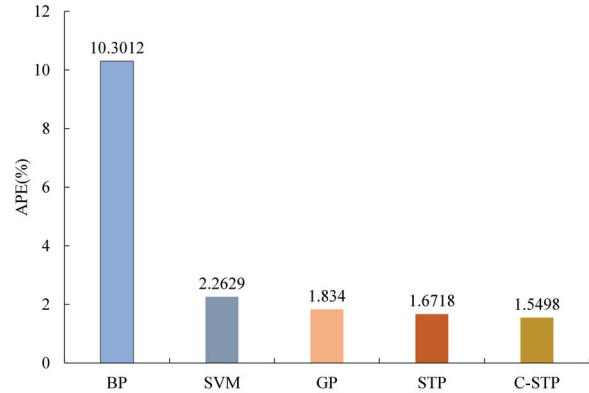


Fig. 5. APE of different models for the CMSA.

of BP, 31.51% higher than that of SVM, 15.50% higher than that of GP, and 7.28% higher than that of STP. The APE of the proposed C-STP is only 1.5498%, showing its strong generalization performance and effectiveness.

In the following, the resonant frequency of RMSA [36, 37], shown in Fig. 6, is selected for testing the proposed C-STP. The antenna consists of a radiating element, a dielectric layer and a ground plane, and W , L ,

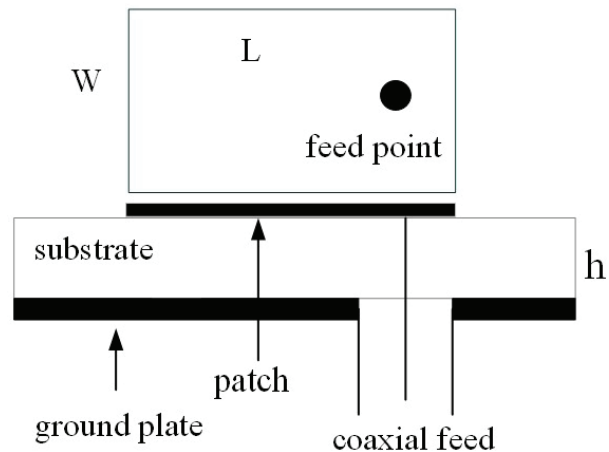


Fig. 6. Schematic diagram of the RMSA.

h , ϵ_r represent the corresponding width, length, thickness of dielectric substrate and relative dielectric constant, respectively. A total of 33 groups of samples are shown in Table 5, which is divided into two parts, one as training

Table 5: Samples of the RMSA for the proposed C-STP method

Number	W/cm	L/cm	h/cm	ϵ_r	f/MHz
1*	0.790	1.185	0.017	2.22	8450
2	0.910	1.000	0.127	10.20	4600
3	2.000	2.500	0.079	2.22	3970
4	0.850	1.290	0.017	2.22	7740
5	1.063	1.183	0.079	2.25	7730
6*	1.810	1.960	0.157	2.33	4805
7	1.720	1.860	0.157	2.33	5060
8	1.170	1.280	0.300	2.50	6570
9	0.987	1.450	0.450	2.55	6070
10	0.776	1.080	0.330	2.55	8000
11	0.790	1.620	0.550	2.55	5990
12*	1.337	1.412	0.200	2.55	5800
13	0.905	1.018	0.300	2.50	7990
14	1.500	1.621	0.163	2.55	5600
15	1.120	1.200	0.242	2.55	7050
16	1.530	1.630	0.300	2.50	5270
17	1.270	1.350	0.163	2.55	6560
18*	1.375	1.580	0.476	2.55	5100
19	0.814	1.440	0.476	2.55	6380
20	1.403	1.485	0.252	2.55	5800
21	0.790	1.255	0.400	2.55	7134
22	0.783	2.300	0.854	2.55	4600
23*	1.000	1.520	0.476	2.55	5820
24	0.883	2.676	1.000	2.55	3980
25	1.265	3.500	1.281	2.55	2980
26	1.200	1.970	0.626	2.55	4660
27	0.974	2.620	0.952	2.55	3980
28	0.920	3.130	1.200	2.55	3470
29*	1.256	2.756	0.952	2.55	3580
30	1.080	3.400	1.281	2.55	3150
31	1.020	2.640	0.952	2.55	3900
32	0.777	2.835	1.100	2.55	3900
33*	1.030	3.380	1.281	2.55	3200

Table 6: Test results of different methods for the RMSA

f_{ME} /GHz	DBD	BP	EDBD	PTS	GP	STP	Proposed
8450	8226	8233.1	8328.2	8148.6	8041	8289.1	8290.2
4805	4684.8	4703.3	4699.2	4879	4807	4860.3	4861.5
6200	6142.6	6147.2	6176.6	6205.7	6164	6192.3	6191.5
5100	5293.2	5291.4	5311.8	5191.4	5112	5047.2	5076.5
5820	5918	5924.5	5931	5780.3	5876	5865.7	5868.5
3580	3655.7	3644.6	3659.8	3685.2	3590	3578.5	3582.4
3200	3184.7	3178	3230.3	3167	3183	3206.4	3205.7
APE (%)	2.020	1.939	1.894	1.663	1.0716	0.7559	0.6778

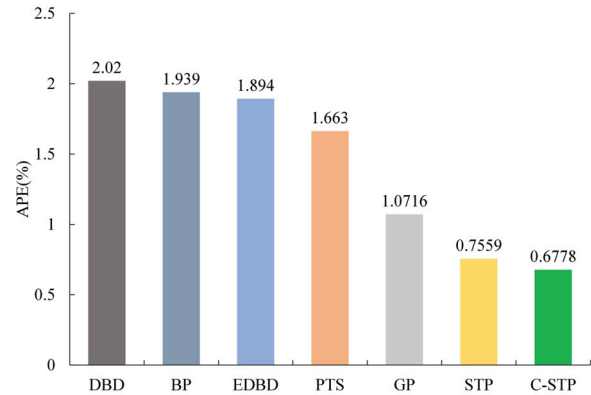


Fig. 7. APE of different models for the RMSA.

set and the other as a test set. A total of 26 groups of samples are randomly selected as the training set, and the remaining 7 groups are marked with * symbol as the test set. The input are W , L , h , ϵ_r , and the resonant frequency f is used as the output. The evaluation metric for the experiment is still the APE.

Six modelling methods including Delta-bar-delta (DBD) [38], BP [38], Extended Delta-bar-delta (EDBD) [38], Parallel Tabu Search (PTS) [39], GP [34], and STP are selected as comparison. The test results are shown in Table 6 and Fig. 7. It can be seen that the predicted APE of the proposed C-STP is 0.6778% and less than that of the other six modelling methods, which is 10.33% higher than STP, 35.24% higher than GP, and 58.27% higher than PTS. It is 63.36% higher than the EDBD method, 64.2% higher than the BP method, and 65.64% higher than the DBD method. Therefore, the C-STP has excellent generalization performance for the RMSA.

V. CONCLUSION

This paper proposes an algorithm named Consistent Student's-T Process (C-STP), aiming to improve the accuracy and efficiency of antenna optimization by exploiting the consistent results of multiple STP

instances and reducing the uncertainty of independently trained STP results. The core idea of the proposed C-STP is to process multiple independently trained STP results through a consistent algorithm to improve the possible inaccuracy problem when using only one STP. The experimental results show that the proposed C-STP algorithm has a clear advantage over existing algorithms in modelling and optimizing the resonant frequencies of two microstrip antennas in accuracy. In addition, the proposed algorithm can overcome the limitations of small sample data and achieve more reliable modelling and optimization results by consistent results from multiple STP instances. Similarly, the proposed method can also be easily applied to the modelling and optimization of other electromagnetic devices.

In practical applications, the optimization of antennas has to take into account the limited time and available computer resources. The proposed C-STP model uses imperfectly trained STPs for the optimization, as well as the estimation of output uncertainty through a consistency approach. We also find that the predictive ability of the model is strongly related to the choice of kernel function and individual network models, and we will continue to investigate in the following study. The proposed method is less suitable for higher dimensionality and larger data volume EM models, which require a large amount of time for training, resulting in low-cost performance.

ACKNOWLEDGMENT

This work was supported by the Natural Science Foundation of Guangdong Province of China under Grant No.2023A1515011272, the Tertiary Education Scientific research project of Guangzhou Municipal Education Bureau of China under No.202234598, the special project in key fields of Guangdong Universities of China under No.2022ZDZX1020, and the scientific research capacity improvement project of key developing disciplines in Guangdong Province of China under No.2021ZDJS057. Corresponding to Yubo Tian, Xuefeng Ren and Yubo Tian are co-first authors.

REFERENCES

- [1] Z. Jiang, Y. Zheng, X. Xuan, and N. Nie, "A novel ultra-wideband wide-angle scanning sparse array antenna using genetic algorithm," *Applied Computational Electromagnetics Society (ACES) Journal*, vol. 38, no. 2, pp. 100-108, 2023.
- [2] V. Grout, M. O. Akinsolu, B. Liu, P. I. Lazaridis, K. K. Mistry, and Z. D. Zaharis, "Software solutions for antenna design exploration: A comparison of packages, tools, techniques, and algorithms for various design challenges," *IEEE Antennas and Propagation Magazine*, vol. 61, no. 3, pp. 48-59, 2019.
- [3] L.-Y. Xiao, W. Shao, F.-L. Jin, B.-Z. Wang, and Q. H. Liu, "Inverse artificial neural network for multiobjective antenna design," *IEEE Transactions on Antennas and Propagation*, vol. 69, no. 10, pp. 6651-6659, 2021.
- [4] L.-Y. Xiao, W. Shao, X. Ding, Q. H. Liu, and W. T. Joines, "Multigrade artificial neural network for the design of finite periodic arrays," *IEEE Transactions on Antennas and Propagation*, vol. 67, no. 5, pp. 3109-3116, 2019.
- [5] A. Uluslu, "Application of artificial neural network base enhanced MLP model for scattering parameter prediction of dual-band helical antenna," *Applied Computational Electromagnetics Society (ACES) Journal*, vol. 38, no. 5, pp. 316-324, 2023.
- [6] A. Ibrahim, H. Abutarboush, A. Mohamed, M. Fouad, and E. El-Kenawy, "An optimized ensemble model for prediction the bandwidth of metamaterial antenna," *CMC-Computers, Materials & Continua*, vol. 71, no. 1, pp. 199-213, 2022.
- [7] D. Shi, C. Lian, K. Cui, Y. Chen, and X. Liu, "An intelligent antenna synthesis method based on machine learning," *IEEE Transactions on Antennas and Propagation*, vol. 70, no. 7, pp. 4965-4976, 2022.
- [8] J. Nan, H. Xie, M. Gao, Y. Song, and W. Yang, "Design of UWB antenna based on improved deep belief network and extreme learning machine surrogate models," *IEEE Access*, vol. 9, pp. 126541-126549, 2021.
- [9] S. Han and Y. Tian, "Structure parameter estimation method for microwave device using dimension reduction network," *International Journal of Machine Learning and Cybernetics*, vol. 14, no. 4, pp. 1285-1301, 2023.
- [10] L.-Y. Xiao, W. Shao, S.-B. Shi, and Z.-B. Wang, "Extreme learning machine with a modified flower pollination algorithm for filter design," *Applied Computational Electromagnetics Society (ACES) Journal*, vol. 33, no. 03, pp. 279-284, 2021.
- [11] K. Sharma and G. P. Pandey, "Efficient modelling of compact microstrip antenna using machine learning," *AEU-International Journal of Electronics and Communications*, vol. 135, p. 153739, 2021.
- [12] X. Chen, Y. Tian, T. Zhang, and J. Gao, "Differential evolution based manifold Gaussian process machine learning for microwave Filter s parameter extraction," *IEEE Access*, vol. 8, pp. 146450-146462, 2020.
- [13] J. Gao, Y. Tian, X. Zheng, and X. Chen, "Resonant frequency modeling of microwave antennas using

- Gaussian process based on semisupervised learning,” *Complexity*, vol. 2020, p. 12, 2020.
- [14] F. Pang, J. Ji, J. Ding, W. Zhang, D. Xu, and M. Zhou, “Analyze the crosstalk of multi-core twisted wires and the effect of non-matched impedance based on BSAS-BPNN algorithm,” *Applied Computational Electromagnetics Society (ACES) Journal*, vol. 38, no. 2, pp. 80-90, 2023.
- [15] S. Han, Y. Tian, W. Ding, and P. Li, “Resonant frequency modeling of microstrip antenna based on deep kernel learning,” *IEEE Access*, vol. 9, pp. 39067-39076, 2021.
- [16] A. O’Hagan, “On outlier rejection phenomena in Bayes inference,” *Journal of the Royal Statistical Society Series B: Statistical Methodology*, vol. 41, no. 3, pp. 358-367, 1979.
- [17] A. Shah, A. Wilson, and Z. Ghahramani, “Student-t processes as alternatives to Gaussian processes,” in *Artificial Intelligence and Statistics*, pp. 877-885, PMLR, 2014.
- [18] A. Solin and S. Särkkä, “State space methods for efficient inference in Student-t process regression,” *Artificial Intelligence and Statistics*, vol. 38, pp. 885-893, PMLR, 2015.
- [19] Q. Tang, L. Niu, Y. Wang, T. Dai, W. An, J. Cai, and S.-T. Xia, “Student-t process regression with student-t likelihood,” in *IJCAI*, pp. 2822-2828, 2017.
- [20] Z. Chen, B. Wang, and A. N. Gorban, “Multivariate Gaussian and student-t process regression for multi-output prediction,” *Neural Computing and Applications*, vol. 32, pp. 3005-3028, 2020.
- [21] R. B. Gramacy and H. K. H. Lee, “Bayesian treed Gaussian process models with an application to computer modeling,” *Journal of the American Statistical Association*, vol. 103, no. 483, pp. 1119-1130, 2008.
- [22] C. E. Rasmussen, “Gaussian processes in machine learning,” *Summer School on Machine Learning*, pp. 63-71, Springer, 2003.
- [23] B. D. Tracey and D. Wolpert, “Upgrading from Gaussian processes to student’s-t processes,” in *2018 AIAA Non-Deterministic Approaches Conference*, p. 1659, 2018.
- [24] J. Vanhatalo, P. Jylänki, and A. Vehtari, “Gaussian process regression with student-t likelihood,” *Advances in Neural Information Processing Systems*, vol. 22, 2009.
- [25] Q. T. Y. Wang and S.-T. Xia, “Student-t process regression with dependent student-t noise,” in *ECAI 2016: 22nd European Conference on Artificial Intelligence*, vol. 29 of *ECAI’16*, pp. 82-89, IOS Press, NLD, 2016.
- [26] R. K. Singh, A. Choudhury, M. Tiwari, and R. Shankar, “Improved Decision Neural Network (IDNN) based consensus method to solve a multi-objective group decision making problem,” *Advanced Engineering Informatics*, vol. 21, no. 3, pp. 335-348, 2007.
- [27] D. Wu, K. Gong, K. Kim, X. Li, and Q. Li, “Consensus neural network for medical imaging denoising with only noisy training samples,” in *International Conference on Medical Image Computing and Computer-Assisted Intervention*, pp. 741-749, Springer-Verlag, 2019.
- [28] Z. Ž. Stanković, D. I. Olčan, N. S. Dončov, and B. M. Kolundžija, “Consensus deep neural networks for antenna design and optimization,” *IEEE Transactions on Antennas and Propagation*, vol. 70, no. 7, pp. 5015-5023, 2021.
- [29] T. Goel, R. T. Haftka, W. Shyy, and N. V. Queipo, “Ensemble of surrogates,” *Structural and Multidisciplinary Optimization*, vol. 33, pp. 199-216, 2007.
- [30] C. L. Blake, “UCI repository of machine learning databases,” <http://www.ics.uci.edu/~mllearn/MLRepository.html>, 1998.
- [31] C.-C. Chang and C.-J. Lin, “LIBSVM: A library for support vector machines,” *ACM Transactions on Intelligent Systems and Technology (TIST)*, vol. 2, no. 3, pp. 1-27, 2011.
- [32] J. S. Armstrong and F. Collopy, “Error measures for generalizing about forecasting methods: Empirical comparisons,” *International Journal of Forecasting*, vol. 8, no. 1, pp. 69-80, 1992.
- [33] G.-B. Huang, Q.-Y. Zhu, and C.-K. Siew, “Extreme learning machine: a new learning scheme of feedforward neural networks,” in *2004 IEEE International Joint Conference on Neural Networks (IEEE Cat. No.04CH37541)*, vol. 2, pp. 985-990, 2004.
- [34] M. Ebden, “Gaussian processes: A quick introduction,” arXiv preprint arXiv:1505.02965, 2015.
- [35] Ş. Sağıroğlu, K. Güney, and M. Erler, “Resonant frequency calculation for circular microstrip antennas using artificial neural networks,” *International Journal of RF and Microwave Computer-Aided Engineering*, vol. 8, no. 3, pp. 270-277, 1998.
- [36] M. Kara, “Closed-form expressions for the resonant frequency of rectangular microstrip antenna elements with thick substrates,” *Microwave and Optical Technology Letters*, vol. 12, no. 3, pp. 131-136, 1996.
- [37] M. Kara, “The resonant frequency of rectangular microstrip antenna elements with various substrate thicknesses,” *Microwave and Optical Technology Letters*, vol. 11, no. 2, pp. 55-59, 1996.

- [38] K. Guney, S. Sagioglu, and M. Erler, "Generalized neural method to determine resonant frequencies of various microstrip antennas," *International Journal of RF and Microwave Computer-Aided Engineering*, vol. 12, no. 1, pp. 131-139, 2002.
- [39] S. Sagioglu and A. Kalinli, "Determining resonant frequencies of various microstrip antennas within a single neural model trained using parallel tabu search algorithm," *Electromagnetics*, vol. 25, no. 6, pp. 551-565, 2005.



Xuefeng Ren studying in Jiangsu University of science and technology, master's degree, research direction: intelligent optimization algorithm, intelligent electromagnetic optimization.



Yubo Tian was born in Tieling, Liaoning Province, China, in 1971. He received the Ph.D. degree in radio physics from the Department of Electronic Science and Engineering, Nanjing University, Nanjing, China. From 1997 to 2004, he was with the Department of Information Engineering, Shenyang University, Shenyang, China. From 2005 to 2020, he was with the School of Electronics and Information, Jiangsu University of Science and Technology, Zhenjiang, China. He is currently with the School of Information and Communication Engineering, Guangzhou Maritime University, Guangzhou, China. His current research interest is Machine Learning methods and their applications in electronics and electromagnetics.



Qing Li was Born in Anqing, Anhui Province, China, studying in Jiangsu University of science and technology, master's degree, research direction: intelligent optimization algorithm, intelligent electromagnetic optimization.



Hao Fu studying in Jiangsu University of science and technology, master's degree, research direction: intelligent optimization algorithm, intelligent electromagnetic optimization.

Multi-polarized Reconfigurable Antenna with Ground Plane Slot and Capacitance Feeding for UAV-to-everything Communications

Seong-Hyeop Ahn¹, Yu-Seong Choi², Mohamed Elhefnawy^{1,3}, and Wang-Sang Lee¹

¹Department of Electrical Engineering, Gyeongsang National University (GNU)
B405-401501, Jinju-daero, Jinju-si Gyeongnam, 52828, Republic of Korea
dksak2115@gnu.ac.kr, wsang@gnu.ac.kr

²Korea Aerospace Industries (KAI), Ltd
78, Gongdan 1-ro, Sanam-myeon, Sacheon-si
Gyeongnam, 52529, Republic of Korea

³Department of Electrical Engineering
Faculty of Engineering, October 6 University, Egypt
mmmelhefnawy.eng@o6u.edu.eg

Abstract – This paper proposes a polarized reconfigurable antenna for unmanned aerial vehicles (UAVs) with flexible UAV-to-Everything (U2X) communications through a reduction of polarization loss. It operates at 2.45 GHz and consists of a square patch antenna, a capacitance feed, a ground surface slot, and a reconfigurable feeding network. The reconfigurable feeding network has dual polarization (linear, circular) depending on the configuration of the feeding network. The dual linear polarization reconfigurable feeding network configuration consists of a single-pole double-throw (SPDT) switch, a 50-ohm microstrip line, and a low-temperature co-fired ceramic (LTCC) 90-degree hybrid coupler. This was added to the circuit to form a double circular polarization reconfigurable feeding network. The proposed antenna has a miniaturized size ($0.389\lambda_o \times 0.389\lambda_o \times 0.005\lambda_o$), and is lightweight (12.2 g), making it suitable for low-height flight. Furthermore, it has maximum gains of 6.6 dBi and 7.2 dBi, in addition to an efficiency of 82%, and a 10 dB bandwidth of 4.5% (2.38-2.49 GHz). Therefore, the proposed antenna covers all UAV control links, video, and telemetry frequency bands (2.38-2.485 GHz).

Index Terms – Capacitance feed, ground surface slot, polarization-reconfigurable antenna, UAV-to-Everything communications.

I. INTRODUCTION

The unmanned aerial vehicles (UAVs) industry, one of the core challenges of the Fourth Industrial Revolution, has high marketability and economic value. It is expected to grow by \$21.8 billion by 2027, based on

the benefits of its applications in various fields such as surveillance/research, hobby/leisure, imaging, and life-saving [1]. Based on these values, research and development of communication platforms for UAVs are also rapidly growing and changing in line with this. Unlike conventional terrestrial wireless communication environments, the UAV communication environment has specific requirements for operation at a certain altitude, so it must be accompanied by flexible UAV-to-Everything (U2X) communication technology that can perform various tasks in different ways. Therefore, the implementation of an antenna with multiple polarizations is essential to reduce polarization loss. The antennas for U2X communications should have many characteristics, including compact size, low profile, and light weight. Additionally, they should cover the frequency band for UAV communication. There have been many research papers focused on the design of antennas for unmanned aerial vehicles. For example, single-polarized antennas without reconfigurability have been studied in [2–4]. The use of single-polarized antennas with U2X communication systems could degrade their performance due to cross-polarization loss. Accordingly, research on polarization-reconfigurable antennas is continuing to reduce polarization losses in wireless communication systems [5–6]. The polarization-reconfigurable antenna has a good gain and impedance bandwidth performance, despite being relatively large in size [7–11]. For the miniaturization of the antenna, a patch antenna with a slot was used in [12–13]. But [12] and [13] have a narrow bandwidth of approximately 7%. In [14–15], researchers have studied a meta-surface antenna that can rotate mechanically and a ring slot antenna that offers

both linear and circular polarization. The meta-surface antenna in [14] has a large size but provides wide bandwidth and high gain. On the other hand, the ring slot antenna in [15] has a small size and wide bandwidth, but it has low gain. In [16], the reconfigurable patch antenna with PIN diodes has both linear and circular polarization but the antenna has narrow impedance and axial ratio bandwidths. [17] investigated the design of an antenna that includes four parasitic patches and two varactor diodes on each patch. By reconfiguring this antenna, it is possible to achieve dual polarization with two beams for each polarization. However, manufacturing this antenna is challenging due to its complex structure, and integrating it as an aerodynamic component to be attached to UAVs is difficult.

In this paper, we propose a compact, multi-polarized, reconfigurable patch antenna that covers the frequency band for unmanned aerial vehicle communication.

II. PROPOSED MULTI-POLARIZED PATCH ANTENNA

Figure 1 (a) shows a schematic diagram of the overall structure and feeding of the proposed antenna. A patch antenna is placed on the top surface of the upper substrate, and a capacitance power supply unit for power supply and impedance matching is located below it. By changing the length and width of the capacitance feeding part, the series capacitance can be adjusted to achieve impedance matching. The antenna is designed to operate at 2.45 GHz for WLAN applications. The proposed antenna was fabricated using an RF-60TC substrate from Taconic, which has a thickness of 0.64 mm. The dielectric constant (ϵ_r) is 6.15 and the loss tangent ($\tan\delta$) is 0.002. On the top surface of the lower substrate, slots are arranged at four corners for impedance matching, front-to-back ratio improvement, and wide electrical length, even in small ground surface sizes. The air gap between the upper and lower substrates is connected through the fixed pins and the feeding pins. It is designed to connect the signal from the power supply circuit to the capacitance power supply. As shown in Figs. 1 (b)-(c), the antenna structure has the following layout parameters: the width of the substrate (W_s) is 49 mm, the width of the square patch (W_p) is 37.5 mm, the width (W_{pin}) and height (H_{pin}) of the feeding and fixed pins are 10 mm and 5 mm, respectively, the distance (W_g) between the patch and feed pin is 2.25 mm, slot width (S_w) is 2 mm, slot length (S_l) is 20 mm, length from corner to the slot (S_m) is 3 mm, linear polarization (LP) feed line length (L_{f1}) and circular polarization (CP) feed line length (L_{f2}) are x mm and y mm, capacitance feed line width (W_c) and length (L_c) are 1 mm and 2.75 mm, respectively. The overall size of the proposed multi-polarized antenna

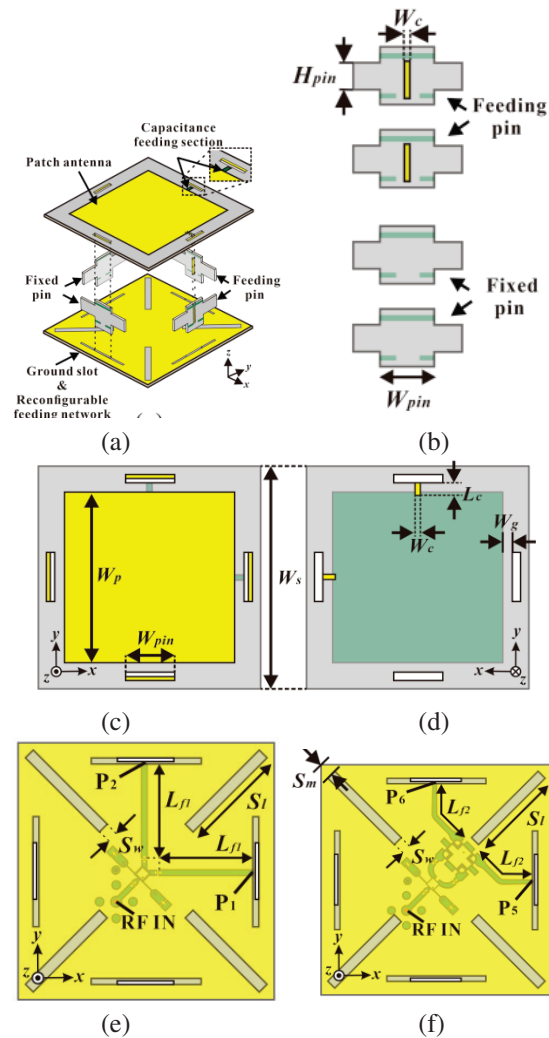


Fig. 1. Proposed antenna configuration: (a) Overall configurations of the proposed patch antenna, (b) front views of fixed and feeding pins, (c)-(d) top and bottom views of the upper substrates, and (e)-(f) top views of the feeding network that forms linear polarization and circular polarization.

is $(0.389\lambda_o \times 0.389\lambda_o \times 0.005\lambda_o)$, where λ_o is the wavelength in free space at the lowest frequency of operation (2.38 GHz). For the miniaturization of the proposed multi-polarized antenna, the patch antenna was designed to be miniaturized using the slot on the ground plane, as shown in Fig. 1 (d).

The electrical length was increased through the effect of the meander line, as the current flow was changed by the arrangement of slots at each corner of the ground plane. To obtain the optimum structure for the proposed antenna, the parameter sweep and optimization tools of the CST Microwave Studio 2022 have been used to determine the optimized dimensions

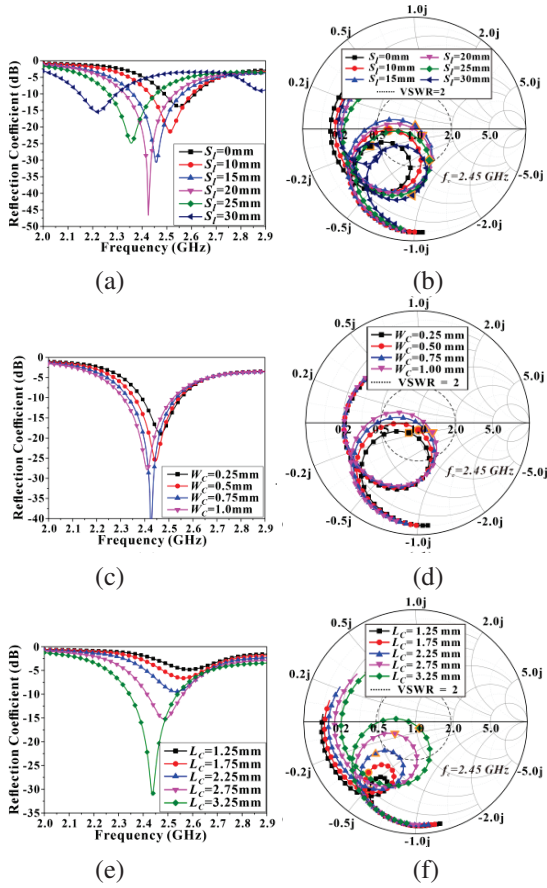


Fig. 2. Simulated reflection coefficients and impedance variations on the smith chart of the proposed antenna according to the (a)-(b) slot length (S_l), (c)-(d) width (W_c) of the capacitance feed line resonator, and (e)-(f) length (L_c) of the capacitance feed line resonator. The resonance frequency $f_c = 2.45$ GHz.

of the proposed antenna and the length of the slot. Figures 2 (a)-(b) show the change in resonance frequency according to the change in the length of the slot (S_l) placed on the proposed antenna ground surface. It is possible to adjust the resonance frequency up to 400 MHz by changing the length of the slot on the ground surface.

Figures 2 (c)-(f) show the simulated reflection coefficients and impedance variations of the proposed antenna according to the feed line width (W_c) and length (L_c). Figure 3 shows the current distribution of the conventional and proposed patch antennas.

For the proposed patch antenna, the slot placed at each corner will result in a longer current path than the conventional patch antenna, resulting in a longer electrical length of the patch antenna. Therefore, the ground surface slot structure reduced in size by approximately

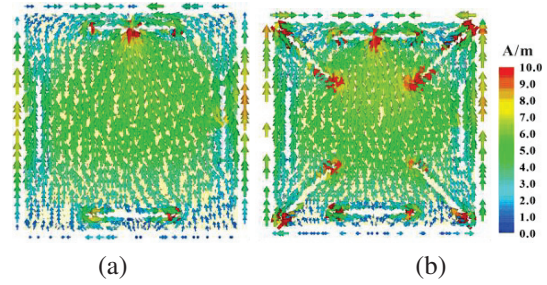


Fig. 3. Current distribution of the conventional and proposed antennas: (a) Conventional patch antenna without slots and (b) proposed patch antenna with slots.

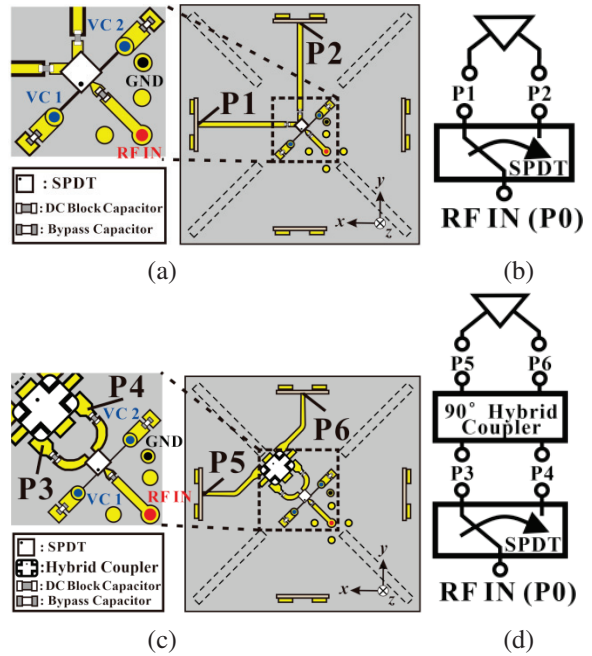


Fig. 4. Configurations and block diagram of the proposed feeding network: (a)-(b) Linear polarization modes and (c)-(d) circular polarization modes.

25%. For wide bandwidth, capacitance feed lines are printed on one side of the crossed rectangular support using two RF-60 substrates, as shown in Fig. 1 (b). To match impedance while enhancing bandwidth, the length and width of the capacitance feed line are adjusted to resonate at 2.45 GHz. Figure 4 shows the four modes of polarization achieved from two cases of reconfigurable feeding networks. The linear polarization feeding network in Figs. 4 (a)-(b) comprises one input port, two output ports, and one single-pole double-throw (SPDT) switch. The SPDT switch is the CG2176X3-C2 AS179-92LF model manufactured by Skyworks. In addition, a 100 pF capacitor is connected for DC blocking, and a

1000 pF capacitor is connected for bypass. All of these capacitors are manufactured by Murata in the 01005-inch size. Figures 4 (c)-(d) show the circular polarization feeding network. The circular polarization feeding network has a configuration in which a hybrid coupler is added to the front of the output ports of the linear polarization feeding network. The polarization mode is selected by using the SPDT switch when the RF input signal is applied. The RF signal input in Figs. 4 (a)-(b) is transmitted to P1 or P2 through the SPDT switch, and the RF signal is fed to the patch through the capacitance feeding line under the patch. The patch antenna has a horizontal LP (H-LP) when the signal is applied to P1, and has the characteristics of vertical LP (V-LP) when the signal is applied to P2. On the other hand, the RF signal input in Figs. 4 (c)-(d) is transmitted to P3 or P4 through the SPDT switch, which transmits a phase difference signal to P5 and P6 through a 90° hybrid coupler so that the RF signal is fed to the patch through the capacitance feed line under the patch. The 90° hybrid coupler used in this circuit is the RCP2650Q03 from RN2 Technologies. When a signal is applied to P3 through the SPDT switch, the patch antenna is applied with a signal of 0° to P5 and a signal of 90° to P6, and the patch antenna has the left-hand CP (LHCP) mode characteristic. In this way, when a P4 signal is applied through the SPDT switch, a 90° signal is applied to the P5 and a 0° signal is applied to the P6 so that the patch antenna has the right-hand CP (RHCP) mode characteristics. Figure 5 shows the implemented and mounted proposed antenna on a UAV. Figures 5 (a)-(c) show the top and bottom views of the proposed patch antenna. Figures 5 (d)-(e) show the overall configuration and mounted proposed antenna on the UAV.

III. RESULT AND DISCUSSION

The proposed UAV antenna, along with the feeding network operating in the 2.45 GHz ISM band has been optimized using a commercial full-wave electromagnetic tool (CST Microwave Studio 2022). To miniaturize the antenna design, the proposed antenna was fabricated on an RF-60 substrate of 0.64 mm thickness and a copper thickness of $18 \mu\text{m}$. The reflection coefficient and isolation were measured using a vector network from Rohde & Schwarz, and the radiation patterns, axial ratio, and gains for each polarization were measured by the Korea Radio Promotion Association's EM Technology Institute. The measured results of the dual LP antenna are presented in Figs. 6 (a)-(b). In the case of dual orthogonal LP in Fig. 6 (a), the reflection coefficients of H-LP and V-LP modes are less than -10 dB, and the 10-dB bandwidth of LP modes is approximately 4.9% from 2.39 GHz to

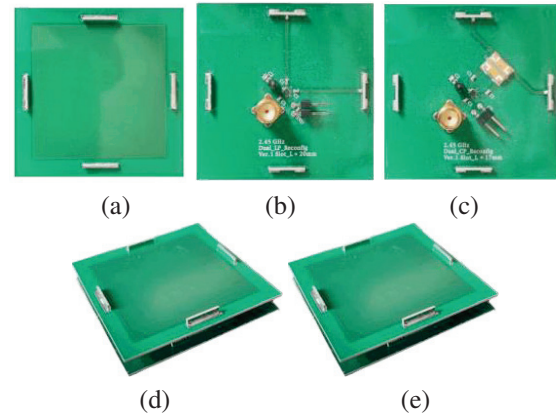


Fig. 5. Implemented and mounted proposed antenna on the UAV: (a) Top views of the patch antenna, (b)-(c) bottom views of the feeding networks, (d) overall configurations of the proposed patch antenna, and (e) mounted proposed patch antenna.

2.51 GHz. The switch's insertion loss is approximately -0.75 dB, and the isolation between two capacitance feeders is -23 dB at 2.45 GHz.

Figure 6 (b) shows the elevation radiation patterns (xz plane) for each polarization mode. They are almost the same for horizontal and vertical LP. The peak gain and front-to-back ratio are more than 6.6 dBi and 12.3 dB to 13.5 dB in each polarization mode, and the efficiencies of LP modes are approximately 82%. Figures 6 (c)-(f) show the characteristics of the dual circularly polarized antenna.

In Fig. 6 (c), the reflection coefficients of RHCP and LHCP modes are less than -10 dB, which include the insertion losses of the SPDT switch and hybrid couplers. The phase variation is approximately 90° , and the transmission coefficient, including a 3 dB divided power loss is approximately -3.5 dB. The 10 dB bandwidth of CP modes is approximately 4.5% from 2.38 GHz to 2.49 GHz. Figure 6 (d) shows the axial ratio and phase variation of the dual circularly polarized antenna. The 3-dB axial ratio bandwidths of CP modes cover approximately 12% from 2.3 GHz to 2.6 GHz. The phase variations are $\pm 90^\circ$ in each RHCP and LHCP mode.

Figures 6 (e)-(f) show the realized gain and radiation pattern. The peak gain and front-to-back ratio are 7.2 dBi and 15.7 dB to 27 dB, respectively. The performance of the proposed antenna is compared to other multi-polarized reconfigurable antennas, as indicated in Table 1. Compared to the previously reported antennas, the proposed antenna has a smaller size, wider bandwidth, and higher gain.

Table 1: Performance comparisons of multiple-polarized antennas

Ref.	f_c (GHz)	BW (%)	Gain (dBi)	Polarization	AR BW (%)	Elect. Size (λ_o^3)
[7]	2.46	52.03	9	1 LP & 2 CP	63.1-	$0.65 \times 0.65 \times 0.19$
[8]	2.65	34	3.7	4 LP	-	$0.7 \times 0.7 \times 0.23$
[9]	2.7	37	8.9	3 LP & 2 CP	50.6	$0.68 \times 0.68 \times 0.24$
[10]	2.45	11.4	7.3	CLP & 2 CP	14	$0.64 \times 0.64 \times 0.05$
[12]	4.805	7.28	6.63	1 LP & 2 CP	7	$0.56 \times 0.56 \times 0.037$
[14]	3.5	11.4	7.5, 5	1 LP & 2 CP	11.4	$0.9 \times 0.9 \times 0.036$
[16]	2.4	0.8	5.83, 6.4	1 LP & 2 CP	0.5	$0.65 \times 0.65 \times 0.01$
[17]	3.4	5.9	5.89, 5.81	2 LP	-	$0.85 \times 0.85 \times 0.26$
Prop.	2.45	4.5	6.6, 7.2	2 LP or 2 CP	12	$0.389 \times 0.389 \times 0.05$

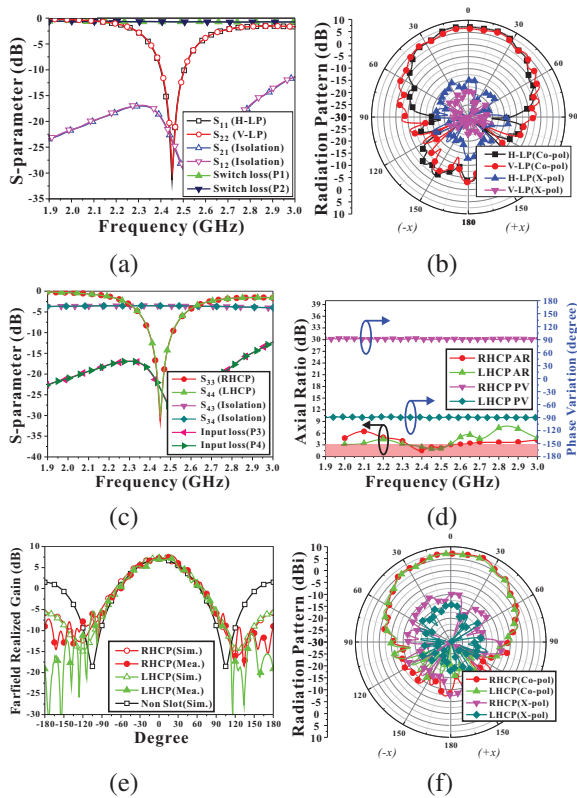


Fig. 6. Characteristics of the proposed antenna at each polarization mode: (a) Measured S-parameters of a linearly polarized antenna, (b) measured radiation patterns of two LP modes in the xz plane, (c) measured S-parameters of the dual circularly polarized antenna, (d) axial ratio and phase variation of the dual circularly polarized antenna, (e) simulated and measured realized gain of the dual CP modes, and (f) radiation patterns of the dual CP modes in the xz plane.

IV. CONCLUSION

A 2.45 GHz multi-polarized reconfigurable patch antenna for U2X communications is presented in this

paper. The proposed feeding network utilizes an SPDT switch and hybrid coupler to achieve various polarization types, including V-LP or H-LP, as well as LHCP or RHCP. The proposed multi-polarized reconfigurable antenna can provide a compact size and high gain in the 2.45 GHz ISM band. This antenna can be easily mounted on UAVs and has a low-profile, balanced structure. It also offers ease of control for selecting different types of polarization. Therefore, the proposed antenna can be widely used for UAV applications, making it a promising candidate for performing a diverse range of missions in numerous fields.

ACKNOWLEDGMENT

This work was supported in part by the Korean government (MSIT) through the National Research Foundation of Korea, South Korea, under Grant 2019R1C1C1008102 and in part by the Institute of Information & Communications Technology Planning & Evaluation (IITP) grant funded by the Korea government (MSIT), under Grant RS-2022-00156409 (ICT innovation human resources 4.0). (Corresponding author: Wang-Sang Lee.)

REFERENCES

- [1] P. G. Fahlstrom, T. J. Gleason, and M. H. Sadraey, *Introduction to UAV Systems*. Hoboken, NJ: Wiley, 2022.
- [2] Y. Fan, X. Liu, B. Liu, and R. Li, "A broadband dual-polarized omnidirectional antenna based on orthogonal dipoles," *IEEE Antennas Wireless Propag. Lett.*, vol. 15, pp. 1257-1260, 2016.
- [3] D. Wu, L. Yang, G. Fu, and X. Shi, "Compact and low-profile omnidirectional circularly polarized antenna with four coupling arcs for UAV applications," *IEEE Antennas Wireless Propag. Lett.*, vol. 16, pp. 2919-2922, 2017.
- [4] D. G. Seo, J. S. Park, and W. S. Lee, "Lightweight printed dipole antenna array with 3×2 beam-forming network for wide UAV communication

- coverage,” *Journal of Engineering & Technology*, vol. 15, pp. 1769-1773, 2020.
- [5] A. Khidre, K. Lee, F. Yang, and A. Z. Elsherbeni, “Circular polarization reconfigurable wideband E-shaped patch antenna for wireless applications,” *IEEE Trans. Antennas Propag.*, vol. 61, no. 2, pp. 960-964, 2013.
- [6] J.-S. Row, W.-L. Liu, and T.-R. Chen, “Circular polarization and polarization reconfigurable designs for annular slot antennas,” *IEEE Trans. Antennas Propag.*, vol. 60, no. 12, pp. 5998-6002, 2012.
- [7] G. Jin, L. Li, W. Wang, and S. Liao, “A wideband polarization reconfigurable antenna based on optical switches and C-shaped radiator,” *Microw. Optical Technology Lett.*, vol. 62, no. 6, pp. 2415-2422, 2019.
- [8] H. Wong, W. Lin, L. Huitema, and E. Arnaud, “Multi-polarization reconfigurable antenna for wireless biomedical system,” *IEEE Trans. Biomed. Circuits Syst.*, vol. 11, no. 3, pp. 652-660, 2017.
- [9] H. H. Tran, N. Nguyen-Trong, T. T. Le, and H. C. Park, “Wideband and multi-polarization reconfigurable crossed bowtie dipole antenna,” *IEEE Trans. Antennas Propag.*, vol. 65, no. 12, pp. 6968-6975, 2017.
- [10] L. Ran, D.-P. Yang, and S.-Y. Wang, “A mode-combination-based polarization-reconfigurable antenna,” *Int. J. RF Microw. Comput.-Aided Eng.*, vol. 32, no. 4, 2022.
- [11] K. M. Mak, H. W. Lai, K. M. Luk, and K. L. Ho, “Polarization reconfigurable circular patch antenna with a C-shaped,” *IEEE Trans. Antennas Propag.*, vol. 65, no. 3, pp. 1388-1392, 2017.
- [12] M. Li, Z. Zhang, and M.-C. Tang, “A compact, low-profile, wideband, electrically controlled, tri-polarization-reconfigurable antenna with quadruple gap-coupled patches,” *IEEE Trans. Antennas Propag.*, vol. 68, no. 8, pp. 6395-6400, 2020.
- [13] S. Chen, F. Wei, P. Qin, Y. J. Guo, and X. Chen, “A multi-linear polarization reconfigurable unidirectional patch antenna,” *IEEE Trans. Antennas Propag.*, vol. 65, no. 8, pp. 4299-4304, 2017.
- [14] H. L. Zhu, S. W. Cheung, X. H. Liu, and T. I. Yuk, “Design of polarization reconfigurable antenna using metasurface,” *IEEE Trans. Antennas Propag.*, vol. 62, no. 6, pp. 2891-2898, 2014.
- [15] C. Y. D. Sim, Y. J. Liao, and H. L. Lin, “Polarization reconfigurable eccentric annular ring slot antenna design,” *IEEE Trans. Antennas Propag.*, vol. 63, no. 9, pp. 4152-4155, 2015.
- [16] X.-X. Yang, B.-C. Shao, F. Yang, A. Z. Elsherbeni, and B. Gong, “A polarization reconfigurable patch antenna with loop slots on the ground plane,” *IEEE Antennas Wireless Propag. Lett.*, vol. 11, pp. 69-72, 2012.
- [17] Y. Mu, J. Han, D. Xia, X. Ma, H. Liu, and L. Li, “The electronically steerable parasitic patches for dual-polarization reconfigurable antenna using varactors,” *Applied Computational Electromagnetics Society (ACES) Journal*, pp. 58-67, 2022.



Seong-Hyeop Ahn received the B.S. and M.S. degrees in electronic engineering from Gyeongsang National University (GNU), Jinju, South Korea, in 2018 and 2020, respectively. Since 2022, he has been working toward the Ph.D. degree in electronic engineering from GNU.

His research interests are high-power microwave systems, near-field wireless power transfer and communications systems, RFID/IoT sensors, and RF/microwave circuit and antenna designs.



Yu-Seong Choi received the B.S. and M.S. degrees in electronic engineering from Gyeongsang National University (GNU), Jinju, South Korea, in 2019 and 2021, respectively. Since 2022, he has been working in Korea Aerospace Industries.

His research interests include reconfigurable antenna design & analysis, RF/Microwave circuits and systems, and RFID/IoT sensors.



Mohamed Elhefnawy received the B.S. and M.S. degrees in electronics and communications engineering from Tanta University and Arab Academy for Science & Technology, Egypt, in 1999 and 2005, respectively. He received a Ph.D. degree in communications engineering from USM University, Malaysia, in 2010. Since 2023, he has been working as a senior researcher in the Department of Electronic Engineering, Gyeongsang National University (GNU), Jinju, South Korea. From 2012 to 2023, he worked as a lecturer in the Department of Electrical Engineering at the Faculty of Engineering, October 6 University, Egypt.

He has a strong academic background that includes RF/microwave engineering, electromagnetic theory, and antenna theory. His research interests include antennas, wave propagation, RF and microwave, and communications.

He has a strong academic background that includes RF/microwave engineering, electromagnetic theory, and antenna theory. His research interests include antennas, wave propagation, RF and microwave, and communications.



Wang-Sang Lee received the B.S. degree from Soongsil University, Seoul, South Korea, in 2004, and the M.S. and Ph.D. degrees in electrical engineering from the Korea Advanced Institute of Science and Technology (KAIST), Daejeon, South Korea, in 2006 and 2013,

respectively.

From 2006 to 2010, he was with the Electromagnetic Compatibility Technology Center, Digital Industry Division, Korea Testing Laboratory (KTL), Ansan-si, South Korea, where he was involved in the international standardization for radio frequency identification (RFID) and photovoltaic systems as well as electromagnetic interference (EMI)/EMC analysis, modeling, and measurements for information technology devices. In 2013, he joined the Korea Railroad Research Institute (KRRRI), Uiwang-si, South Korea, as a Senior Researcher, where he was involved in the position detection for high-speed railroad systems and microwave heating for low-vibration rapid tunnel excavation systems. Since 2014, he has been an Associate Professor with the Department of Electronic Engineering, Gyeongsang National University (GNU), Jinju, South Korea. From 2018 to 2019, he was a Visiting Scholar with the ATHENA Group, Georgia Institute of Technology, Atlanta, GA, USA. His current research interests include near- and far-field wireless power and data communications systems, RF/microwave antenna, circuit, and system design, RFID/Internet of Things (IoT) sensors, and EMI/EMC.

Dr. Lee is a member of IEEE, IEC/ISO JTC1/SC31, KIEES, IEIE, and KSR. He was a recipient of the Best Paper Award at IEEE RFID in 2013, the Kim Choong-Ki Award Electrical Engineering Top Research Achievement Award at the Department of Electrical Engineering, KAIST, in 2013, the Best Ph.D. Dissertation Award at the Department of Electrical Engineering, KAIST, in 2014, the Young Researcher Award at KIEES in 2017, and the Best Paper Awards at IEIE in 2018 and KICS in 2019.